Development of a non-destructive testing method to determine the tensile fatigue life of Ti-6Al-4V additively manufactured parts

S. Botha

orcid.org/0000-0002-4975-0721

Dissertation submitted in fulfilment of the requirements for the degree *Master of Engineering in Mechanical Engineering* at the North West University

Supervisor: Mr. CP Kloppers

Graduation: May 2020

Student number: 25081128

PREFACE

This dissertation consists of six chapters, a reference section and two appendices.

Chapter 1: This chapter gives the reader the introduction to the study, which includes the background, the problem statement and objectives of this study, the research methodology and the dissertations' layout.

Chapter 2: This chapter contains a detailed literature study on the concepts that are relevant to additive manufacturing among other concepts in this study, including work done on this subject.

Chapter 3: This chapter covers the theoretical calculations and knowledge required for this study.

Chapter 4: This chapter discusses the experimental procedure, thus the steps taken to set up the experiments and execute all relevant tests for the study.

Chapter 5: The results obtained from the experiments are discussed in this chapter.

Chapter 6: This chapter presents the recommendations for improving this study and further studies. Conclusions made from this study are also discussed in this chapter

References: All the references used in the literature study and throughout the document are listed in this chapter.

Appendix A: Tensile test specimens' results are discussed in this section.

Appendix B: Fatigue test data is included in this section.

ACKNOWLEDGEMENTS

I would like to begin by thanking the Lord Jesus Christ for giving me the strength to complete this study and get up each day with renewed courage to take on the challenges that crossed my path.

I would also like to thank the Collaborative Programme for Additive Manufacturing for funding my studies by providing me with a bursary for two years to complete my studies. I also express my gratitude to the North-West University for their contribution by granting me a master's degree student bursary.

Thank you to Mr CP Kloppers for providing leadership during the study and for advice on how to overcome the obstacles that the study presented.

I also express my appreciation for Mr Sarel Naude, the Faculty of Mechanical Engineering laboratory manager for providing assistance during the testing phase of this study. Moreover, acknowledgement is given to Dr Anine Jordaan, the senior subject specialist at the laboratory for Electron Microscopy Chemical Recourse Beneficiation (CRB) for assisting with the SEM imaging. My thanks also go to Ms Daniella Da Costa and Mr Geo Joubert, two final-year students, for assisting me with the experimental setup and verification of this study.

Lastly but most importantly, I would like to thank my parents for their endless support over the past two years. They are an inspiration to me, always pushing me to be a better version of myself.

ABSTRACT

Direct metal laser sintering (DMLS) is a powder bed fusion (PBF) technology used for additive manufacturing (AM). This process deploys a laser to selectively fuse regions of a powder bed. The manufacturing of a part is done layer-by-layer with the help of software that created two-dimensional slices of a 3D CAD model.

Defects that occur during the manufacturing process have a significant influence on the fatigue performance of Ti-6Al-4V additively manufactured parts. These defects occur in the form of surface and internal voids. Post-processing like polishing the surface of a specimen can also strongly influence the fatigue performance of a test specimen. This study was completed using test specimens in the as-built condition where they are only stress-relieved after manufacturing with no post-processing having been done on them.

A Micro-CT scanner is commonly used to determine the location and size of defects present in a part that was fabricated using additive manufacturing. The Micro-CT scans will detect any surface- or internal defects present in the part. Literature indicates that surface defects will have a greater influence on the fatigue life than the internal defects. This is arguably due to stress concentrations on the surface which will lead to cracks that will propagate from these defects through the part. Micro-CT scanning is an expensive, operator-specific process. An alternative process might be beneficial where Micro-CT scanning is not available due to financial or time constraints. Among alternative equipment that can give a representative indication of the fatigue life and defects that could cause failure, the Digital Image Correlation (DIC) system and the Scanning Electron Microscopy (SEM) imaging serve as possible alternatives. The DIC system gives an indication of where the strain is concentrated, while the SEM images show defects in the specimen including the size of these defects once a part has failed.

This study investigates the level accuracy that using a DIC system can obtain as an alternative non-destructive test to predict where a test specimen will fail. To determine whether this alternative is viable, tests are carried out until the specimens fail. The DIC images are analysed at 50% of the fatigue life as well as the point just before failure to determine whether the DIC system accurately indicates the strain concentration at the same point where the specimens fail.

Experimental data from the study shows that the DIC system could accurately predict the point of failure at the fatigue half-life in only 10% of the test specimens that were investigated. The DIC system was able to accurately predict the point of failure right before failure occurred in only 25% of the test specimens that were investigated.

Keywords: *Additive manufacturing, AM, DIC, digital image correlation, direct metal laser sintering, DMLS, fatigue life prediction, fatigue testing, Ti-6Al-4V*

TABLE OF CONTENTS

PREFACE ..... **I**

ACKNOWLEDGEMENTS ..... **II**

ABSTRACT ..... **III**

LIST OF ABBREBVIATTIONS ..... **XIX**

CHAPTER 1 ..... **1**

INTRODUCTION **1**

1.1 Background **1**

1.2 Problem statement **2**

1.3 Hypothesis **2**

1.4 Aim and objectives **2**

1.4.1 Research aim 2

1.4.2 Research objectives 3

1.5 Research methodology **3**

CHAPTER 2 ..... **5**

LITERATURE SURVEY **5**

2.1 Introduction **5**

2.2 Additive Manufacturing **6**

2.3 Different types of AM **10**

2.4 Metal-sintering technology **14**

2.4.1 Powder bed fusion (PBF) 14

2.4.2 Direct energy deposition 16

2.4.3 Electron beam melting 18

2.5 Heat treatment of AM parts 19

2.6 Properties of AM Parts 21

2.7 Mechanical fatigue testing 22

2.8 Analysing of cavities and other characteristics 23

CHAPTER 3 27

THEORY 27

3.1 Material properties 27

3.1.1 Stress 27

3.1.2 Strain 27

3.1.3 Stress-strain graph 28

3.1.4 Modulus of elasticity 29

3.2 Fatigue 29

3.2.1 Waveform properties 29

3.2.1.1 Stress range 30

3.2.1.2 Stress Amplitude 30

3.2.1.3 Mean stress 30

3.2.1.4 Stress ratio 30

3.2.1.5 Amplitude ratio 30

3.2.2 The stress-life method 31

3.2.2.1 Design equations for the stress-life method 31

3.2.3 The strain-life method 34

3.3 Verification of theory calculations and testing results 35

CHAPTER 4 37

EXPERIMENTAL PROCEDURE **37**

4.1 Test specimen **37**

4.2 Hardware **39**

4.2.1 EOSINT M280 39

4.2.2 MTS landmark 40

4.2.3 DIC Q400 40

4.3 Test sample preparation **41**

4.4 Standard test method procedure **43**

4.4.1 Test environment 44

4.4.2 Test machine control 44

4.4.3 Waveform 45

4.4.4 Strain rate and frequency of cycling 46

4.4.5 Test commencement 46

4.4.6 Number of specimens 46

4.4.7 Recording 47

4.4.8 Determination of failure 47

4.4.9 Test duration 49

4.4.10 Data analysis 49

CHAPTER 5 ..... **51**

RESULTS **51**

5.1 Material properties **51**

5.1.1 0º Test specimens 51

5.1.2 90º Test specimens 53

5.2 Fatigue results 54

5.2.1 0º Fatigue Specimens 54

5.2.2 90º Fatigue specimens 58

5.2.3 Fatigue tests conclusion 63

5.3 DIC results discussion 63

5.3.1 Summary of DIC system's prediction ability 63

5.4 SEM results discussion 65

CHAPTER 6 66

CONCLUSION AND RECOMMENDATIONS 66

REFERENCES 68

APPENDIX A 72

A.1 0º Tests 72

A.2 90º Tests 75

APPENDIX B 78

FATIGUE TESTS RESULTS 78

0º FATIGUE TEST SPECIMENS 78

B.1 Specimen B1 78

B.2 Specimen B2 80

B.3 Specimen B3 81

B.4 Specimen B4 83

B.5 Specimen B5 84

B.6 Specimen B6 86

B.7 Specimen B7 88

B.8 Specimen B8 90

B.9 Specimen B9 91

B.10 Specimen B10 92

B.11 Specimen B11 94

90º FATIGUE TEST SPECIMEN 95

B.12 Specimen A1 95

B.13 Specimen A2 97

B.14 Specimen A3 99

B.15 Specimen A4 100

B.16 Specimen A5 102

B.17 Specimen A6 103

B.18 Specimen A7 105

B.19 Specimen A8 106

B.20 Specimen A9 108

B.21 Specimen A10 110

B.22 Specimen A11 111

LIST OF TABLES

Table 2-1: Benefits, limitations, and applications of the material extrusion process [6] 10

Table 2-2: Benefits, limitations, and applications of the VAT polymerization process [6] 11

Table 2-3: Benefits, limitations, and applications of the powder bed fusion technologies [6] 12

Table 2-4: Material jetting process' benefits, limitations and applications [6] 12

Table 2-5: Benefits, limitations, and applications for the binder jetting process [6] 13

Table 2-6: Benefits, limitations, and applications of directed energy deposition 13

Table 2-7: Benefits, limitations and applications for sheet lamination 14

Table 2-8: Differences between EBM and MLS [11] 18

Table 2-9: Chemical composition of Ti-6Al-4V powder 21

Table 3-1: Parameters for Marin surface modification factor (Table 6-2 [36]) 32

Table 3-2: Reliability Factor ke corresponding to eight percent standard deviation of the endurance limit [36] 32

Table 4-1: EOSINT M280 specifications [39] 39

Table 4-2: MTS Landmark 370.10 specifications [40] 40

Table 4-3: MTS input variables showing the applied force as a percentage load of the UTS ... 45

Table 5-1: Peak loads obtained from 0º tensile test specimens 51

Table 5-2: Material Properties of 0º tensile test specimens 52

Table 5-3: Peak loads obtained from 90º tensile test specimens 53

Table 5-4: Material properties for 90º tensile test specimens 54

Table 5-5: 0º Test specimens fatigue test results 55

Table 5-6: 90º Test specimen fatigue test results 59

Table 5-7: Summary of 0º fatigue tests' DIC results 64

Table 5-8: Summary of 90º fatigue tests' DIC results 64

LIST OF FIGURES

Figure 1.5-1: Flow chart for research methodology 3

Figure 2.1-1: Comparison of the three manufacturing techniques commonly used [1] 6

Figure 2.2-1: Cost comparison for different manufacturing techniques [1] 7

Figure 2.2-2: 3D models of parts manufactured through AM 7

Figure 2.2-3: CAD file sliced using PrusaSlicer 2.1.0 8

Figure 2.2-4: CAD file printed with support material included 9

Figure 2.2-5: Support material removed from parts 9

Figure 2.4-1: Schematic drawing showing the selective lase sintering process [11] 15

Figure 2.4-2: GE's fuel nozzle, which has been additively manufactured [12] 16

Figure 2.4-3: Schematic of the laser powder DED process [11] 17

Figure 2.4-4: Schematic illustration of the EBM process [11] 19

Figure 2.5-1: Stress relieving cycle 20

Figure 2.7-1: S-N diagram for steel and aluminum alloys [22] 23

Figure 2.8-1: Schematic showing the process of X-ray micro-CT scanning [24] 24

Figure 2.8-2: Schematic diagram of Scanning Electron Microscope [32] 26

Figure 3.1-1: The conventional and true stress-strain diagrams for ductile material (steel) [22] 28

Figure 3.2-1: Stress-cycles waveform [35] 29

Figure 3.2-2: S-N diagram plotted from results obtained from a completely reversed axial fatigue test [36] 31

Figure 3.2-3: True stress-true strain hysteresis loop showing five stress reversals of a cyclic softening material [36] 34

Figure 3.2-4: Log-log plot showing how the fatigue life is related to the true strain amplitude for hot-rolled SAE 1020 steel [36] 34

Figure 3.3-1: Results of fatigue tests 36

Figure 4.1-1: ASTM E606 test specimen dimensions [8] 37

Figure 4.1-2: Recommended low-cycle fatigue specimens [38] 38

Figure 4.3-1: The sponge after it has been dabbed in the acrylic paint 43

Figure 4.3-2: Test samples once the speckle pattern has been applied 43

Figure 4.4-1: Test setup in laboratory 44

Figure 4.4-2: MTS control computer showing the waveform of the test carried out 46

Figure 4.4-3: Image showing all the test samples that were tested 47

Figure 4.4-4: Definitions of Tension and Compression Modulus for a Determination of Failure [9] 48

Figure 5.1-1: Load versus Extension graph for 0º tensile test specimens 51

Figure 5.1-2: Load versus extension for 90º tensile test specimens 53

Figure 5.2-1: S-N graph for the 0º test specimen fatigue results 55

Figure 5.2-2: Specimen B5 SEM images showing a surface defect and impurities on the fractured surface 56

Figure 5.2-3: Specimen B2's DIC images 56

Figure 5.2-4: Specimen B1's DIC results 57

Figure 5.2-5: DIC results for specimen B8 57

Figure 5.2-6: SEM image for specimen B7 showing an internal defect 58

Figure 5.2-7: S-N graph for the 90º test specimen fatigue tests 59

Figure 5.2-8: SEM image for specimen A8 60

Figure 5.2-9: DIC results for specimen A7 60

Figure 5.2-10: SEM image of specimen A2 61

Figure 5.2-11: DIC results for test specimen A6 62

Figure 5.2-12: DIC results for specimen A11 62

Figure A.1-1: Stress-Strain Curve for 0º tensile test specimen 1..... 72

Figure A.2-1: Stress-Strain Curve for 90º tensile test specimen 1..... 75

Figure A.2-2: Modulus of Elasticity for 90º tensile test specimen 1 75

Figure A.2-3: Stress-Strain Curve for 90º tensile test specimen 2..... 76

Figure A.2-4: Modulus of Elasticity for 90º tensile test specimen 2 76

Figure A.2-5: Stress-Strain Curve for 90º tensile test specimen 3..... 77

Figure A.2-6: Modulus of Elasticity for 90º tensile test specimen 3 77

Figure B.1-1: Specimen B1 hysteresis stress-strain curve..... 78

Figure B.1-2: Strain-life graph for specimen B1 79

Figure B.1-3: From left to right: B1 reference image, B1 half-life image, B1 final image, B1 failure image 79

Figure B.2-1: Specimen B2 hysteresis stress-strain curve..... 80

Figure B.2-2: Strain life graph for specimen B2 80

Figure B.2-3: From left to right: B2 reference image, B2 half-life image, B2 final image, B2 failure image 81

Figure B.3-1: Hysteresis stress-strain curve for specimen B3..... 81

Figure B.3-2: Strain life graph for specimen B3 82

Figure B.3-3: From left to right: B3 reference image, B3 half-life image, B3 final image, B3 failure image 82

Figure B.4-1: Hysteresis stress-strain curve for specimen B4..... 83

Figure B.4-2: Strain life graph for specimen B4 83

Figure B.4-3: From left to right: B4 reference image, B4 half-life image, B4 final image, B4 failure image 84

Figure B.5-1: Hysteresis stress-strain curve for specimen B5 84

Figure B.5-2: Strain-life graph for specimen B5 85

Figure B.5-3: From left to right: B5 reference image, B5 half-life image, B5 final image, B5 failure image 85

Figure B.5-4: SEM image of specimen B5 86

Figure B.6-1: Hysteresis stress-strain curve for specimen B6 86

Figure B.6-2: Strain-life graph for specimen B6 87

Figure B.6-3: From left to right: B6 reference image, B6 half-life image, B6 final image, B6 failure image 87

Figure B.7-1: Hysteresis stress-strain curve for specimen B7 88

Figure B.7-2: Strain-life curve for specimen B7 88

Figure B.7-3: From left to right: B7 reference image, B7 half-life image, B7 final image, B7 failure image 89

Figure B.7-4: SEM images for specimen B7 89

Figure B.8-1: Hysteresis stress-strain curve for specimen B8 90

Figure B.8-2: Strain-life graph for specimen B8 90

Figure B.8-3: From left to right: B8 reference image, B8 half-life image, B8 final image, B8 failure image 91

Figure B.9-1: Hysteresis stress-strain curve for specimen B9 91

Figure B.9-2: Strain-life graph for specimen B9 92

Figure B.10-1: Hysteresis stress-strain curve for specimen B10 92

Figure B.10-2: Strain-life graph for specimen B10 93

Figure B.10-3: From left to right: B10 reference image, B10 half-life image, B10 final image, B10 failure image 93

Figure B.11-1: Hysteresis stress-strain curve for specimen B11 94

Figure B.11-2: Strain-life graph for specimen B11 94

Figure B.11-3: From left to right: B11 reference image, B11 half-life image, B11 final image, B1 failure image 95

Figure B.12-1: Hysteresis stress-strain curve for specimen A1 95

Figure B.12-2: Strain-life graph for specimen A1 96

Figure B.12-3: From left to right: A1 reference image, A1 half-life image, A1 final image, A1 failure image 96

Figure B.13-1: Hysteresis stress-strain curve for specimen A2 97

Figure B.13-2: Strain-life graph for specimen A2 97

Figure B.13-3: From left to right: A2 reference image, A2 half-life image, A2 final image 98

Figure B.13-4: SEM images for specimen A2 98

Figure B.14-1: Hysteresis stress-strain curve for specimen A3 99

Figure B.14-2: Strain-life graph for specimen A3 99

Figure B.14-3: From left to right: A2 reference image, A3 half-life image, A3 final image, A3 failure image 100

Figure B.15-1: Hysteresis stress-strain curve for specimen A4 100

Figure B.15-2: Strain-life graph for specimen A4 101

Figure B.15-3: From left to right: A4 reference image, A4 half-life image, A4 final image, A4 failure image 101

Figure B.16-1: Hysteresis stress-strain curve for specimen A5 102

Figure B.16-2: Strain-life graph for specimen A5 102

Figure B.16-3: From left to right: A5 reference image, A5 half-life image, A5 final image, A5 failure image 103

Figure B.17-1: Hysteresis stress-strain curve for specimen A6 103

Figure B.17-2: Strain-life graph for specimen A6 104

Figure B.17-3: From left to right: A6 reference image, A6 half-life image, A6 final image, A6 failure image 104

Figure B.18-1: Hysteresis stress-strain curve for specimen A7 105

Figure B.18-2: Strain-life graph for specimen A7 105

Figure B.18-3: From left to right: A7 reference image, A7 half-life image, A7 final image, A7 failure image 106

Figure B.19-1: Hysteresis stress-strain curve for specimen A8 106

Figure B.19-2: Strain-life graph for specimen A8 107

Figure B.19-3: From left to right: A8 reference image, A8 half-life image, A8 final image, A8 failure image 107

Figure B.19-4: SEM images for test specimen A8 108

Figure B.20-1: Hysteresis stress-strain curve for specimen A9 108

Figure B.20-2: Strain-life graph for specimen A9 109

Figure B.20-3: From left to right: A9 reference image, A9 half-life image, A9 final image, A9 failure image 109

Figure B.21-1: Hysteresis stress-strain curve for specimen A10 110

Figure B.21-2: Strain-life graph for specimen A10 110

Figure B.21-3: From left to right: A10 reference image, A10 half-life image, A10 final image, A10 failure image 111

Figure B.22-1: Hysteresis stress-strain curve for specimen A11 111

Figure B.22-2: Strain-life graph for specimen A11 112

Figure B.22-3: From left to right: A11 reference image, A11 half-life image, A11 final image, A11 failure image..... 112

Figure B.22-4: SEM images for specimen A11 113

LIST OF ABBREBVIATTIONS

AM	Additive manufacturing
ASTM	American Society for Testing and Materials
BJ	Binder jetting
CAD	Computer-aided design
CAM	Computer-aided manufacturing
CCD	Charged coupled device
DED	Direct energy deposition
DIC	Digital image correlation
DLP	Direct light processing
DMLS	Direct metal laser sintering
DOD	Drop on demand
EBM	Electron beam melting
FDM	Fused deposition modelling
FFF	Fused filament fabrication
HIP	Hot isostatic pressing
ISO	International Organization for Standardization
LBMD	Laser-based metal deposition
LENS	Laser engineering net shaping
LOM	Laminated object manufacturing
ME	Material extrusion
Micro-CT	Micro-computed tomography
MJ	Material jetting
MLS	Metal laser sintering
PBF	Powder bed fusion
SEM	Scanning electron microscopy
SL	Sheet lamination
SLS	Selective laser sintering
STL	Stereolithography
UAM	Ultrasonic additive manufacturing
UTS	Ultimate tensile strength
UV	Ultraviolet
VP	Vat photopolymerization

CHAPTER 1

INTRODUCTION

This chapter draws attention to the commercialisation of AM (additive manufacturing) and the different technologies that can be used in this process.

1.1 BACKGROUND

Additive manufacturing (AM) is defined by [1] as: “Additive manufacturing makes ‘objects’ from a digital ‘model’ by depositing the constituent material/s in a layer-by-layer manner using digitally controlled and operated material laying tools”. AM has many advantages as this versatile and highly customisable form of manufacturing means that it can be used in a wide variety of industrial production sectors. The extensive range of materials available for the manufacturing of parts includes metallic, ceramic, and polymeric materials as well as composite materials. Its versatility makes this technology an attractive solution for manufacturing complex objects which would not be possible using traditional manufacturing techniques.

The success of AM depends on how well the manufactured object serves its intended use in the industry. According to [1], translating the superiority and convenience of AM in creating shapes and structures into useful products is critical for the adoption of AM in the industrial setup.

The commercial success, then, will depend on how firmly one can assure that the properties of the material meet the accepted, predefined standards while maintaining a competitive cost of production [1]. The market uptake of additively manufactured parts will thus only happen if the parts that are produced are manufactured with its intended properties, which can be confirmed through appropriate measurements.

A number of different technologies within AM can be used to manufacture a part. The International Organization for Standardization (ISO)/American Society for Testing and Materials (ASTM) 52900:2015 standard has categorised AM under seven categories. These categories include binder jetting (BJ), directed energy deposition (DED), material extrusion (ME), material jetting (MJ), powder bed fusion (PBF), sheet lamination (SL), and vat photopolymerization (VP) [2].

This thesis focuses specifically on Direct Metal Laser Sintering (DMLS), which is a PBF process. DMLS is an AM technique in which a high-power fibre laser creates solid layers from loose powder materials and joins them in an additive manner. This manufacturing process is characterised by

highly localised heat inputs during very short interaction times which significantly affect the microstructure [2, 3]. The affected microstructure complicates the entire process of commercialising AM and working towards realising Factory 4.0 / Manufacturing 4.0.

1.2 PROBLEM STATEMENT

Engineers want to be able to use AM as a technique for producing complex parts that ameliorate existing parts in various manufacturing industries.

While AM presents new possibilities for design freedom and the manufacturing of complex shapes, the material properties must be fully characterised for design purposes for these possibilities to be realised optimally. The mechanical properties, especially those focusing on the fatigue lifetime of parts, are normally tested by means of micro-CT scanning and a destructive testing process. Hence, the problem is to find an alternative solution for predicting the fatigue life of Ti-64 DMLS parts that have been produced on a EOSINT M280 printer. One of the limitations associated with this study is financial support. Hence an alternative non-destructive testing method needs to be investigated as micro-CT scanning is expensive.

The scientific method was used to investigate the fatigue life of parts and identify alternative solutions for reducing the cost and waiting time associated with the scanning process.

1.3 HYPOTHESIS

A hypothesis was made for this empirical study. The acceptance or rejection of this hypothesis serves as the study's validation. The hypothesis for this study is formulated as follows:

The DIC system, which can accurately detect small displacements, will be able to predict where all of the test specimens will fail.

1.4 AIM AND OBJECTIVES

The aim and objectives of this study present to the reader an expectation of what has been done in this study and the outcomes that the research intended to achieve. The objectives were set up in a manner that they would assist in confirming or rejecting the hypothesis.

1.4.1 RESEARCH AIM

This study aimed to identify whether less expensive and time-consuming alternatives to non-destructive micro-CT scanning techniques are available for locating pores and defects in parts.

1.4.2 RESEARCH OBJECTIVES

The following objectives were set for the successful completion of this study:

1. Manufacture test specimens.
2. Induce crack propagation in test specimens.
3. Analyse the failure point of the test specimens.
4. Set up a database for cause of failure.

1.5 RESEARCH METHODOLOGY

The research methodology outlines the steps that were followed to achieve the study's objectives and which assisted in testing the hypothesis stated above.

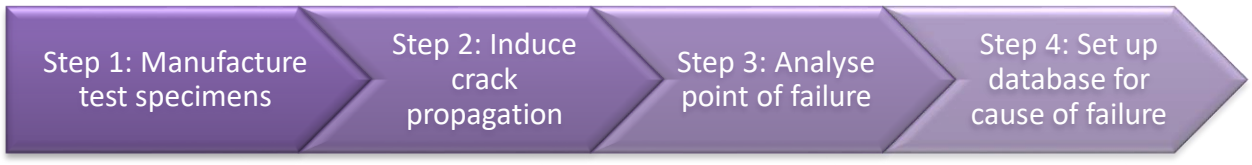

Figure 1.5-1: Flow chart for research methodology

STEP 1: Manufacture test specimens

The test specimens were manufactured according to ASTM E606 standards. Researchers [4] indicate that these samples are provided with a uniform-gage test section, and also noted the critically stressed volume in these specimens to be greater than in regular hourglass specimens. The consequent undesirous effects of manufacturing defects, thus mainly the pores and surface cavities, are more likely to present themselves during fatigue tests. These specimens were manufactured in Bloemfontein at CUT's CRPM facility using the EOS M280 machine.

STEP 2: Induce crack propagation in test specimens

The MTS Landmark machine was used to complete this part of the study. Fatigue tests were carried out over a number of cycles that resulted in the failure of the specimens. The entire test was captured on a Digital Image Correlation (DIC) system, the DIC Q-400.

STEP 3: Analyse the failure point of the test specimens

The use of a Scanning Electron Microscope (SEM) allowed the test specimen's point of failure to be captured in a digital image. Analysis of the captured image assisted in identifying any defects that occurred, including their size, during the manufacturing process which may have caused the

test specimen to fail. The use of a Digital Image Correlation (DIC) system helped the researcher identify during which cycle the first signs of strain occurred that resulted in the point of failure.

STEP 4: Set up a data base for cause of failure

Once the tests had been carried out, the results of the SEM images and the DIC were used to set up a data base, which would indicate the fatigue life of the specimen compared to the size of the defect present at the point of failure.

CHAPTER 2

LITERATURE SURVEY

This chapter covers the definition of additive manufacturing, the different methods available for this technology and their application. This chapter also presents a further understanding of metal sintering processes and other topics of importance to this study, including an understanding what fatigue is.

2.1 INTRODUCTION

When a part is designed for use in the engineering industry, one of the most important consideration is the method that will be used to manufacture the part. Manufacturing methods most commonly used are categorised into three groups. Figure 2.1-1 below shows the three manufacturing methods that can be applied. The use of **formative manufacturing** is used where high volumes of the same part must be manufactured. This method requires a large initial investment in tooling to create the moulds; however, once the moulds are manufactured, the parts are produced quickly and at a low cost per unit. **Subtractive manufacturing** is the preferred method for manufacturing parts with simple geometry in low to medium volumes. The third primary method of manufacturing is **additive manufacturing,** which is used for more complex parts that are produced in lower volumes. The following literature survey aims to provide a better understanding of the main contributing factors of AM in this study.

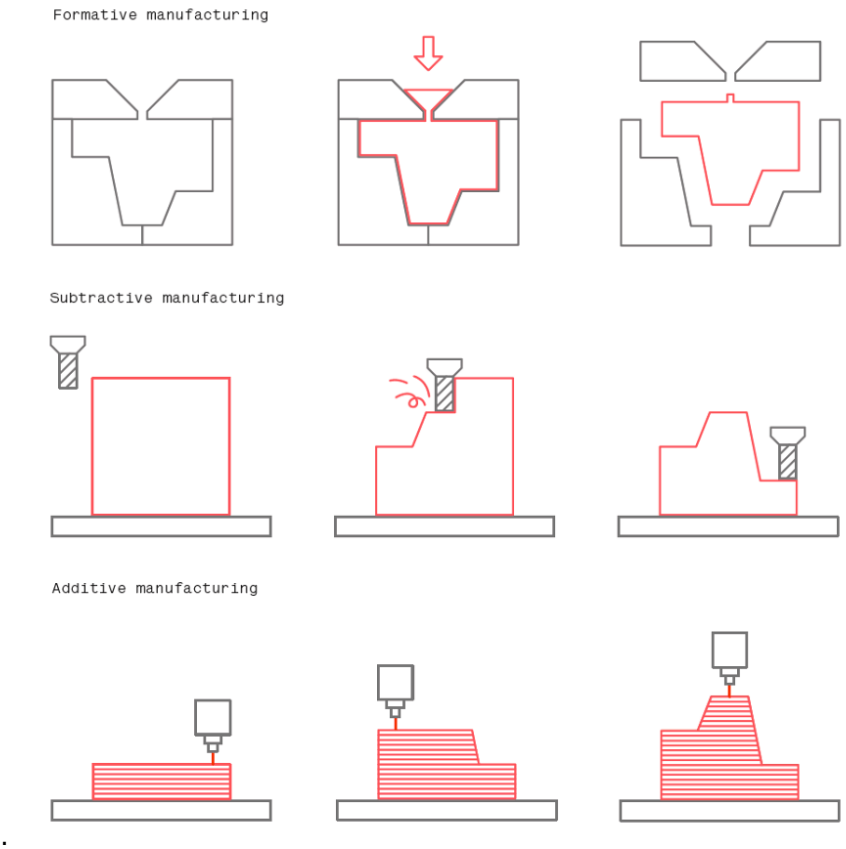

Figure 2.1-1: Comparison of the three manufacturing techniques commonly used [1]

2.2 ADDITIVE MANUFACTURING

Additive manufacturing (AM) is the process of building parts in layers through material deposition. Other conventional methods of fabricating parts include milling a workpiece from a block of material; however, the AM process involves building up a part layer by layer using materials that are preferably in a fine powder form. Additive manufacturing is arguably most commonly used in conjunction with rapid prototyping, which is the construction of a functional prototype for illustrative purposes. This construction helps manufacturers in the industry to create a distinctive profile based on the customer's needs with a cost-saving potential and the ability to meet sustainability goals [5].

The benefits related to the use of AM as a manufacturing technique are multiple. One of the biggest advantages of AM is its ability to manufacture parts of almost any geometry [6]. This technology allows for a design-driven manufacturing process where the design determines the production and not the other way around as with conventional manufacturing techniques. These complex geometries are also comparatively light weight whilst being just as strong [5].

However, as expected, AM also has several limitations. The inability of AM to produce parts that have the same material properties as those manufactured using conventional methods is

arguably one of the greatest limitations. Limitations inherent to AM includes anisotropy, or parts that are not equally strong in all directions, and the repeatability of manufacturing that is influenced by deviations that can occur due to differential cooling or warping during curing [6].

An important factor to consider when deciding on AM as a manufacturing technique for a specific part is the cost comparison with other techniques. Figure 2.2-1 shows the comparison of the cost per part between the different techniques, having taken into consideration the number of parts that must be produced [6].

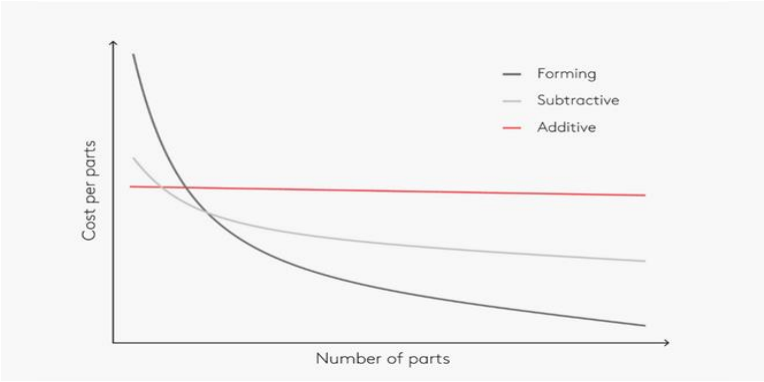

Figure 2.2-1: Cost comparison for different manufacturing techniques [1]

The AM process generally has five steps. The first step is to create a digital model, for which the most common method is to design a part using computer-aided design (CAD) software. Figure 2.2-2 below shows a 3D model that has been generated using a CAD program.

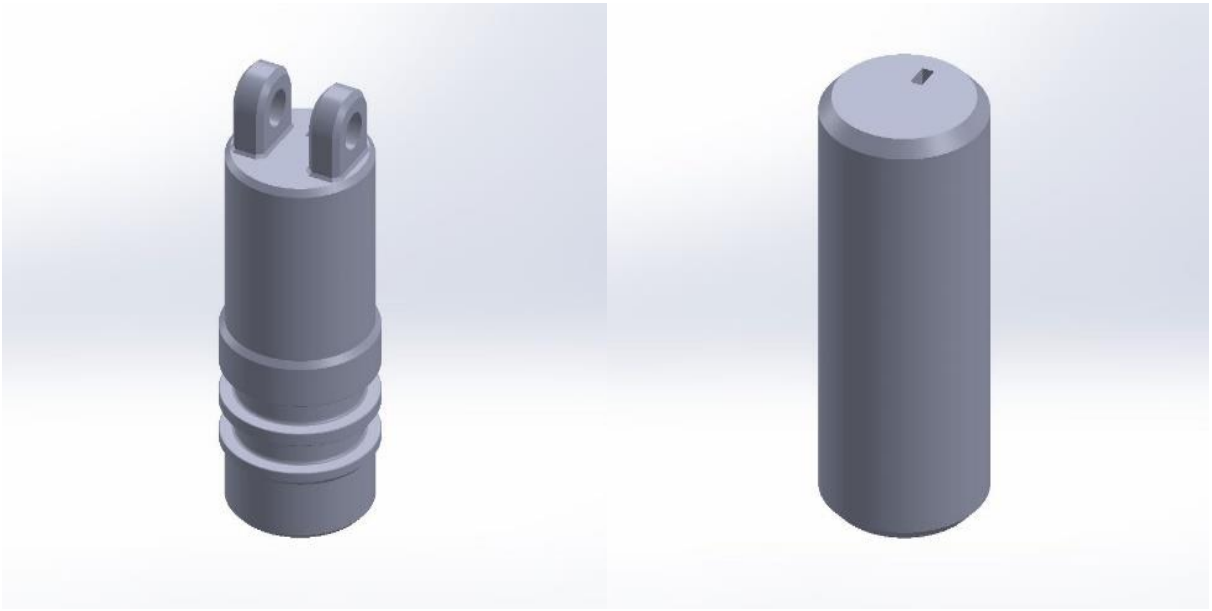

Figure 2.2-2: 3D models of parts manufactured through AM

The second step is to convert the CAD model into a STL (STereoLithography) file. This is done in order for the 3D printer to interpret the 3D model. The STL file is also referred to as Standard Triangle Language, which uses triangles (tessellations) to describe the surfaces of an object and thus in essence simplify the CAD model. A slicing program is used to slice the 3D model in to 2D slices/layers, and the STL file is converted into G-code. G-code is a numerical control programming language used in CAM to control automated machines like 3D printers. The slicing software is also where the machine operator defines the printer build parameters and specifies properties such as support location, layer height, and part orientation [6].

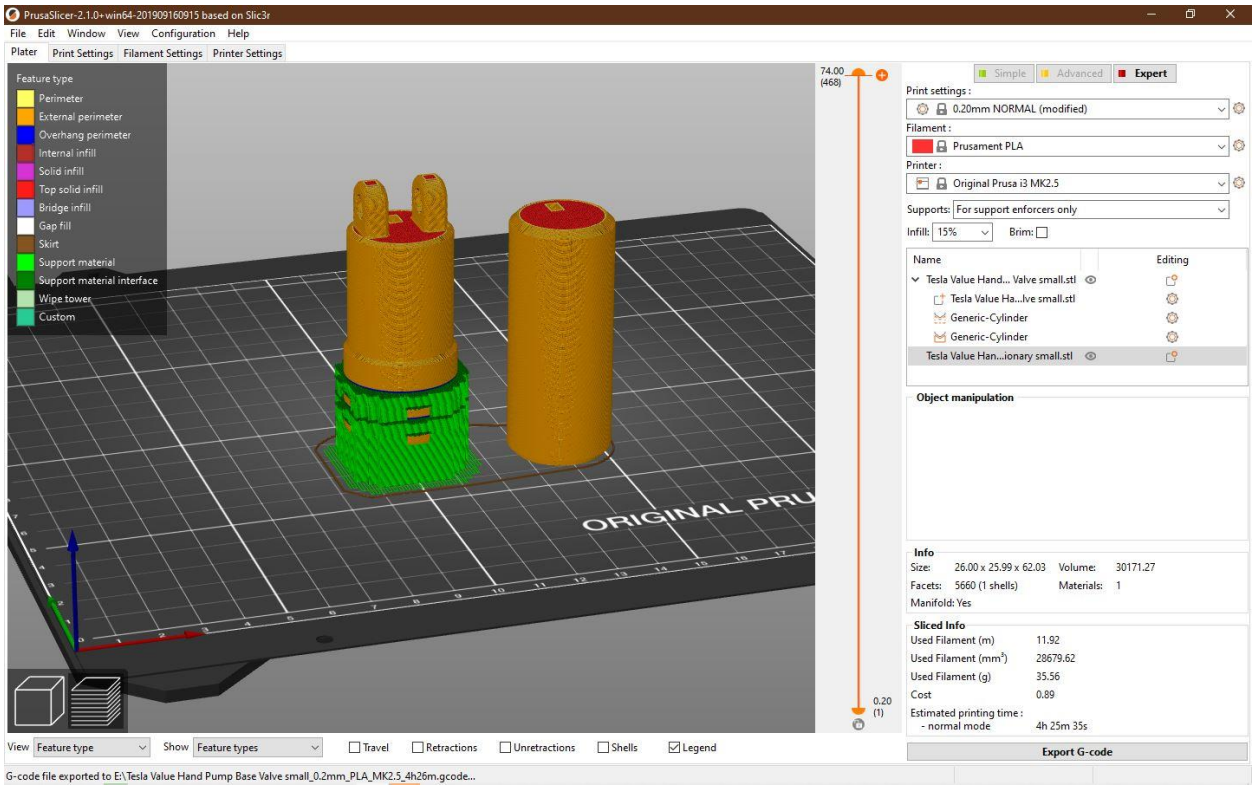

Figure 2.2-3: CAD file sliced using PrusaSlicer 2.1.0

The third step in the process is to upload the G-code on the printer, start the print and wait for the part's completion.

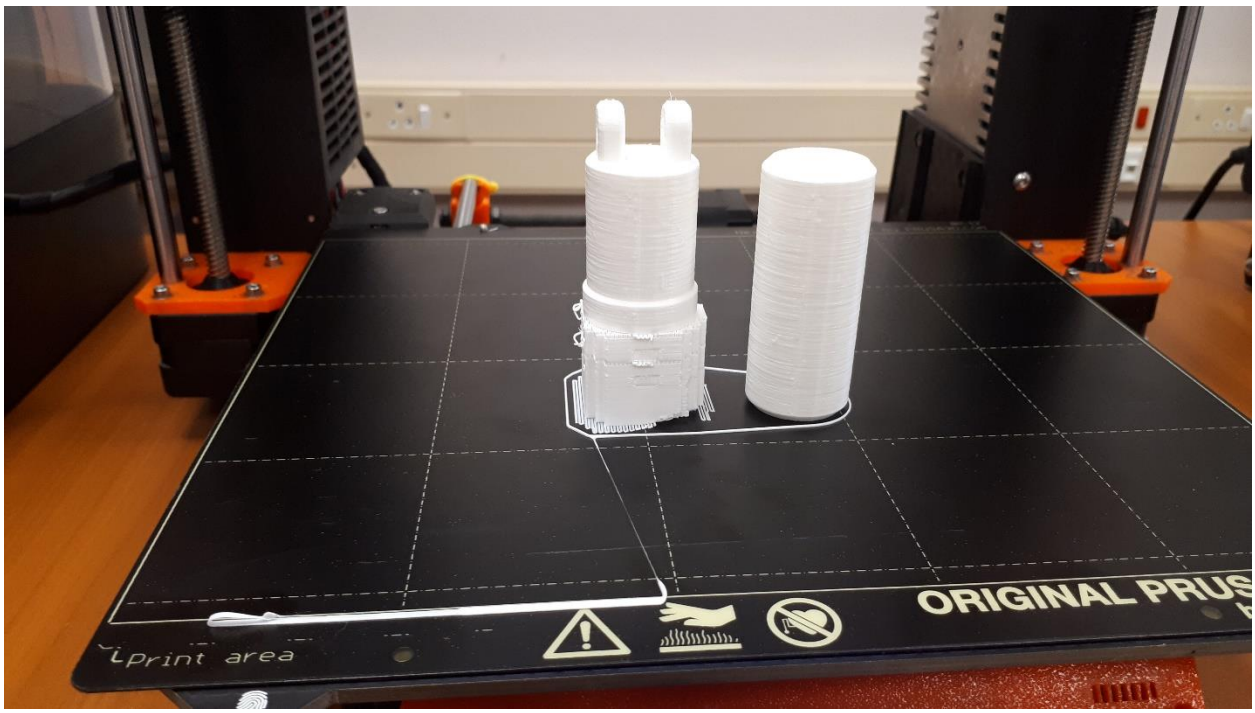

Figure 2.2-4: CAD file printed with support material included

The part's removal is the fourth step in the AM production of a part. Some parts only need to be removed from the build platform, while others require post-processing in the form of removing support material. Depending on the type of AM method used, more intricate skills and tools might be required to remove the support material. The necessary safety equipment are therefore also required to work in a controlled environment.

Figure 2.2-5: Support material removed from parts

The fifth and final step in the AM process is curing an additively manufactured part. These procedures differ from one method to another (see Chapter 2.5 for more details regarding post-processing).

2.3 DIFFERENT TYPES OF AM

The following section gives the reader an insight into technologies commonly used in AM. Thus follows a summary of each of the most commonly used 3D-printing technologies, including their respective applications, benefits, and limitations.

Material extrusion is the process of manufacturing parts by extruding or dispensing material through a nozzle. This technology is more commonly known as fused filament fabrication (FFF) or fused deposition modelling (FDM). Table 2-1 gives a summary of the benefits, limitations, and applications of the material extrusion process as found in [6].

Table 2-1: Benefits, limitations, and applications of the material extrusion process [6]

MATERIAL EXTRUSION	
Benefits	1. Low-cost materials and machines. 2. Ease of operation. 3. Most common choice for rapid prototyping.
Limitations	1. Anisotropic nature of parts. 2. Layer-by-layer building causes parts to be weaker in one direction. 3. Mostly requires some form of post-processing for a smooth surface.
Applications	1. Investment casting patterns. 2. Electronics housings. 3. Form and fit testing. 4. Jigs and fixtures.

VAT Polymerization is the process in which a liquid photopolymer is selectively cured in a vat by light-activated polymerization. Usually, ultraviolet (UV) light is used to cure the parts once they have been manufactured. The technologies associated with this process is stereolithography (SLA) and direct light processing (DLP). Table 2-2 contains the benefits, limitations, and applications of this process [6].

Table 2-2: Benefits, limitations, and applications of the VAT polymerization process [6]

VAT POLYMERISATION	
Benefits	1. Smooth surface finish. 2. High-dimensional accuracy.
Limitations	1. Photopolymers are brittle. 2. Does not have a high impact strength or durability. 3. Parts have limited life expectancy. 4. A loss of mechanical properties over time occurs.
Applications	1. Injection mould-like prototypes. 2. Jewellery for investment casting. 3. Dental applications. 4. Hearing aids.

Powder bed fusion (PBF) is a process that uses thermal energy in the form of a laser to selectively fuse regions of a powder bed. Selective laser sintering (SLS), direct metal laser sintering (DMLS), selective laser melting (SLM), and electron beam melting (EBM) are all technologies associated with the PBF process [6].

Table 2-3 summarises some benefits, limitations, applications associated with the PBF technologies and, more specifically, the SLS technology and the DMLS / SLM technology. These benefits, limitations and applications can be found in [6].

Table 2-3: Benefits, limitations, and applications of the powder bed fusion technologies [6]

POWDER BED FUSION	
SLS	
Benefits	1. Strong functional parts that can be manufactured. 2. Parts with complex geometries can be manufactured. 3. High level of dimensional accuracy is obtained. 4. Parts have an isotropic nature. 5. Parts can be manufactured without any support material.
Limitations	1. Expensive machines are required. 2. Highly skilled operators are required. 3. High lead time is required due to heating and cooling stages.
Applications	1. Functional parts. 2. Low run part production. 3. Complex ducting (hollow sections).
DMLS / SLM	
Benefits	1. Complex and highly customised parts can be manufactured. 2. Topology optimisation can be done on parts to reduce weight.
Limitations	1. Cost for production is high in terms of the machine and material. 2. The build volume is a restriction.
Applications	1. Dental applications. 2. Medical applications.

Material jetting is a process that works on the basis of material droplets that are selectively deposited and then cured on a build plate. The technologies that can be associated with this process includes material jetting (MJ) and drop-on-demand (DOD) [6].

Table 2-4: Material jetting process' benefits, limitations and applications [6]

MATERIAL JETTING	
Benefits	1. Homogeneous parts are produced. 2. Parts have a very smooth surface finish. 3. Parts are highly dimensional accurate.
Limitations	1. Parts have poor mechanical properties. 2. This is a very expensive manufacturing method. 3. Support material is added as a solid mass which results in wasted material.

Applications	1. Full-colour visual prototypes. 2. Medical models. 3. Injection mould-like prototypes.

Binder jetting is a process where a liquid bonding agent is used to selectively bind regions of a powder bed [6].

Table 2-5: Benefits, limitations, and applications for the binder jetting process [6]

BINDER JETTING	
Benefits	1. No heat present in the manufacturing process, thus no residual stresses are present in the parts. 2. Low operating costs. 3. Large products can be produced.
Limitations	1. Parts have poor mechanical properties.
Applications	1. Full colour models. 2. Sand casting. 3. Functional metal parts.

Another process that is part of the commonly used additive manufacturing techniques is **direct energy deposition**. This process uses thermal energy to fuse layers together by melting the materials they are being deposited. Laser engineering net shaping (LENS) and laser-based metal deposition (LBMD) are technologies associated with this process [6].

Table 2-6: Benefits, limitations, and applications of directed energy deposition

DIRECT ENERGY DEPOSITION	
Benefits	1. Ability to control grain structure to a high degree [7]. 2. Repair work of a high quality is possible [7].
Limitations	1. The prints are low resolution and have poor surface finishing, which requires secondary machining [8]. 2. Limitations are present in printable geometries, as overhangs cannot be printed since no support structures are built [8]. 3. The process is relatively expensive [8].
Applications	1. Repairs and maintenance of structural parts [7].

Sheet lamination is a process where sheets of material are bonded together to form a part. The technologies that make use of this process is ultrasonic additive manufacturing (UAM) and laminated object manufacturing (LOM) [6].

Table 2-7: Benefits, limitations and applications for sheet lamination

SHEET LAMINATION	
Benefits	1. High-speed form of manufacturing [9]. 2. Low costs associated with this method [9]. 3. Ease of handling of material [9]. 4. Sheets are cut at a quicker speed [9].
Limitations	1. Only a limited range of materials can be used in this process [9]. 2. Finishing is dependent on the material and may require post-processing [9].
Applications	1. Investment casting patterns can be manufactured [10]. 2. Concept verification can be done using this method [10]. 3. End-use products can be manufactured [10].

2.4 METAL-SINTERING TECHNOLOGY

This section provides a more in-depth focus on the metal-sintering processes found in AM. This technology is widely investigated for Industry 4.0, as it has more industrial applications.

2.4.1 POWDER BED FUSION (PBF)

PBF processes are better known as **laser sintering** machines. These machines make use of a laser during the manufacturing process. Even though the method of polymer laser sintering is not covered here, it is necessary to be familiar with the principles of the powder bed fusion process. The following extract gives a brief description of what the PBF process entails:

> All PBF processes share a basic set of characteristics. These include one or more thermal sources for inducing fusion between powder particles, a method for controlling powder fusion to a prescribed region of each layer, and mechanisms for adding and smoothing powder layers. The most common thermal sources for PBF are lasers [11].

To obtain an understanding of the powder bed fusion process, polymer laser sintering is described, to which the PBF process is compared. The figure below shows that during the laser sintering process, a thin layer of powder, roughly between 0.075 and 0.1 mm thick, is fused. This powder is spread across the build area using a counter-rotating powder levelling roller.

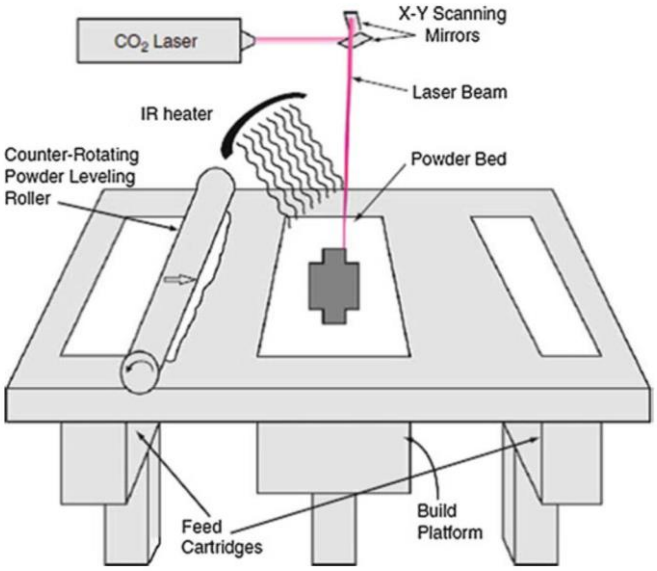

Figure 2.4-1: Schematic drawing showing the selective lase sintering process [11]

The manufacturing of parts happens inside an enclosed chamber where, according to [11–13], nitrogen or argon gas is present to minimise the oxidation and degradation of the powdered material. According to [11, 12, 14], the powder in the build platform is maintained at a temperature which is elevated, to reduce the residual stresses and to prevent warping of the part during the manufacturing process.

After the powder layer has been preheated and formed, a focused CO_2 laser beam is directed onto the powder bed, following the cross-sectional slice of the part being manufactured and thus fusing the material. The surrounding powder material remains unfused and serves as support material for the following layers that are manufactured. This eliminates the need for secondary support, especially for the polymer laser melting, which is needed in the vat photopolymerization processes. Once a layer has been completed, the build platform is lowered by the preset layer thickness, and a new layer of powder is laid and levelled. The laser is again directed onto the powder, thus fusing the cross-sectional slice to the previous one. This process is repeated until the part's completion.

After the print is completed, a cool-down period is usually required, which allows the part to cool down uniformly to a temperature that is cool enough so that it can be handled and exposed to the ambient temperature. Where no provisions are made for this, the parts may degrade when

exposed to oxygen and may also warp as a result of uneven thermal contraction. Once this has been completed, the parts are removed and post-processing operations are carried out where necessary [11].

The **metal laser sintering** can process a wide variety of metals using PBF. In general, any metal that can be welded is considered to be a good option for the PBF process of AM. These metals include stainless steel, tool steel, titanium as well as its alloys, nickel-based alloys, some of the aluminum alloys, and cobalt-chrome [11].

Alloys that crack under high solidification rates are not a good option for the metal laser sintering process. This is, arguably, due to its high solidification rates, as the crystal structures produced and the mechanical properties obtained are different than those for other manufacturing processes [11].

Several different applications are associated with PBF, and [12, 13, 15] note that one of the most common industries where this technology is used is the aerospace industry. Both [12, 15] note that this technology can be applied in the medical industry, more specifically the biomedical industry. Other industries that could benefit from this manufacturing process is the automotive industry, as noted in [12].

Figure 2.4-2: GE's fuel nozzle, which has been additively manufactured [12]

2.4.2 DIRECT ENERGY DEPOSITION

Direct energy deposition (DED) is generally known as a "metal deposition" technology, arguably because of its being predominantly used for metal powders, even though this approach can also work for polymers and ceramics. This process works on the basis of melting material as it is deposited [11].

During the DED process, energy is directed onto a narrow and focused region to heat a substrate. This melts the substrate and simultaneously melts the material that is being deposited into the substrate's melt pool. It is important to note that, unlike PBF techniques, this process of DED does not melt material that is pre-laid in a powder bed but rather melts material as it is being deposited. [11].

A laser or electron beam is typically used as the focused heat source to melt the feedstock material and build up the three-dimensional objects in a similar manner to extrusion-based processes. To create complex three-dimensional geometries, support material, or a multi-axis deposition head is required – as each pass of the DED head creates a line of solidified material, the adjacent lines of deposited material create the layers [11]. The figure below gives a schematic representation of the DED process.

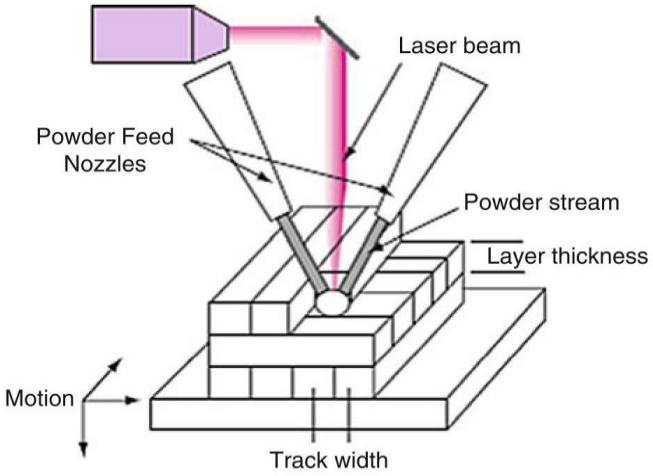

Figure 2.4-3: Schematic of the laser powder DED process [11]

High-density parts are obtained during this manufacturing process due to a traveling melt pool where powdered material is deposited, melted, and solidified [11].

The deposition head is an integrated collection of laser optics, powder nozzle(s), inert gas tubing and, in some cases, sensors. The substrate onto which powder is deposited can either be a flat plate, which is typically the case when new parts are manufactured, or an existing part onto which additional geometry is added. The deposition is controlled by the differential motion between the substrate and the deposition head. It is easier to accurately control the motion of the deposition head for larger parts. On the other hand, if the substrate has a simple geometry, say, for instance, a flat plate, then it is easier to move the substrate and not the deposition head. In some cases it is necessary to combine the movement of the substrate and the deposition head, which accommodates for four- or five-axis systems through the use of either rotary tables or robotic arms. Vertical deposition is also possible, as the kinetic energy of the powder particles moving

through the powder nozzle into the melt pool is greater than the effect of gravity on the powder particle during its flight [11].

The applications for this technology mainly include being used as a welding technology as noted in [16] but can also be used to manufacture end-use products.

2.4.3 ELECTRON BEAM MELTING

Electron beam melting (EBM) uses a high-energy electron beam to induce fusion between metal powder particles. This makes EBM a successful approach to PBF [11].

As with the MLS process, the EBM process entails a focused electron beam that scans across a thin layer of pre-laid powder. This causes localised melting and re-solidification of each slice of the cross section. There are numerous differences between the two processes, which are summarised by Gibson et al. [11] in Table 2-8 below. The differences are arguably due to the EBM process having an energy source consisting of electrons. Other differences are attributed to engineering trade-offs. The figure below shows the schematic illustration of how the EBM process works [11].

Table 2-8: Differences between EBM and MLS [11]

CHARACTERISTIC	EBM	MLS
THERMAL SOURCE	Electron beam	Laser
ATMOSPHERE	Vacuum	Inert gas
SCANNING	Deflection coils	Galvanometers
ENERGY ABSORPTION	Conductivity-limited	Absorptivity-limited
POWDER PREHEATING	Use electron beam	Use infrared or resistive heaters
SCAN SPEED	Very fast, magnetically driven	Limited by galvanometer inertia
ENERGY COSTS	Moderate	High
SURFACE FINISH	Moderate to poor	Excellent to moderate
FEATURE RESOLUTION	Moderate	Excellent
MATERIALS	Metals (conductors)	Polymers, metals and ceramics
POWDER PARTICLE SIZE	Medium	Fine

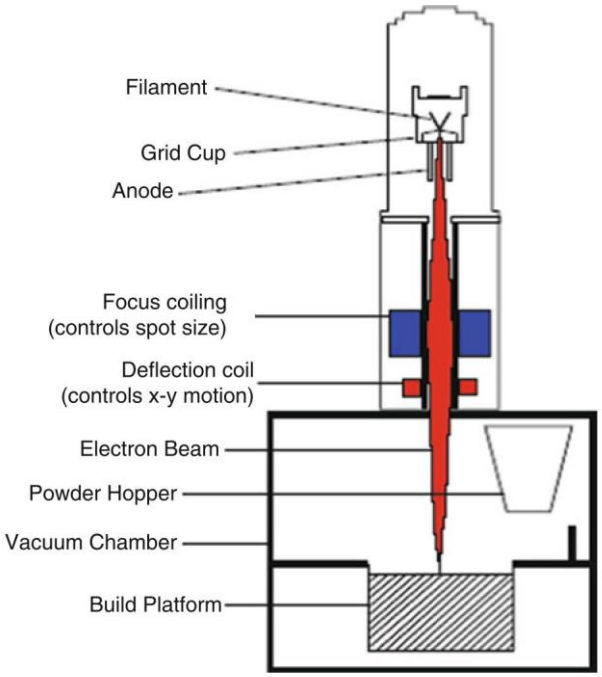

Figure 2.4-4: Schematic illustration of the EBM process [11]

During the EBM process, the electron beam is used to heat the metal substrate at the bottom of the build platform before the powder is laid down. The bed is preheated by defocussing the electron beam and then scanning it rapidly over the build surface of the substrate. Preheating is also done on the metal powder for subsequent layers that must be manufactured. Therefore, it is possible to preheat the bed uniformly to any preset temperature [11] [17]. Ensuring that the powder bed is maintained at an elevated temperature results in a part being manufactured with a microstructure that is significantly different from a part manufactured using the MLS process [11].

As with the PBF process, this technology has different applications in the medical, automotive, and aerospace industries, as noted in [12, 15, 18]. The PBF process is used in the aerospace industry for structural members, for the automotive industry it is used in the form of heat exchangers, and for the medical industry it is used for implants.

2.5 HEAT TREATMENT OF AM PARTS

This section seeks to shed light on the post processing heat treatments that can be done on parts that have been additively manufactured. Residual stresses build up during the manufacturing process, which, in turn, causes parts to warp, thus rendering the parts unusable. The aim of the heat treatment is to reduce the residual stresses present in the parts.

The as-built condition of the test specimen entails no post-processing, such as polishing, of the specimen, but only to **stress-relieve** the specimen. The stress-relieving process consists of a

cycle that starts at room temperature. A vacuum or an argon-filled furnace is used to minimise the changes of oxidation of the part during the heat treatment. The furnace is ramped up to 650ºC in three hours. Depending on the part's wall thickness, the part is then kept at 650ºC for approximately three hours. The cooling rate is then set to 200ºC per hour. The cooling-down rate and the heating-up rate must be constant, otherwise residual stresses can be reintroduced into the part. Figure 2.5-1 demonstrates the stress-relieving cycle.

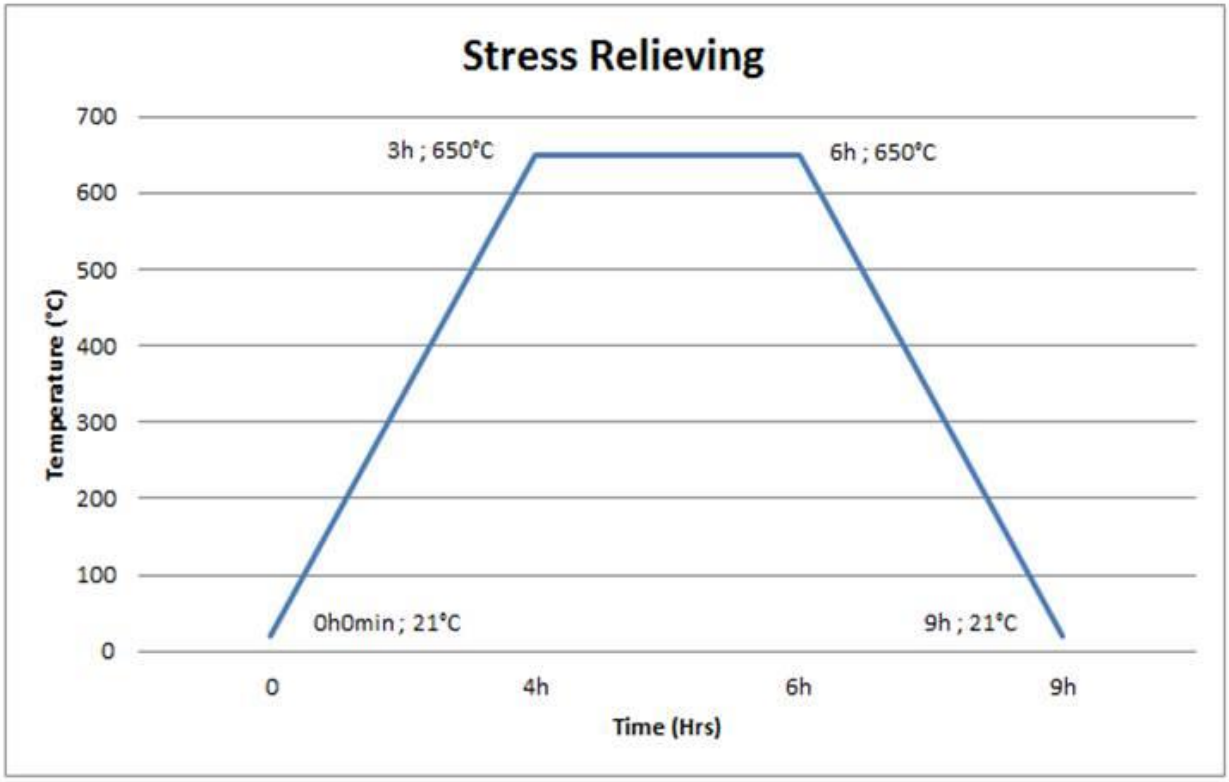

Figure 2.5-1: Stress relieving cycle

Another heat-treatment process that can be done on the test specimen after it has been manufactured is a process called **hot isostatic pressing (HIP)**. As mentioned in Chapter 1, pores can occur inside the micro structure and will cause a concentration of stress when a load is applied to the part. One of the few things that can be done to reduce, or in some cases even close, the pores is the HIP process. The component, in this case a test specimen, is heated in a furnace to a temperature slightly below the melting point, which is then deformed plastically by the application of high pressure, which ensures that the part has a higher density [19].

In [19] it is noted that an external supplier carried out the HIP process at a temperature of 920 ºC, a pressure of 1000 bar and subjected it to an isothermal step of two hours.

It is also possible to **anneal** the parts once they have been manufactured. This must be done between 550 ºC and 1000 ºC, as noted in [20], because some negative effects, which include age

hardening and excessive grain growth, occur outside the range of these temperatures. During tests done in [20], the annealing process was carried out at 600 ºC and 800ºC respectively for two hours with a cooling-down stage in the furnace environment.

2.6 PROPERTIES OF AM PARTS

This section of the literature seeks to give more insight into the different types of properties of parts that have been manufactured using the additive manufacturing technique. These properties include chemical properties, physical properties as well as mechanical properties.

The **chemical properties** of a metal have an influence on, among other things, the corrosion resistance and oxidation resistance of the relevant metal and are related to the chemical composition of the metal and not the microstructure [21]. The chemical composition of the Ti-6Al-4V metal powder is indicated in the table below:

Table 2-9: Chemical composition of Ti-6Al-4V powder

Chemical composition wt. (%)								
Element	N	C	H	Fe	O	Al	V	Ti
wt. (%)	0.01	0.01	0.002	0.20	0.09	6.26	4.1	Balance

The **physical properties** of a metal are related to the physics and crystal structures of the metals. The physical properties that are most commonly known are the Young's modulus, also known as the modulus of elasticity (E), the shear modulus (G), the bulk modulus (K), and Poisson's ratio (υ) [21].

The **mechanical properties** are properties that vary with the microstructure of the metal, and the microstructure can vary depending on the chemical composition and the mechanical work done on the metal and whether or not it has been heat treated. The important mechanical properties mentioned in [21] include:

- hardness,
- tensile strength,
- toughness,
- elongation,
- impact strength,
- fatigue strength,
- wear resistance strength.

Each of the mechanical properties mentioned has specific tests which can be done according to a specified standard test method to determine the strength of the material with regards to a specific mechanical property.

2.7 MECHANICAL FATIGUE TESTING

This section discusses fatigue testing, especially laboratory fatigue testing, including what the test entails and important information that can be obtained from doing the test.

Fatigue occurs when a material is subjected to constant and repeated cycles of stress or strain. This causes the structure of the material to break down, which ultimately leads to fractures. It is important to note that when a fracture or failure of the material occurs in parts, it occurs at a stress that is less than the material's yield stress [22] [23].

According to [23], fatigue fractures are caused by a combination of factors, namely the cyclic stress, tensile stress and plastic strain that are in action during the test. It is also noted that if any one of the three factors are not present, then fatigue cracking will not initiate and propagate. It should therefore be clear that the process of fatigue arguably consists of three stages. The first stage of fatigue is where the cyclic stress causes the initial fatigue damage, which results in crack initiation. The second stage is where the tensile stress produces crack propagation (growth) until the remaining uncracked cross section of the test specimen becomes too weak to sustain the loads imposed on it. The final stage is the sudden fracture of the remaining cross section [23].

This type of failure is arguably the result of the presence of microscopic regions, usually on the surface of the member, where the localised stress far exceeds the average stress acting over the cross section of the member. When this greater stress is then subjected to cyclic stresses, minute cracks begin to form. The formation of these cracks further increases the stress concentration at either the tips or boundaries of the cracks. These stress concentrations extend the cracks further into the member as cyclic stresses are still present. At a certain number of stress cycles, the cross-sectional area of the member is reduced to the point where the load can no longer be sustained, which eventually results in the sudden failure of the part. Under these conditions it is noted that even materials known to be ductile behave as though they were brittle [22].

For fatigue crack initiation in most laboratory fatigue tests, the stress is usually cycled either between a maximum and a minimum tensile stress or between a maximum tensile stress and a maximum compressive test. The stress ratio is the first essential piece of information that can be obtained. The stress ratio is the algebraic ratio of two specified stress values in a stress cycle. The first of the two most commonly used stress ratios are the ratio A, which is the ratio of the

alternating stress amplitude to the mean stress ($A=S_a/S_m$) and ratio R, which is the minimum stress to the maximum stress ($R = S_{min}/S_{max}$).

The necessity to specify a safe strength for a metallic material under cyclic loading requires that a limit be determined where no evidence of failure can be detected after applying a load for a number of cycles. This limiting stress is known as either the endurance limit or the fatigue limit. Using the appropriate testing apparatus, a series of test specimens are subjected to a specified stress and cycled to failure. The results from these tests are plotted as a graph representing the stress ***S*** (or σ) as the ordinate and the number of cycles-to-failure ***N*** as the abscissa. This type of graph is called an S-N diagram or a stress-cycle diagram, where the number of cycles are plotted on a logarithmic scale since the values are normally quite large [22].

The following figure shows examples of S-N diagrams for steel and aluminum. The endurance limit is that stress for which the S-N graph becomes horizontal or asymptotic [22].

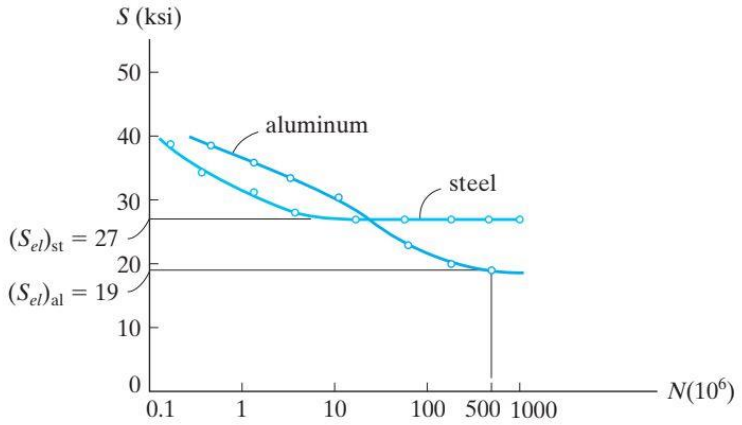

S–N diagram for steel and aluminum alloys (*N* axis has a logarithmic scale)

Figure 2.7-1: S-N diagram for steel and aluminum alloys [22]

2.8 ANALYSING OF CAVITIES AND OTHER CHARACTERISTICS

This section of the literature focuses on systems used to identify defects in AM parts. The main focus is on the pores that are present in AM parts and the strain concentration during the fatigue test.

X-ray micro-CT makes use of X-rays which irradiate a sample, and it measures the subsequent absorption X-ray image and acquires these images constantly as the sample rotates. The X-ray images of the absorption represent views of the sample from different angles, and the penetration of the X-rays provides internal data. The images are then used in a mathematical reconstruction process to generate a volumetric dataset. This volume consists of voxels (volumetric pixels), where the brightness of each pixel is related to the X-ray density of the material.

The schematic below demonstrates the fundamentals of the process, and is a representation of a typical laboratory micro-CT setup with a microfocus X-ray source, a rotating sample, a planar detector, and integrated software that is used for acquiring the images and reconstructing of the volumetric data. Once the scanning and reconstruction has been completed, further data analysis and visualization is performed. This is usually done using dedicated software. As can be seen in the schematic a CT slice image was taken showing the presence of remaining powder [24].

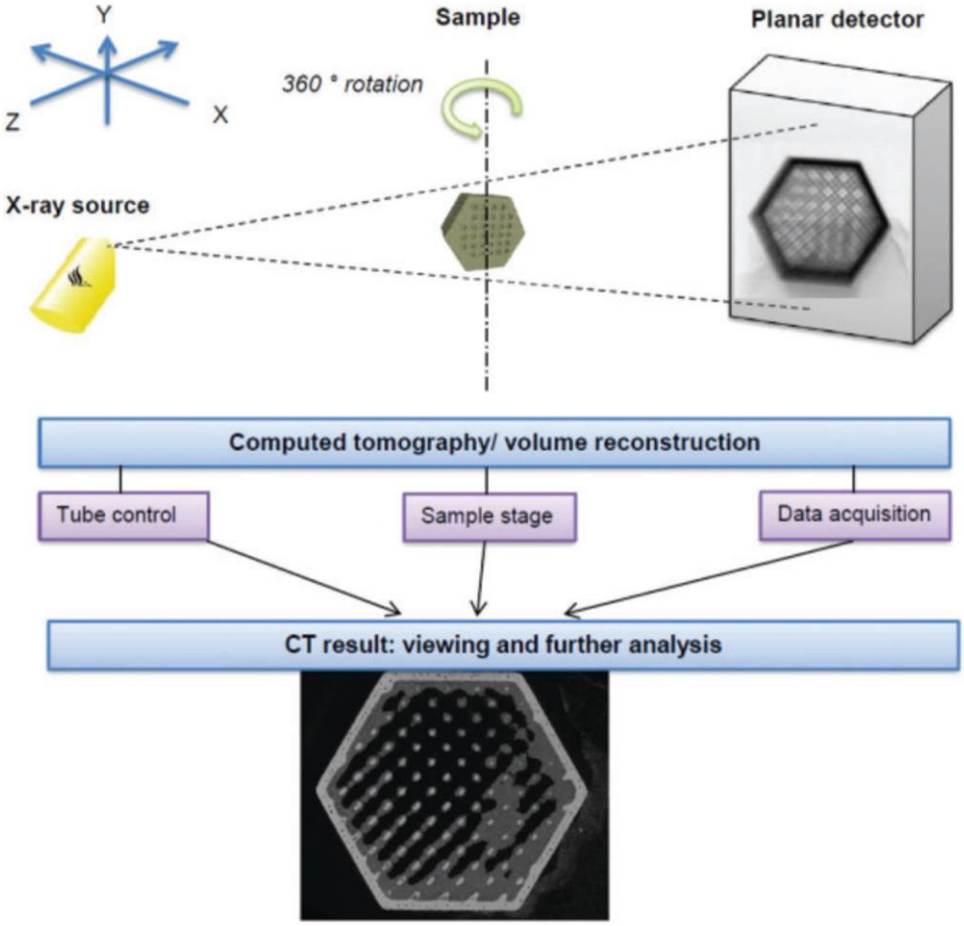

Figure 2.8-1: Schematic showing the process of X-ray micro-CT scanning [24]

Work done in [24, 25] demonstrates how the voids and pores are located inside parts that have been additively manufactured.

The **digital image correlation (DIC)** system used is manufactured by Dantec Dynamics. This measurement system has a wide range of applications and can be used in microscopic investigations on microelectronic or biomedical materials. It can also be used for large scale measurements, such as aerospace, automotive, marine, railway and civil engineering/infrastructural components [26].

For mechanical engineering, the applications include the principles of physics for analysis, design, manufacturing and maintenance of mechanical systems. The application areas include material

strength, instrumentation and measurement, kinematics and dynamics, engineering design, and simulation [26].

The principle of digital 3D correlation entails determining an object's deformation through observation with CCD (charged coupled device) cameras, which are sensors used in digital cameras to capture still and moving images. The digital image correlation process determines the shift of small-faceted elements determined in the reference image. Such correlation algorithms can determine the maximum displacement with an accuracy of up to 1/100 pixel [27].

Work done in [28, 29] shows how the strain can be detected through the use of a DIC system and how it is visualised.

Scanning electron microscope (SEM) images are used to observe the surface phenomena of materials. The sample that must be analysed is shot in a SEM using high-energy electrons, and the outcoming electrons/X-rays are analysed. These outcoming electrons/X-rays provides information on the topography, morphology, composition, orientation of grains and crystallographic information of a material among others [30].

SEM is an electronic and optical system that consists of the following components [30, 31]:

1. *Electron gun*: The electron gun provides the electron beam, which is capable of varying the energy according to the material need, thus ensuring that the image with the best resolution is obtained with minimum sample charging and damage.
2. *Vacuum*: The vacuum helps to eliminate interactions between electrons and gas molecules, which ensures images with high resolution. The vacuum allocates electron movement along the column devoid of scattering and spreading, and it avoids discharge in the interior gun zone.
3. *Column*: The column consists of a condenser lens, scanning coils, stigmator coils, an objective lens and apertures. All of these components help to focus the electron beam onto the surface of the specimen.

Figure 2.8-2 below shows a schematic diagram of the SEM.

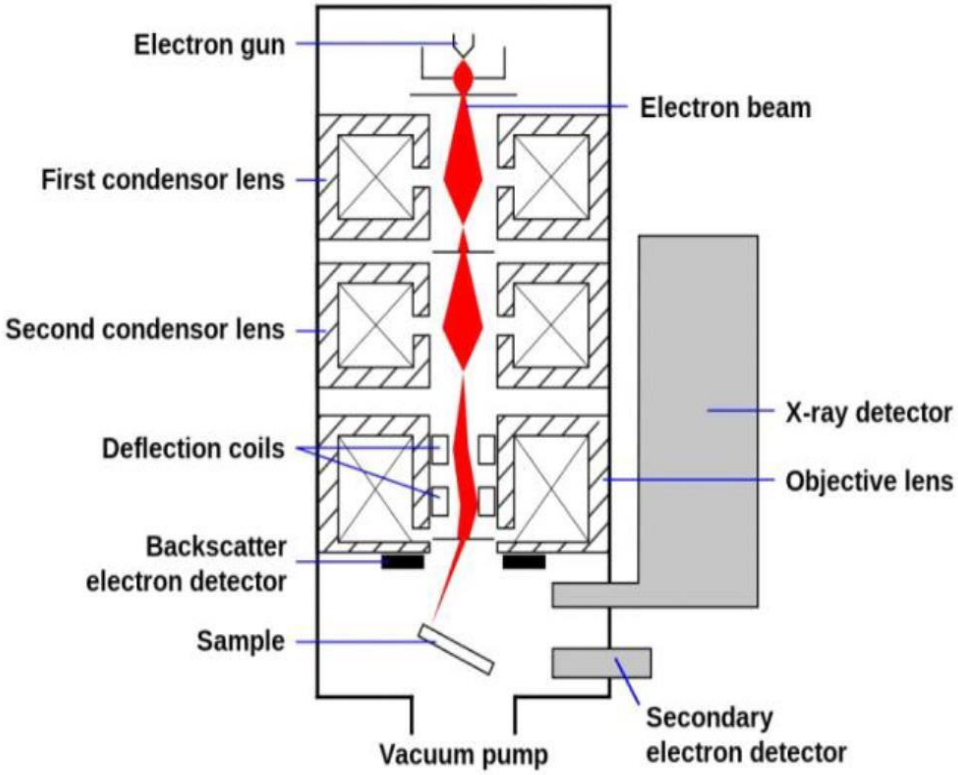

Figure 2.8-2: Schematic diagram of Scanning Electron Microscope [32]

Work done in [4, 33, 34] shows SEM images of the fracture surfaces and the type of defects that occurred at the point of failure for additively manufactured parts after fatigue tests have been completed.

Having worked through the literature and work that other researchers have completed, it is now known that with AM there are many different technologies that are associated with the manufacturing process as well as the analysis process of parts. Therefore, from the literature review, it is evident that with micro-CT scanning being a time-consuming and expensive procedure, an investigation into a possible alternative technique can be developed through the use of a DIC and SEM scanning method to determine where a part will fail.

CHAPTER 3

THEORY

This chapter seeks to shed light on the theory associated with fatigue testing and the calculations that must be considered.

3.1 MATERIAL PROPERTIES

The objective of this section is to understand what the fatigue behaviour is of Ti-6Al-4V, and one of the important steps that must be taken is finding its material properties. Therefore, a tensile test was conducted to establish the material properties of Ti-6Al-4V.

3.1.1 STRESS

The stress (**σ**) that a material experiences can be calculated by taking the force (**F**) acting on a material applied to the cross-sectional (**A**) area where it breaks.

$$\sigma = \frac{F}{A} \qquad \text{(Equation 3-1)}$$

with:

σ – Units: Pascal [**Pa**],
F – Units: Newton [**N**],
A – Units: Squared meter [$\mathbf{m^2}$]

3.1.2 STRAIN

The strain (**ε**) that a material experiences is the percentage elongation of the specimen from its original length ($\mathbf{L_i}$) to the final length at which it breaks ($\mathbf{L_f}$).

$$\varepsilon = \frac{\Delta L}{L_i} = \frac{L_f - L_i}{L_i} \qquad \text{(Equation 3-2)}$$

with:

ε – Units: Unitless [**-**] / percentage [**%**]
$\mathbf{L_i}$ – Units: Meter [**m**]
$\mathbf{L_f}$ – Units: Meter [**m**]

3.1.3 STRESS-STRAIN GRAPH

A stress-strain graph can be constructed when the stress and strain has been obtained from a tensile test. The stress is considered to be the dependent variable as it is plotted on the y-axis and the strain is considered to be the independent variable as it is plotted on the x-axis. Figure 3.1-1 shows the stress-strain graph normally obtained from doing a tensile test.

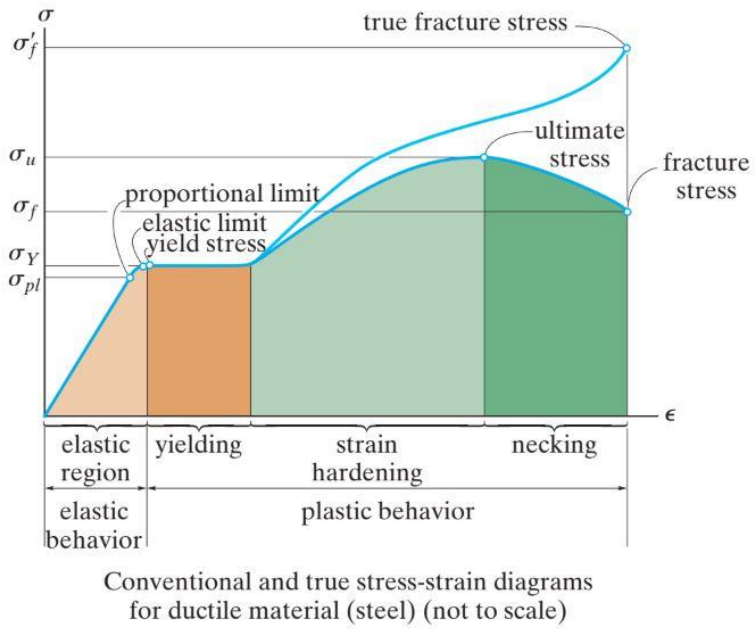

Conventional and true stress-strain diagrams for ductile material (steel) (not to scale)

Figure 3.1-1: The conventional and true stress-strain diagrams for ductile material (steel) [22]

In Figure 3.1-1 above, the stress and strain are proportional over the elastic behaviour region in the graph. It can be considered to be linearly elastic, with the upper stress limit to the linear relationship being called the **proportional limit** (σ_{pl}). Then the curve tends to flatten out and continue until the stress reaches the **elastic limit**. If the load is removed in the elastic region, the test specimen will return to its original shape.

Yielding is the behaviour where an increase in stress above the elastic limit causes the material to permanently deform as the material is broken down. This point on the graph where yielding begins is known as the **yield point** (σ_y).

When the yielding has ended and a further load is applied to the material, the graph rises again before it begins to flatten out until a maximum stress is reached. This maximum stress is known as the **ultimate stress** (σ_u).

Necking occurs when the ultimate stress causes the cross-sectional area to decrease in a localized part of the specimen and not the entire length of the specimen. The resulting decrease

in the specimen's cross-sectional area means that the area can only carry a smaller load. Therefore, the stress-strain diagram will tend to curve downward until the specimen breaks at the **fracture stress** (σ_f). The **true stress** would be calculated if the true (actual) cross-sectional area at the point of failure is measured instead of always using the original cross-sectional area and length to calculate the engineering stress and strain.

3.1.4 MODULUS OF ELASTICITY

The modulus of elasticity (E) represents the equation of the initial straight-lined part of the stress-strain graph up to the proportional limit. The modulus of elasticity is also known as the Young's modulus, and it represents the slope of the straight line in the graph.

$$E = \frac{\Delta\sigma}{\Delta\varepsilon} \qquad \text{(Equation 3-3)}$$

with:

E – Units: Pascal [**Pa**]
σ – Units: Pascal [**Pa**]
ε – Units: Unitless [**-**] / Percentage [**%**]

3.2 FATIGUE

The fatigue failure results from the fact that there are microscopic regions which usually occur on the surface of the member where the localised stress exceeds the average stress acting over the cross section by far. In addition to the knowledge obtained on the material properties, the following properties for a fatigue test should also be known.

3.2.1 WAVEFORM PROPERTIES

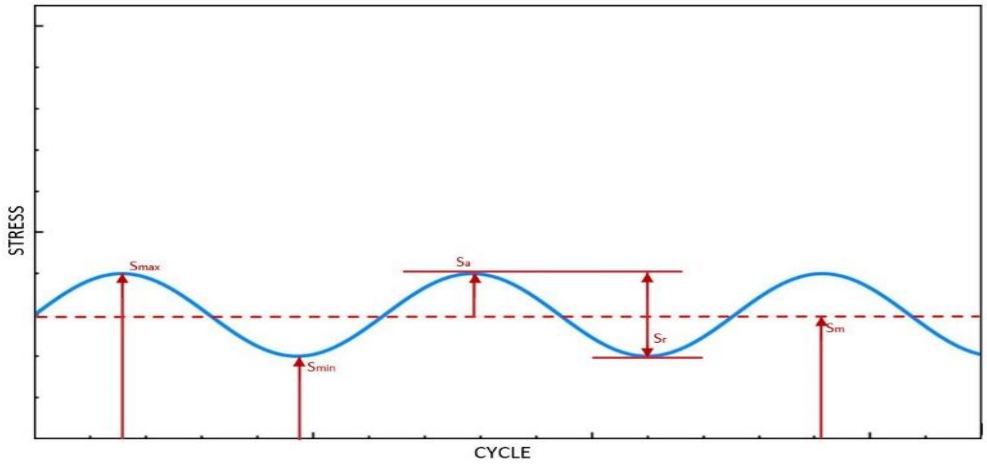

Figure 3.2-1: Stress-cycles waveform [35]

3.2.1.1 STRESS RANGE

The stress range is the difference between the maximum and minimum stress [35].

$$S_r = S_{max} - S_{min} \quad \text{(Equation 3-4)}$$

with:

S_{max} – Maximum Stress
S_{min} – Minimum Stress

3.2.1.2 STRESS AMPLITUDE

The stress amplitude is one half of the stress range [35].

$$S_a = \frac{S_r}{2} = (S_{max} - S_{min})/2 \quad \text{(Equation 3-5)}$$

3.2.1.3 MEAN STRESS

The mean stress is the average of the maximum and minimum stress [35].

$$S_m = (S_{max} + S_{min})/2 \quad \text{(Equation 3-6)}$$

3.2.1.4 STRESS RATIO

The stress ratio is the minimum stress divided by the maximum stress [35].

$$R = S_{min}/S_{max} \quad \text{(Equation 3-7)}$$

3.2.1.5 AMPLITUDE RATIO

The amplitude ratio is the stress amplitude divided by the mean stress [35].

$$A = (1 - R)/(1 + R) \quad \text{(Equation 3-8)}$$

3.2.2 THE STRESS-LIFE METHOD

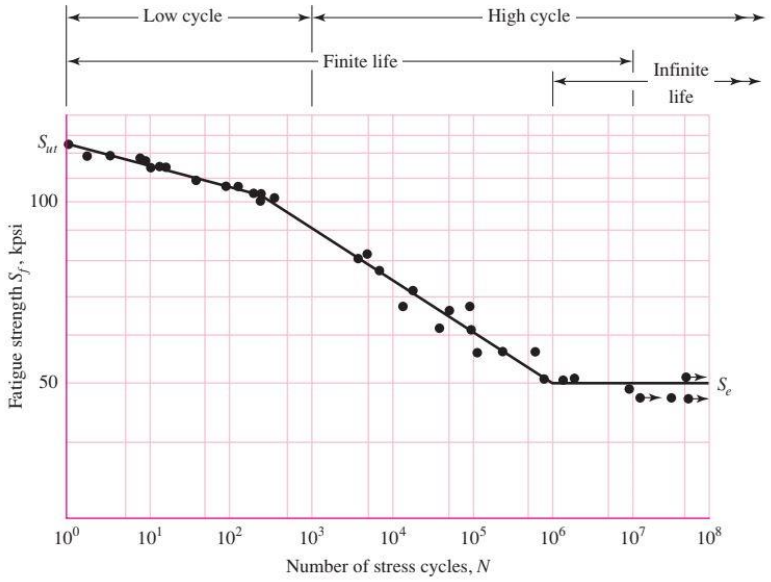

Figure 3.2-2: S-N diagram plotted from results obtained from a completely reversed axial fatigue test [36]

The S-N diagram is obtained from doing a completely reversed stress cycle, during which the stress level alternates between equal magnitudes of tension and compression. **Low-cycle fatigue** is considered to be fatigue failure from N=1 to N=1000 cycles, as indicated in Figure 3.2-2 above. **High-cycle fatigue** is associated with failure corresponding to stress cycles greater than 103 cycles [36].

It is also important to note the **finite-life region** and the **infinite-life region**, as shown in Figure 3.2-2. The number of cycles which define the boundaries of these regions cannot clearly be defined except for a specific material and lies somewhere between 10^6 and 10^7 cycles for steel [36].

3.2.2.1 DESIGN EQUATIONS FOR THE STRESS-LIFE METHOD

Three categories of fatigue problems exist for fatigue testing. The important procedures and equations are presented here:

1. Determine S'_e either from test data or

$$S'_e = \begin{cases} 0.5S_{ut} & S_{ut} \leq 1400\ MPa \\ 700\ MPa & S_{ut} > 1400\ MPa \end{cases} \qquad \text{(Equation 3-9)}$$

2. Modify S'_e to determine S_e.

$$S_e = k_a k_b k_c k_d k_e k_f S'_e \qquad \text{(Equation 3-10)}$$

$$k_a = aS_{ut}^b \qquad \text{(Equation 3-11)}$$

Table 3-1: Parameters for Marin surface modification factor (Table 6-2 [36])

	Factor a		
Surface finish	S_{ut}, kpsi	S_{ut}, MPa	Exponent b
Ground	1.34	1.58	-0.085
Machined or cold-drawn	2.70	4.51	-0.265
Hot-rolled	14.4	57.7	-0.718
As-forged	39.9	272	-0.995

Rotating shaft. For bending or torsion the size factor is noted as

$$k_b = \begin{cases} (d/7.62)^{-0.107} = 1.24d^{-0.107} & 2.79 \le d \le 51\ mm \\ 1.51d^{-0.157} & 51 < 254\ mm \end{cases} \qquad \text{(Equation 3-12)}$$

For axial,

$$k_b = 1 \qquad \text{(Equation 3-13)}$$

Non-rotating member. Use Table 6-3, [36, p.298], for d_e and substitute into Eq. (3-12) for d.

To determine the loading factor, use the following equation:

$$k_c = \begin{cases} 1 & bending \\ 0.85 & axial \\ 0.59 & torsion \end{cases} \qquad \text{(Equation 3-14)}$$

To determine the temperature factor:

$$k_d = 0.975 + 0.432(10^{-3})T_F - 0.115(10^{-5})T_F^2 + 0.104(10^{-8})T_F^3 - 0.595(10^{-12})T_F^4 \qquad \text{(Equation 3-15)}$$

where $70 \le T_F \le 1000°\text{F}$

Use Table 6-5 [36] to determine the reliability factor:

Table 3-2: Reliability Factor ke corresponding to eight percent standard deviation of the endurance limit [36]

Reliability, %	Transformation variate z_a	Reliability factor k_e
50	0	1.000
90	1.288	0.897
95	1.645	0.868
99	2.326	0.814
99.9	3.091	0.753
99.99	3.719	0.702
99.999	4.265	0.659
99.9999	4.753	0.620

3. Determine the fatigue stress-concentration factor, K_f or K_{fs}. First, find K_t or K_{ts} (stress concentration factors), which can be obtained from [36].

$$K_f = 1 + q(K_t - 1) \text{ or } K_{fs} = 1 + q(K_{ts} - 1) \quad \text{(Equation 3-16)}$$

obtain q from either Fig. 6-20 or 6-21 [36]

or alternatively,

$$K_f = 1 + \frac{K_t - 1}{1 + \sqrt{a/r}} \quad \text{(Equation 3-17)}$$

For $\sqrt{a}$ in units of $\sqrt{in}$, and S_{ut} in kpsi

For bending or axial:

$$\sqrt{a} = 0.246 - 3.08(10^{-3})S_{ut} + 1.51(10^{-5})S_{ut}^2 - 2.67(10^{-8})S_{ut}^3 \quad \text{(Equation 3-18)}$$

For torsion:

$$\sqrt{a} = 0.190 - 2.51(10^{-3})S_{ut} + 1.35(10^{-5})S_{ut}^2 - 2.67(10^{-8})S_{ut}^3 \quad \text{(Equation 3-19)}$$

4. Apply K_f or K_{fs} either by dividing S_e by it or multiplying it by the purely reversing stress, but not both.
5. Determine fatigue life constants a and b. If $S_{ut} \geq 490\ MPa$, determine *f* from Fig. 6-18 [36]. If $S_{ut} < 490\ MPa$, let $f = 0.9$.

$$a = (fS_{ut})^2/S_e \quad \text{(Equation 3-20)}$$

$$b = -[log(fS_{ut}/S_e)]/3 \quad \text{(Equation 3-21)}$$

6. Determine fatigue strength S_f at N cycles, or N cycles to failure at a reversing stress σ_{rev}; this applies to purely reversing stresses where $\sigma_m = 0$.

$$S_f = aN^b \quad \text{(Equation 3-22)}$$

$$N = (\sigma_{rev}/a)^{1/b} \quad \text{(Equation 3-23)}$$

3.2.3 THE STRAIN-LIFE METHOD

A fatigue failure almost always begins at a local discontinuity, such as a notch, crack, or other area of stress concentration. When the stress at the discontinuity exceeds the elastic limit, plastic strain occurs. If a fatigue fracture is to occur, there must exist cyclic plastic strains. Figure 3.2-3 has been constructed to show the general appearance of these plots for the first few cycles of controlled cyclic strain. In this case the strength decreases with stress repetitions, as can be seen from the fact that the reversals occur at ever-decreasing stress levels.

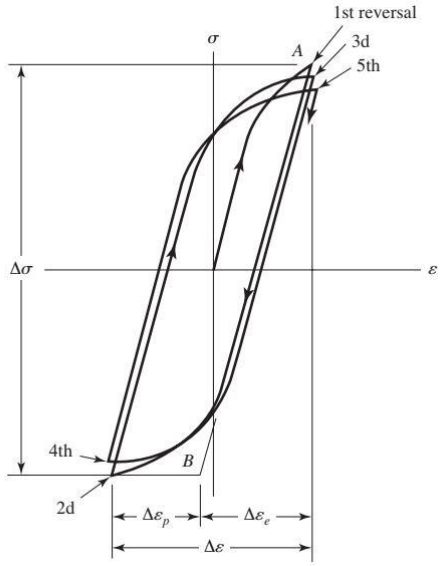

Figure 3.2-3: True stress-true strain hysteresis loop showing five stress reversals of a cyclic softening material [36]

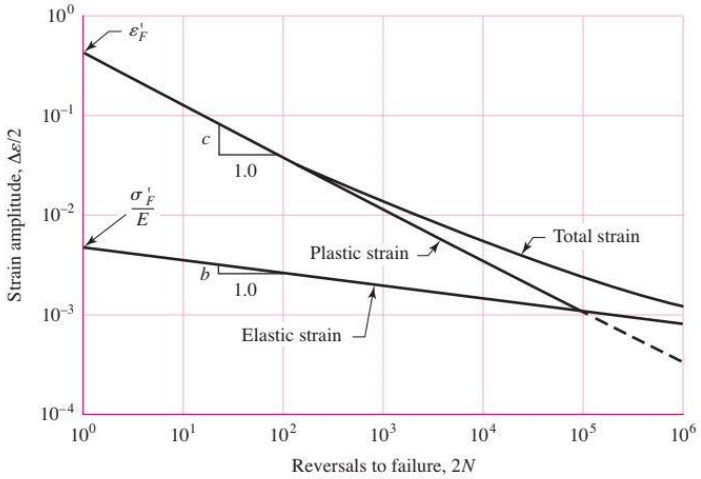

Figure 3.2-4: Log-log plot showing how the fatigue life is related to the true strain amplitude for hot-rolled SAE 1020 steel [36]

A few terms from Figure 3.2-4 require defining. The first term is the fatigue ductility coefficient, ε'_F, which is the true strain corresponding to fracture in one reversal. The fatigue strength coefficient, σ'_F, is the true stress corresponding to fracture in one reversal. The fatigue ductility exponent, c, is the slope of the plastic strain line and is the power to which the life 2N must be raised for it to be proportional to the true plastic-strain amplitude. If the number of stress reversals is 2N, then N is the number of cycles. The fatigue strength exponent, b, is the slope of the elastic-strain line and is the power to which the life 2N must be raised for it to be proportional to the true-stress amplitude.

In Figure 3.2-4 the total strain can be seen as the sum of the elastic and plastic components. The total strain amplitude is thus half of the total strain range:

$$\frac{\Delta\varepsilon}{2} = \frac{\Delta\varepsilon_e}{2} + \frac{\Delta\varepsilon_p}{2} \qquad \text{(Equation 3-9)}$$

The equation of the plastic-strain line in figure 3-5 is

$$\frac{\Delta\varepsilon_p}{2} = \varepsilon'_F(2N)^c \qquad \text{(Equation 3-10)}$$

The equation of the elastic strain line is

$$\frac{\Delta\varepsilon}{2} = \frac{\sigma'_F}{E}(2N)^b \qquad \text{(Equation 3-11)}$$

Equation 3-9 can thus be rewritten to obtain the total-strain amplitude

$$\frac{\Delta\varepsilon}{2} = \frac{\sigma'_F}{E}(2N)^b + \varepsilon'_F(2N)^c \qquad \text{(Equation 3-12)}$$

3.3 VERIFICATION OF THEORY CALCULATIONS AND TESTING RESULTS

Tests done by final year students, Ms Daniella Da Costa [42] and Mr Geo Joubert [43], indicated a good correlation with results from literature with the use of the theory stated above. These tests were carried out on wrought Ti-6Al-4V and Stainless Steel 316. The first set of results are obtained from Ms Da Costa's study and shows how she compared her own results to that obtained from another study done in 2014. The figure below shows a table comparing the two set of results.

Mower's Results		Experimental Results	
Stress	Cycles	Stress	Cycles
950 MPa	10000 $Cycles$	959.22 MPa	34383.5 $Cycles$
850 MPa	700000 $Cycles$	852.64 MPa	513009 $Cycles$
740 MPa	1200000 $Cycles$	746.06 MPa	863964.5 $Cycles$

Figure 3.3-1: Results of fatigue tests

The table shows that in the same range of fatigue life, there are comparable values for the stress a test specimen can endure.

Conclusions made in [43] by Mr Geo Joubert is that the fatigue endurance limit of SS316 as calculated from tests is 469.146 MPa. This also compared well with the results from literature. The stress-life method was used in both tests where the endurance limit was determined through the design equation: $S_e = k_a k_b k_c k_d k_e k_f S'_e$. Stress-strain graphs as well as the modulus of elasticity from each test done was also compared with literature and showed good correlation.

CHAPTER 4

EXPERIMENTAL PROCEDURE

This chapter contains the experimental procedure, test specimen design, equipment used during the study and a discussion of the ASTM standard test method.

4.1 TEST SPECIMEN

The specimen design configuration is in accordance with the ASTM E606 standard [37]. The configuration in Figure 4.1-1 below shows the recommended uniform-gage specimen. The reason for this configuration is that with the other hourglass configuration shown in ASTM E606 standard, careful considerations should be made for problems of data interpretation and anisotropy as well as buckling.

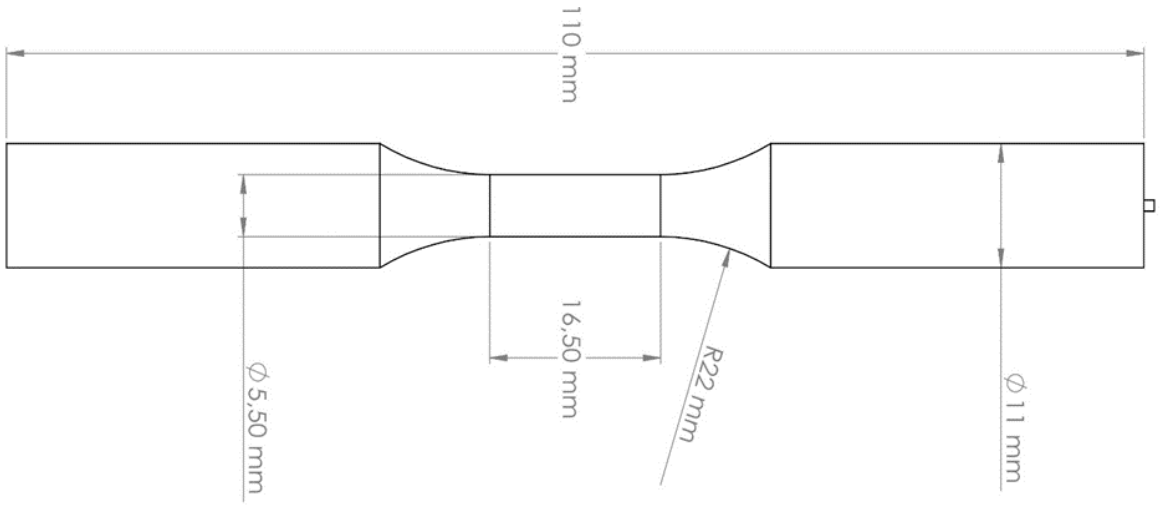

Figure 4.1-1: ASTM E606 test specimen dimensions [8]

This specimen has a solid circular cross section and a minimum diameter of 5.5 mm in this test section. The recommended specific cross-sectional dimensions are shown in Figure 4.1-2 below. The ASTM E606 standard document advises that the minimum diameter should be 6.35 mm, but it also states the following [38]:

> Specimens possessing other diameters or tubular cross sections may be tested successfully within the scope of this test method; however, crack growth rate, specimen grain size, and other considerations might preclude direct comparison with test results from the recommended specimens.

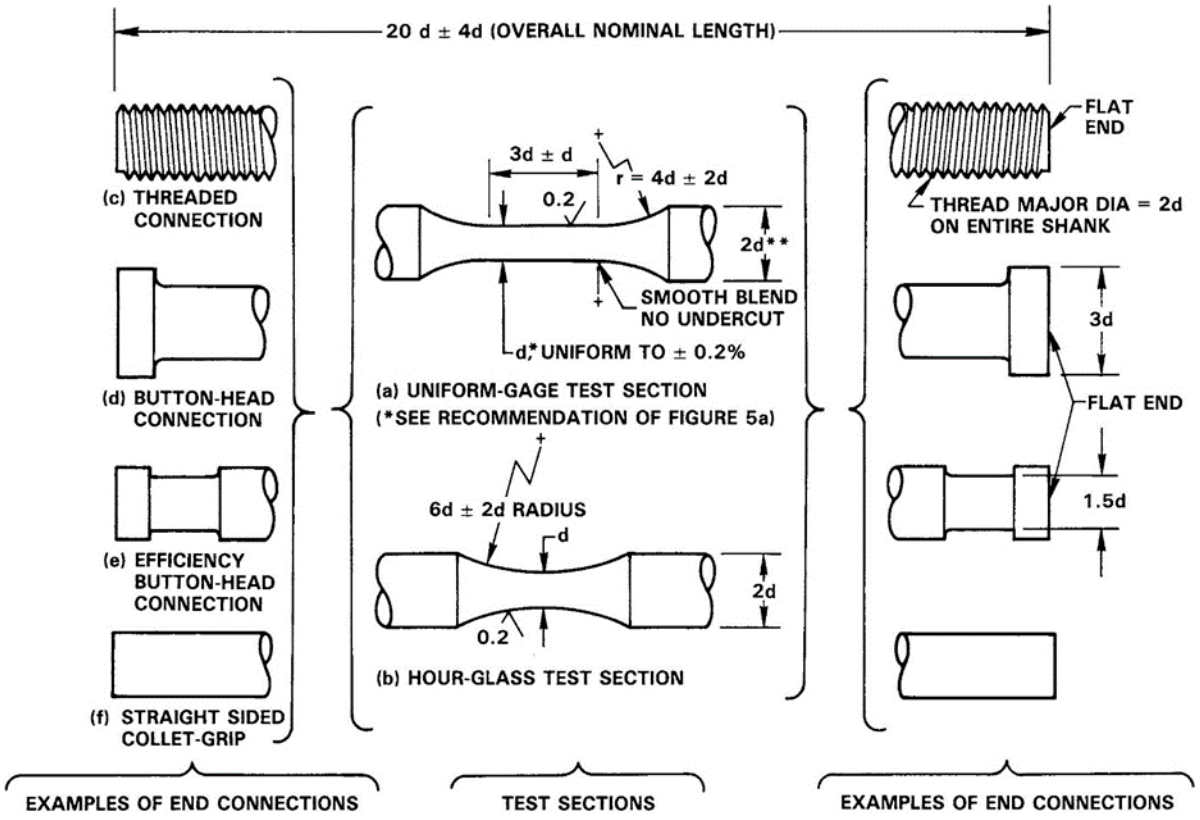

Figure 4.1-2: Recommended low-cycle fatigue specimens [38]

The dimensions for the design of the specimens that were used has been specifically chosen as the MTS Landmark machine does not have clamps to handle test specimens with maximum diameter of larger than 11 mm.

For the specimen preparation it is important that the specimens be prepared by a specific set of procedures known to provide consistent test results. It is important to ensure that the surface of the specimens are protected against oxidation and corrosion during the heat treatment or storage. The storage of the test specimens is important, as they may be susceptible to corrosion in moist room-temperature air. Ways in which storage can take place is by keeping the specimens in a dry, inert gas environment or a vacuum.

The microstructural characteristics such as the composition, grain size, shape of the grain size, as well as the specification designation and heat treatment methods, are important. A description of mechanical properties of the material such as tensile strength, yield strength, ultimate tensile strength, percentage elongation, Poisson's ratio and Young's modulus are desirable. For the true stress-strain properties, the strain hardening exponent and strength coefficient are considered.

4.2 HARDWARE

4.2.1 EOSINT M280

The following table gives the specifications of the machine in [39].

Table 4-1: EOSINT M280 specifications [39]

MACHINE DIMENSIONS (B X D X H)	
System	2200 mm x 1070 mm x 2290 mm
Recommended installation space	min. 4.8m x 3.6 m x 2.9 m
Weight	approx. 1250 kg
MACHINE SPECIFICATIONS	
Building volume (including building platform)	250 mm x 250 mm x 325 mm
Laser type	Yb-fibre laser, 200W / 400W
Precision optics	F-theta-lens , high-speed scanner
Scan speed	up to 7.0 m/s
Variable focus diameter	100 – 500 µm
Power supply	32 A
Power consumption	maximum 8.5 kW
Nitrogen generator	integrated
Compressed air supply	7000 hPa ; 20m^3/h
Argon supply	4000 hPa ; 100 l/min
DATA PREPARATION	
Software	EOSTATE Magics RP (materialise)
CAD interface	STL
Network	Ethernet

4.2.2 MTS LANDMARK

The following table (Table 4-2) gives the specifications of the machine in [40]. The model used is the MTS Landmark 370.10 (Actuator integral to Base).

Table 4-2: MTS Landmark 370.10 specifications [40]

Load frame specifications	Value	Units
Force capacity (rated dynamic force)	100	kN
Available actuator ratings (nominal)	100	kN
Actuator dynamic stroke	150	mm
Min vertical test space – standard height	140	mm
Max vertical test space – standard height	1283	mm
Min vertical test space – extended height	363	mm
Max vertical test space – extended height	1753	mm
Working height	922	mm
Column spacing (test space width)	533	mm
Column diameter	76.2	mm
Base width	1018	mm
Base depth	698	mm
Diagonal clearance – standard height	2580	mm
Diagonal clearance – extended height	3084	mm
Overall height – standard height	2588	mm
Overall height – extended height	3058	mm
Stiffness	467×10^6	N/m
Weight	635	kg

4.2.3 DIC Q400

Sensor:

Type: Correlation system (Q400)

Camera type: 5 MPix

All sensors used are based on FireWire or Gigabit Ethernet Cameras. The 25 mm-lenses are high-resolution lenses manufactured by Schneider Kreuznach, Germany.

The USB3 sensors transfer the data via the USB3 Standard with a maximum bandwidth of up to 5000 Mbit/s.

Control and analysis electronics:

Laptop processor:	Intel Core i7-8850H @ 2.60 GHz
Memory RAM:	16 GB
Hard drive:	500 GB
Graphic board:	Intel(R) UHD Graphics 630
	NVIDIA GeForce MX130

Software:

MS Windows:	Version:	Win 10 Professional 64 bit
	Language:	English
Istra4D:	Version:	4.4.7.667
	Language:	English

HUB Box:

The Timing Box is an interface between the control computer and the sensors. It consists of a DAQ (data acquisition) timing and analog data recording board.

4.3 TEST SAMPLE PREPARATION

Having established which apparatus to use in this study, it is necessary to prepare the test samples for the fatigue testing.

For the purpose of this study, which entails making use of a DIC system, some preparation is needed in terms of a speckle pattern that must be applied to the test samples. It is known that the DIC system's cameras are five-Megapixel cameras. The basis on which the DIC system works entails the pixels from the cameras following a certain speckle while the test is in progress. Therefore, the speckles must be small enough since the test sample's gauge area is also a small object of focus.

Having experimented with different methods of applying a speckle pattern to the test samples, it became evident that for these specific test samples, a very fine speckle pattern was needed. The use of an all-purpose sponge and black acrylic paint which is applied to a flat surface and dabbed with the sponge, delivered the desired speckle pattern. Figure 4.3-1 and Figure 4.3-2 shows the test samples once the speckle pattern has been applied after the test samples was painted matte white.

A summary of the steps followed during the preparation of the test sample follow:

1. **Remove all support material structures from the test samples.** The test samples that were manufactured in the XY-plane had support material that had to be removed carefully to ensure that the test samples are not damaged in the process, as this would impact the test results.

2. **Apply a matte-white spray paint to the test samples.** The test samples are spray painted with a matte-white spray. This is done to reduce reflections on the part as much as possible while the DIC system acquires the data and images. A glossy white paint would reflect too much light off the test sample, which would lead to the DIC system not being able to find start points because the speckle pattern would be lost.

3. **Apply a speckle pattern on the test sample with a sponge.** The most effective way to apply the acrylic paint is to apply the acrylic paint on a flat, clean surface and spread it over an area equal to or bigger than the one side of the sponge. It is recommended that the sponge be rectangular and about the width of the gauge length of the test specimens. The sponge is then dabbed a few times in the wet acrylic paint which has been spread on the flat surface, ensuring to not apply too much pressure as the sponge would then absorb the paint, thus leading to large speckles. The sponge must be placed on the flat surface, with the acrylic paint-covered surface facing the top. The test sample is then held by hand and with the black acrylic paint-covered sponge, the paint is applied gently. The test sample is lifted up again with care not to drag it across the sponge as this will cause smudges on the gauge area.

4. **Repeat process if necessary.** Some test samples might need to be repainted if the speckle pattern is not as desired. The test samples can simply be painted matte white again so that the speckle pattern can be reapplied in another attempt.

Figure 4.3-1: The sponge after it has been dabbed in the acrylic paint

Figure 4.3-2: Test samples once the speckle pattern has been applied

4.4 STANDARD TEST METHOD PROCEDURE

Once the test samples have been prepared, the fatigue testing can begin.

The following procedures are followed: first the procedure is given as stated in the ASTM E606 standard document [38], followed by the procedure carried out during the tests.

4.4.1 TEST ENVIRONMENT

According to section 8.1.1.2 from [38]:

> For the duration of the test, the controlled temperature of the specimen should be T_n±2℃.
>
> NOTE 19 – If the temperature cannot be maintained within limits mentioned above, then temperature deviations should be reported. If possible, the effect of temperature should be demonstrated throughout the range of test temperatures.

According to section 8.1.2 from [38]: “specimens tested at room temperature also should be in draft-free surroundings”.

The tests were carried out in the laboratory where the MTS test bench is located. This is an indoor facility, thus ensuring that the surroundings are draft-free.

Figure 4.4-1: Test setup in laboratory

4.4.2 TEST MACHINE CONTROL

According to section 8.3 from [38]:

> Test Machine Control – It is necessary to control one (or more) variable(s) (for example, stress, strain, force, displacement, or other appropriate parameters) in a manner that is in keeping with the test objectives.

For the fatigue test, the force applied to the test specimens was the controlled variable. The force applied was a percentage of the ultimate tensile strength of the specimen. The following table is an example of the input variables entered into the MTS TestSuite program.

Table 4-3: MTS input variables showing the applied force as a percentage load of the UTS

NAME	VALUE	UNIT
Ultimate Force	24.570	kN
R	0.1	unitless
f	10	Hz
Percentage Load	0.75	unitless

In Table 4-3 the ultimate force is 24,570 kN. The percentage of this ultimate force that is applied to the specimen is 0.75, which translates to 75% of the 24,570 kN. It can also be noted that the test is carried out at a rate of 10 Hz, with R= 0,1 indicating that it is an axial-axial test and not a fully reversed test.

4.4.3 WAVEFORM

According to section 8.4 from [38]:

> Waveform – The strain (or stress) versus time waveform should be identical throughout a test program unless test objectives are to determine waveform effects. In the absence of specific waveform requirements or equipment limitations, a triangular waveform for continuous cyclic tests and trapezoidal waveforms for hold period tests are preferred.

The waveform obtained from the test is identical throughout the test as well as all the test specimens as no hold periods were preferred for the tests.

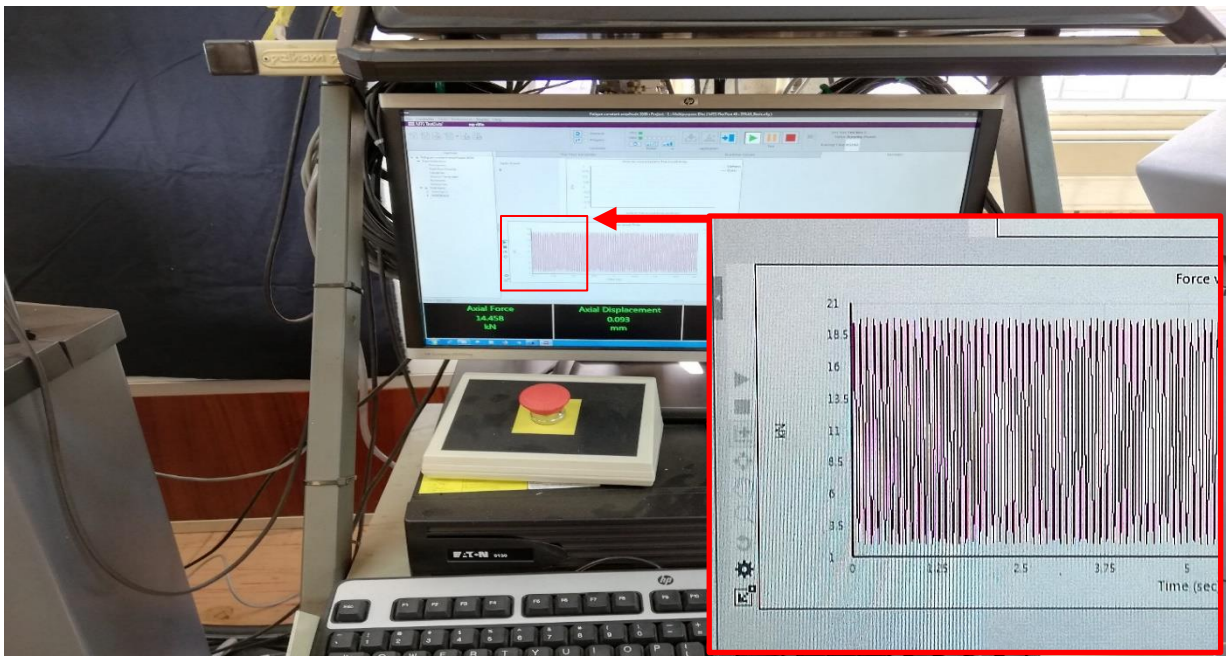

Figure 4.4-2: MTS control computer showing the waveform of the test carried out

4.4.4 STRAIN RATE AND FREQUENCY OF CYCLING

According to section 8.5 from [38]:

> Strain Rate and Frequency of Cycling – Either strain rate or frequency of cycling should be held constant for the duration of each test as well as for the duration of a test program, unless the test objective is specifically to determine either strain rate of frequency effects, respectively.

The frequency was held constant for the duration of the test. The test was carried out with a frequency of 10 Hz for the duration of the test. Refer to Table 4-3.

4.4.5 TEST COMMENCEMENT

According to section 8.6.1 from [38]: “begin all tests in the same direction of initial straining, tensile or compressive, unless the purpose of testing is to study initial loading effects.”

No initial loading (tensile or compressive) was applied before testing commenced, as it was not the purpose of the tests to study initial loading effects.

4.4.6 NUMBER OF SPECIMENS

According to section 8.7 from [38]: “Number of specimens – It is suggested that a minimum of ten specimens be used to generate a fatigue strain-life curve.”

Test specimens that were additively manufactured in two different directions were used in this study. The one set of test specimens was manufactured in the XY-plane (0º in relation to the build direction) and the other test specimens was manufactured in the YZ-plane (90º in relation to the build direction). The tests were carried out on a total of 22 test samples (11 test samples in each of the two build directions).

Figure 4.4-3: Image showing all the test samples that were tested

4.4.7 RECORDING

According to section 8.8 from [38]: “Recording- [...] When practical, continuously record the dependent variables (for example, axial stress and plastic axial strain in a total strain control test) as a function of time.”

Data was collected continuously for the duration of the test through the use of the MTS TestSuite Multipurpose Elite program, which enables the user to export the raw test data and create reports.

4.4.8 DETERMINATION OF FAILURE

The following are the acceptable definitions of failure:

According to section 8.9.1 from [38]:

Separation – Total separation or fracture of the specimen into two parts at (1) some location within the uniform section of a uniform-gage specimen, or (2) the vicinity of the minimum diameter in an hourglass specimen. All failure locations should be recorded.

Likewise, section 8.9.2 from [38] states the following:

Modulus Method – For any specified number of cycles, N, during the test, the modulus for unloading following a peak tensile stress is defined as E_{NT} and the modulus for loading following a peak compression stress is E_{NC}. Failure is defined when the ratio $Q_N = E_{NT}/E_{NC}$ reaches one-half the value of Q for the first cycle $Q_{Nf}=0.5Q1$ [38] (see figure below).

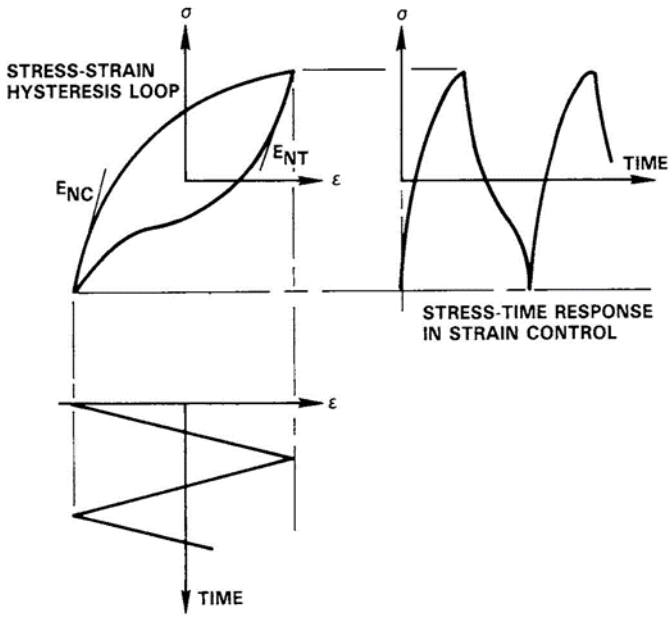

Figure 4.4-4: Definitions of Tension and Compression Modulus for a Determination of Failure [9]

Section 8.9.3 from [38] states: “Microcracking – The existence of surface microcracks (for example, as observed optically or by replicas) that are larger than some preselected size consistent with test objectives”.

Finally, section 8.9.4 from [38] states:

Force (Stress) Drop – It is acceptable to define failure in a manner related to the ability to sustain a tensile force (stress). Failure is often defined as the point at which the maximum force (stress) or elastic modulus (as measured when unloading from a peak tensile stress) decreases by approximately 50% because

of a crack or cracks being present. The exact method and percentage drop should be documented.

The type of failure that occurred in all the test specimens can be categorised as “separation” or the fracture of the test specimens into two pieces within the uniform section of the uniform-gauge specimens. All the specimens broke in the gauge area of the specimen in the uniform section.

4.4.9 TEST DURATION

According to section 8.10 from [38]:

> Test Duration – Conduct testing at least until failure and preferably until fracture when needs dictate and economics allow. Record total accumulated cycles to failure (and fracture) by means of a cycle counter and check against a measure of elapsed time.

The tests were carried out until fracture point was achieved, with the total accumulated cycles and the elapsed time being recorded on the computer with the help of MTS TestSuite Multipurpose Elite software.

4.4.10 DATA ANALYSIS

Section 8.11.1 and 8.11.2 from [38] states the following with regards to the analysis of data:

> Determination of the Cyclic Stress-Strain Curve – Generate a cyclic stress-strain curve from paired values of stress amplitude and strain amplitude typically at material half-life. When practical, assume a simplifying mathematical expression for the cyclic stress-strain relationship.
>
> Determination of Strain-Life Relationship – Generate a strain-life curve from paired values of total strain versus life or plastic strain versus life and elastic strain versus life. When practical, assume a simplifying mathematical relationship.

Section 8.11.3 from [38] states the following with regards to the post-mortem examinations of the test specimens:

> Post-mortem examinations – Metallographic examination of the failed specimens is desirable for a variety of purposes depending in part on user interests. Of foremost importance is a fractographic examination of the two surfaces to determine any unusual causes of failure that might invalidate the test results.

See **Chapter 5** for the data analysis.

CHAPTER 5

RESULTS

This chapter discusses the results obtained from the fatigue tests, the data obtained from the DIC system and the SEM images.

5.1 MATERIAL PROPERTIES

Tensile tests were carried out on test specimens from each of the different orientations. Three specimens were selected at random and tested using the MTS Landmark machine.

5.1.1 0° TEST SPECIMENS

The following table and graph were obtained from the report generated by the MTS Landmark machine.

Table 5-1: Peak loads obtained from 0° tensile test specimens

NAME	PEAK LOAD (KN)
Test run 1	26.305
Test run 2	26.316
Test run 3	26.423
Mean	26.348
Standard deviation	0.065

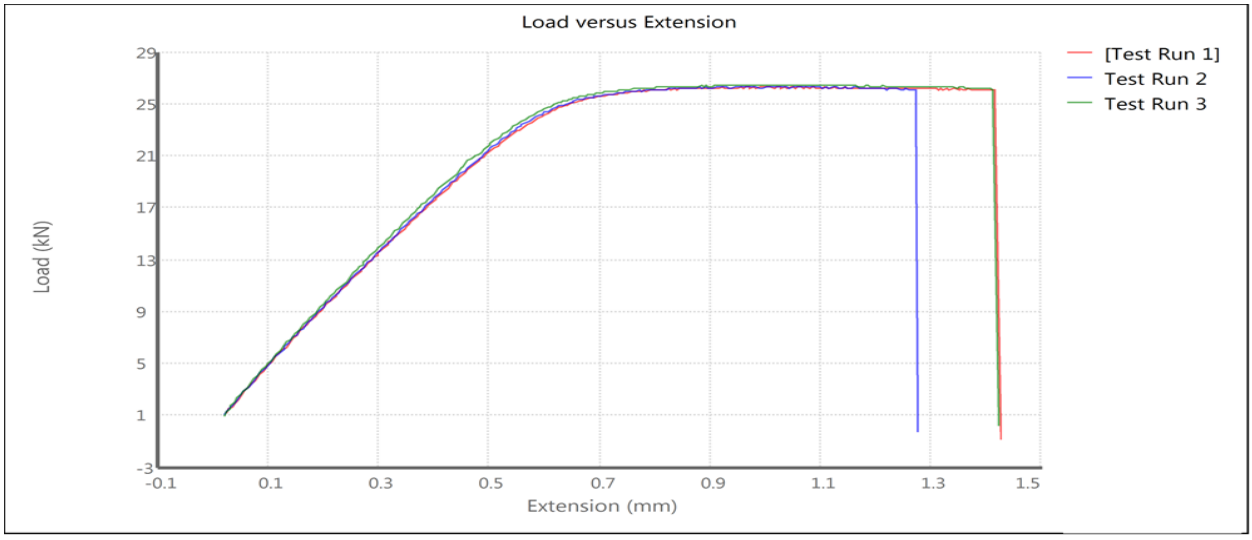

Figure 5.1-1: Load versus Extension graph for 0° tensile test specimens

The results obtained from the tensile tests reveal that all three test samples reacted in a similar fashion in terms of the peak load that they had experienced. It is further noted that the standard deviation from the mean value of 26,348 kN is 0,065 kN. In figure 5.1-1 can be seen that the second test sample (Test run 2) did not extend as much as the other two samples before breaking. The following table gives a summary of the other material properties obtained from the tensile tests.

Table 5-2: Material Properties of 0º tensile test specimens

TEST RUN	MATERIAL PROPERTY	VALUE	UNIT
Test 1	UTS	1092.985	MPa
	Strain	0.022621	mm/mm
	Modulus of elasticity	110.649	GPa
	Yield stress	1074.613	MPa
Test 2	UTS	1093.442	MPa
	Strain	0.020247	mm/mm
	Modulus of elasticity	110.002	GPa
	Yield stress	1078.058	MPa
Test 3	UTS	1097.881	MPa
	Strain	0.022545	mm/mm
	Modulus of elasticity	115.089	GPa
	Yield stress	1079.714	MPa
Average	UTS	1094.769	MPa
	Strain	0.021804	mm/mm
	Modulus of elasticity	111.913	GPa
	Yield stress	1077.462	MPa

The average ultimate tensile stress (UTS) and yield stress obtained from the tensile tests are comparable with values obtained from literature [41] for test samples that have been tested in the as-built condition with only stress-relief done on the parts. The UTS is on the mark of what is expected, 1094,769 MPa compared to the 1096 ±7 MPa from literature. The yield stress, 1077,462 MPa, is within a 6%-range of the values expected from literature, which is 1017±7 MPa (refer to Appendix A for the stress-strain curves of each test run as well as the modulus of elasticity calculation).

5.1.2 90º TEST SPECIMENS

As with the 0º test specimens, the following table and graph were obtained from a report generated from the MTS Landmark machine.

Table 5-3: Peak loads obtained from 90º tensile test specimens

NAME	PEAK LOAD (KN)
Test run 1	24.756
Test run 2	24.420
Test run 3	24.534
Mean	24.570
Standard deviation	0.171

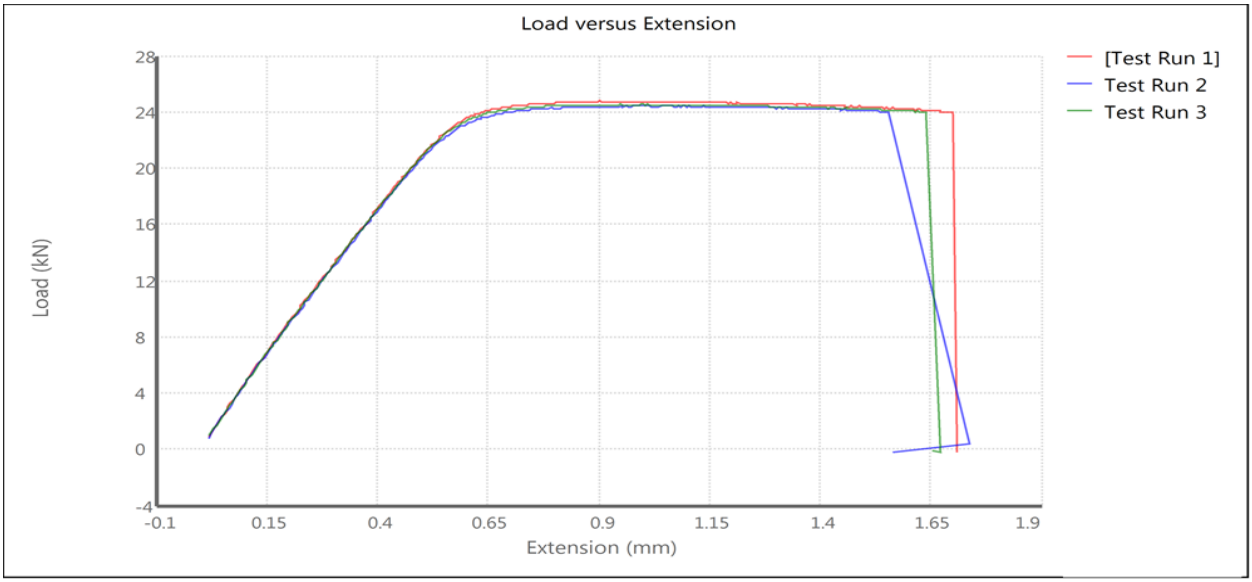

Figure 5.1-2: Load versus extension for 90º tensile test specimens

From Figure 5.1-2 we can see that there is some variance in both the peak loads, that each specimen experienced, as well as the extension of the specimens under the respective loads. The first test specimen endured the highest peak load and extended the furthest of the specimens before breaking. The second test specimen had the lowest peak load and could also not extend as far as the first specimen before breaking.

The third test specimen endured the second-highest peak load and also the second-highest extension under the specified load before breaking. Even though there are some variances with regards to the peak loads experienced by each specimen, it is still within 0,171 kN from the mean

load of 24,570 kN. The following table gives a summary of the material properties that are calculated from the tensile tests.

Table 5-4: Material properties for 90º tensile test specimens

TEST RUN	MATERIAL PROPERTY	VALUE	UNIT
Test 1	UTS	1126.365	MPa
	Strain	0.027286	mm/mm
	Modulus of elasticity	119.572	GPa
	Yield stress	1113.926	MPa
Test 2	UTS	1111.072	MPa
	Strain	0.024854	mm/mm
	Modulus of elasticity	118.3895	GPa
	Yield stress	1094.477	MPa
Test 3	UTS	1116.271	MPa
	Strain	0.026252	mm/mm
	Modulus of elasticity	119.064	GPa
	Yield stress	1102.684	MPa
Average	UTS	1117.903	MPa
	Strain	0.026131	mm/mm
	Modulus of elasticity	119.009	GPa
	Yield stress	1103.696	MPa

The ultimate tensile stress and yield stress from the 90º test specimens are a bit higher than what is expected from literature. The UTS from these specimens are within 2% of what is expected from literature, with the measured UTS at 1117,903 MPa compared to 1096±7 MPa. The yield stress is within 8,5% of what is expected from literature, 1103,696 MPa compared to the 1017±7 MPa from literature.

5.2 FATIGUE RESULTS

The fatigue results that are presented here consists of an S-N curve for each of the different oriented specimens. A discussion regarding the results is also made, but all the hysteresis loops as well as the strain-life graphs are in Appendix B.

5.2.1 0º FATIGUE SPECIMENS

The following table shows each specimen's number as well as the load that it was subjected to. The amount of cycles that each specimen lasted is also tabulated and an S-N graph is also shown,

which has been drawn up from the table. The table is sorted according to the percentage load that each specimen was subjected to and then according to sample number in that load range.

Table 5-5: 0º Test specimens fatigue test results

% UTS	LOAD [KN]	STRESS [KPA]	SAMPLE NUMBER	NUMBER OF CYCLES
75	19.761	821078.96	B5	5191
75	19.761	821078.96	B6	4295
75	19.761	821078.96	B9	4208
65	17.1262	711601.76	B2	4200
65	17.1262	711601.76	B4	7606
65	17.1262	711601.76	B11	8247
45	11.8566	492647.37	B1	22303
45	11.8566	492647.37	B8	15086
45	11.8566	492647.37	B10	15332
35	9.2218	383170.18	B3	47895
35	9.2218	383170.18	B7	32330

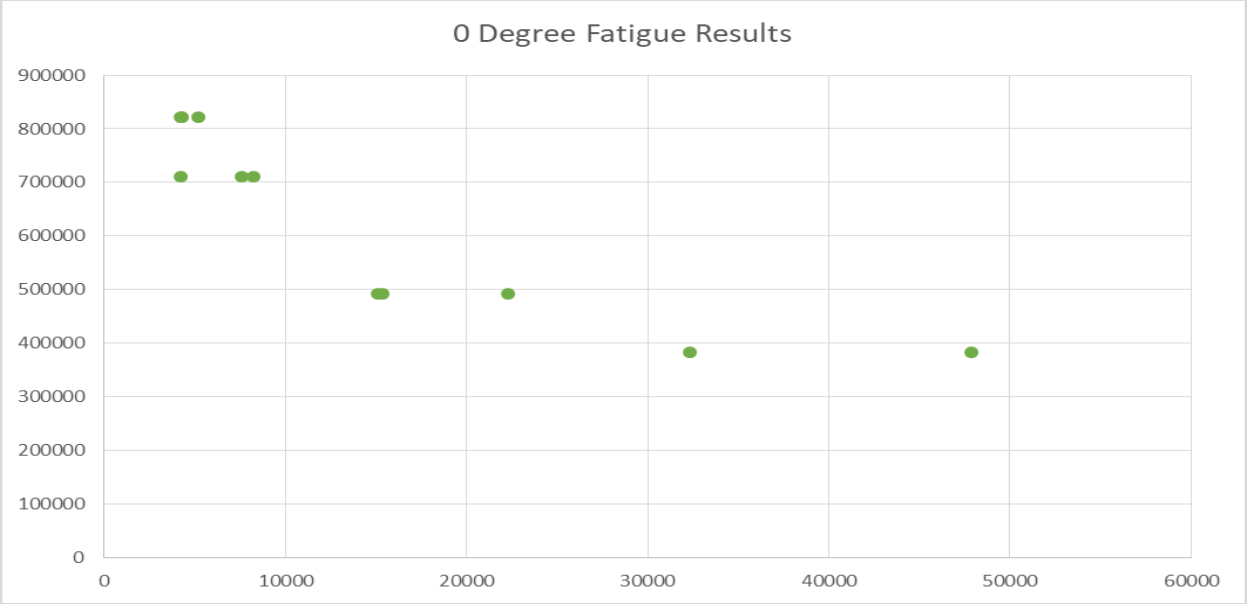

Figure 5.2-1: S-N graph for the 0º test specimen fatigue results

As can be seen from both Table 5-5 and Figure 5.2-1, the grouping in the 75% UTS load range is a good grouping. Two test specimens, B6 and B9, were subjected to a similar amount of cycles before fracturing. Test specimen B5 lasted almost a thousand cycles longer before failing. Below is the SEM image of the fractured surface of specimen B5, which shows a small part of a cavity near the surface (see the upper left corner of the enlarged SEM image). The SEM image of specimen B5 also shows bright spots on the fractured surface. These bright spots are impurities, and they appear bright because they could not conduct the electron beam.

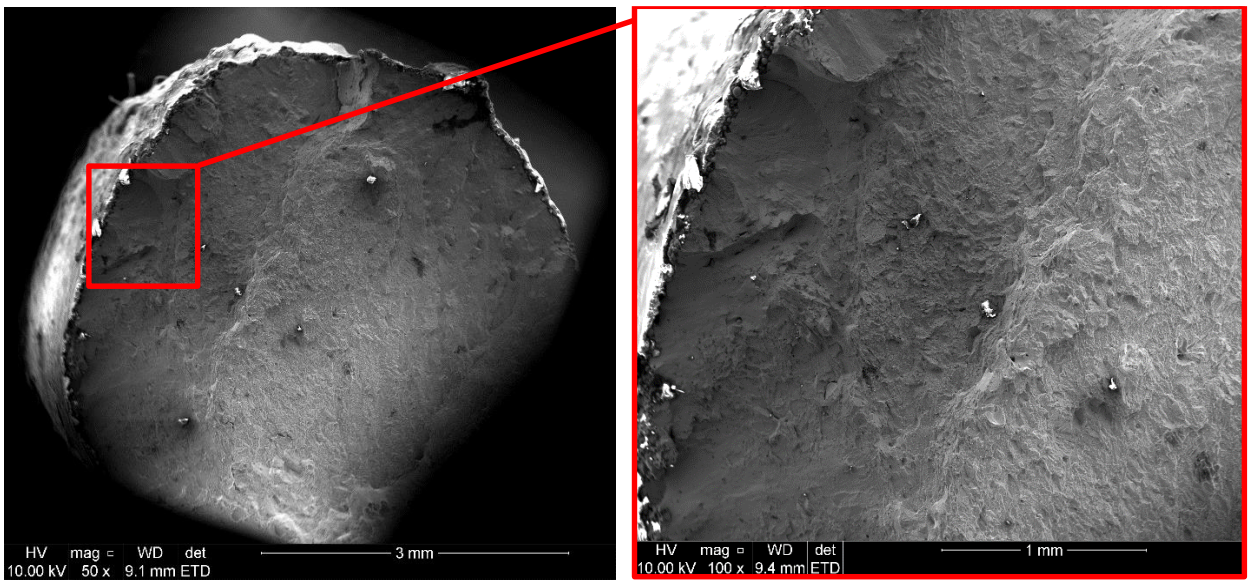

Figure 5.2-2: Specimen B5 SEM images showing a surface defect and impurities on the fractured surface

The 65% UTS range consists of two test specimens that completed a similar number of cycles and one test specimen that failed much earlier than the other test specimens. Below is a figure showing the DIC results from the test specimen that failed earlier than the other specimens. The DIC images did not accurately predict where the specimen would fail. The images are in the following sequence from left to right: reference image, image at half of the fatigue life, image taken right before the specimen fails, and image showing the point of failure.

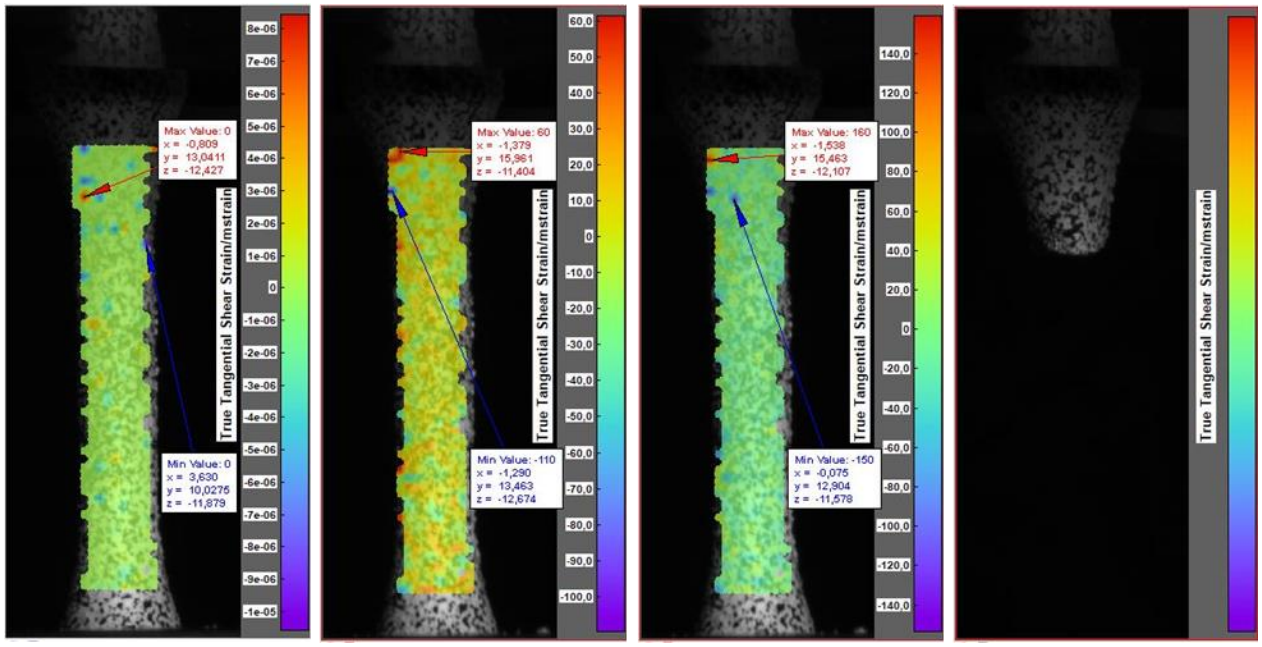

Figure 5.2-3: Specimen B2's DIC images

The 45% UTS load range also consists of two specimens that completed a similar amount of cycles and one specimen that failed much later than the other two specimens. The two figures

included below show the DIC results of specimens B1 and B8. Specimen B1 lasted longer than the two other specimens. The DIC images accurately predicted where the specimen fails, but it can only be seen in the image taken the instant before the specimen failed.

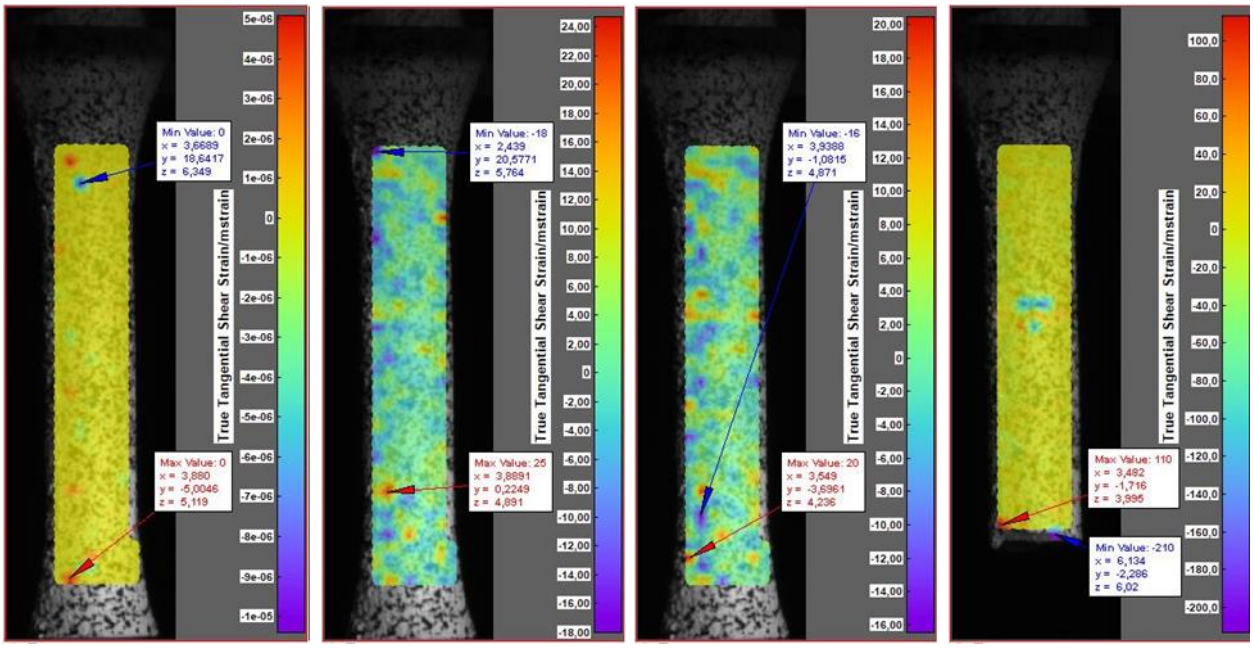

Figure 5.2-4: Specimen B1's DIC results

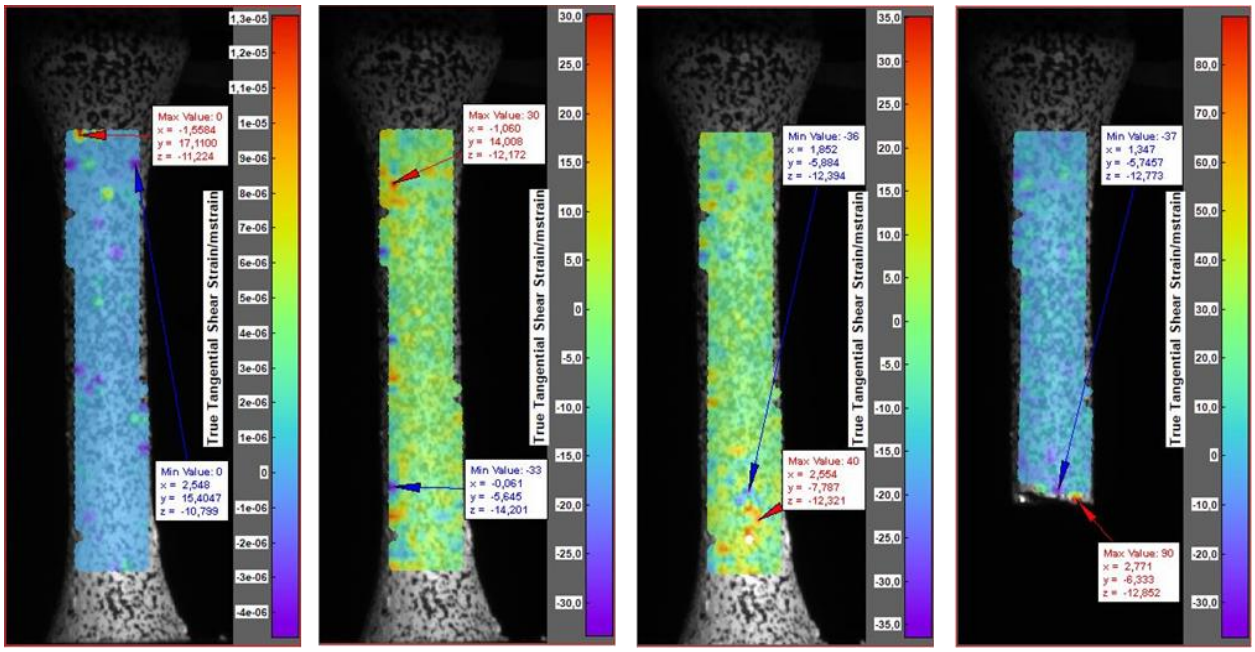

Figure 5.2-5: DIC results for specimen B8

In the 35% UTS load range, there is a noticeable difference between the numbers of cycles that each specimen completed. Specimen B7 failed before specimen B3. The SEM image of specimen B7 is shown below. From the enlargement of the fractured surface, an internal defect can be noticed as well as residual metal powder which did not completely sinter during the manufacturing

process. It can be noted that the metal powder is spherical and have differing diameters. This internal defect, which is approximately 200µm in length, is expected to contribute to the premature failure of specimen B7.

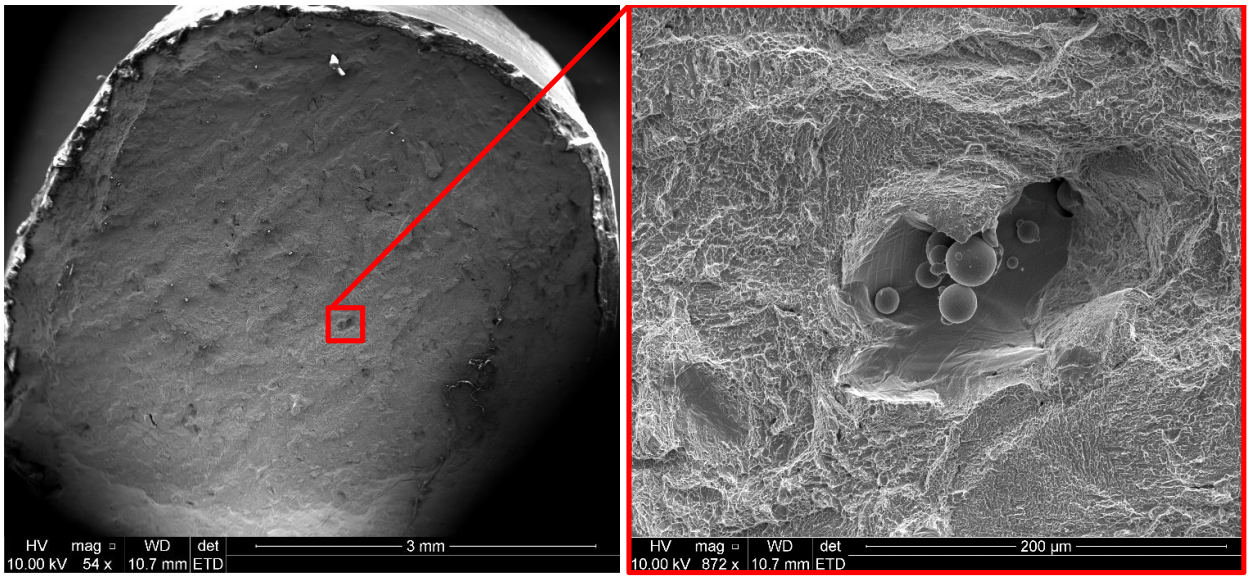

Figure 5.2-6: SEM image for specimen B7 showing an internal defect

5.2.2 90º FATIGUE SPECIMENS

As with the 0º fatigue specimens, the following table and graph were obtained from the fatigue tests that were carried out until failure occurred. This table also shows the load and stress together with the number of cycles associated with each specimen.

Table 5-6: 90º Test specimen fatigue test results

% UTS	LOAD [KN]	STRESS [KPA]	SAMPLE NUMBER	NUMBER OF CYCLES
75	18.4275	838426.88	A3	5182
75	18.4275	838426.88	A5	4808
75	18.4275	838426.88	A8	5041
65	15.9705	726636.63	A4	7701
65	15.9705	726636.63	A7	7734
65	15.9705	726636.63	A10	8268
45	11.0565	503056.13	A1	22201
45	11.0565	503056.13	A2	20403
45	11.0565	503056.13	A9	23848
35	8.5995	391265.88	A6	57009
35	8.5995	391265.88	A11	50387

From Table 5-6 and Figure 5.2-7 it is clear that the grouping is ideal and the test specimens exhibited similar behaviour in the 75% UTS load range. Figure 5.2-8 below is the SEM results of test specimen A8. A large surface defect is noticeable in the image. Surface defects have a negative effect on the fatigue life of a specimen as it promotes the propagation of the crack.

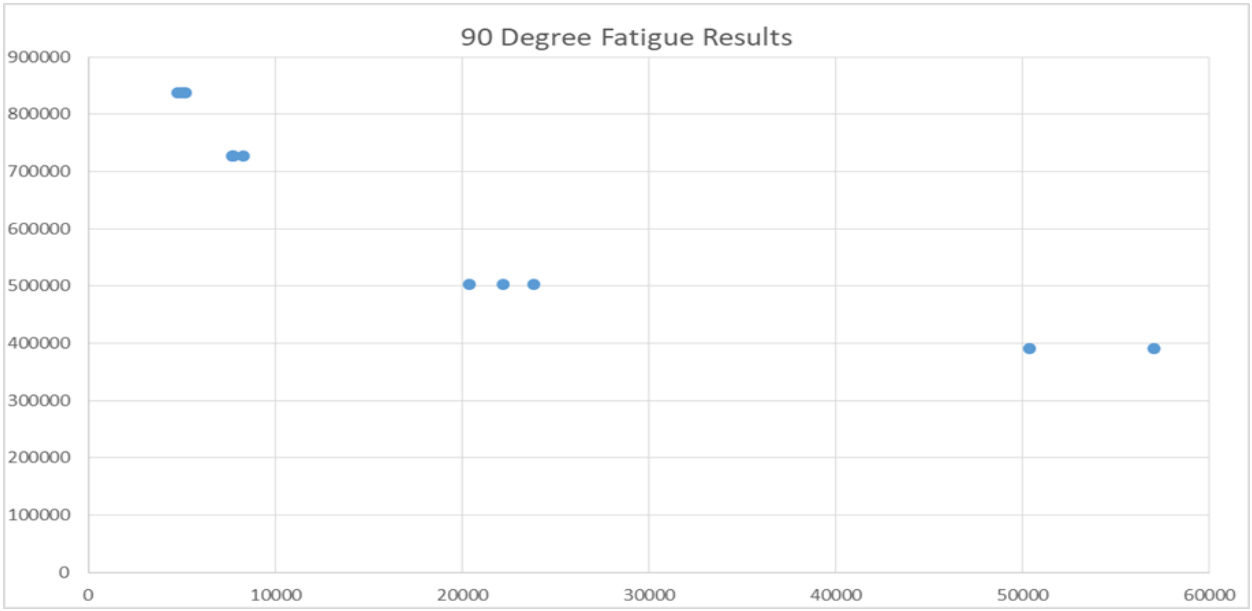

Figure 5.2-7: S-N graph for the 90º test specimen fatigue tests

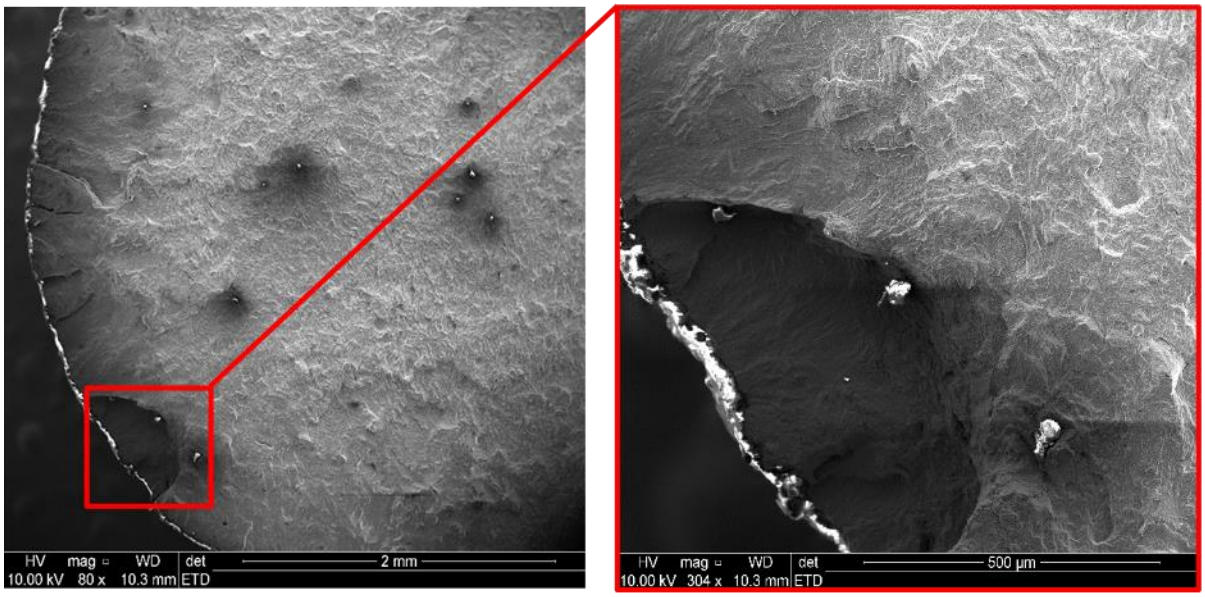

Figure 5.2-8: SEM image for specimen A8

The specimens grouped in the 65% UTS load range are also quite close with the exception of one test specimen that lasted a few hundred cycles longer than the other two specimens. Specimen A7 was subjected to this load case when testing was done and the DIC results of the test are shown below in Figure 5.2-9. The DIC results of specimen A7 show that the DIC was able to accurately predict where the test specimen would fail in the final image taken before failure.

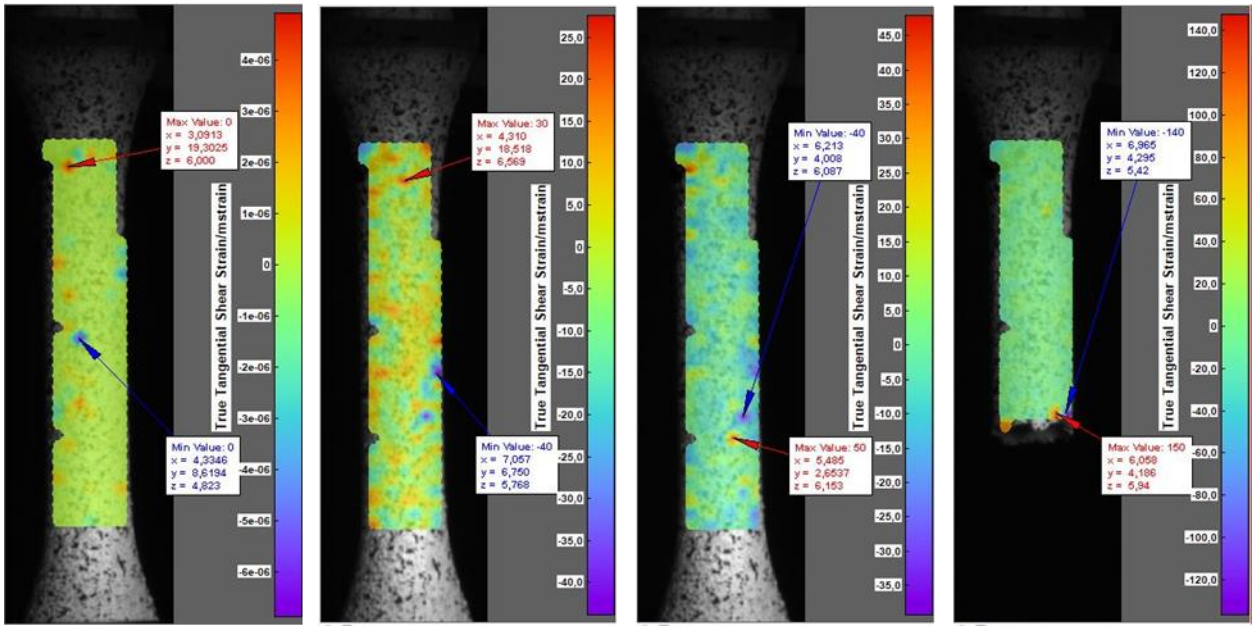

Figure 5.2-9: DIC results for specimen A7

The three test specimens in the 45% UTS load range have differing values for the amount of cycles that it endured before failure. All three specimens fall within the same region of fatigue life (20 000 – 25 000 cycles), with the difference between the sample that lasted longest and the one

that failed first being 3445 cycles. Specimen A2, which was subjected to the 45% UTS load, contained a large surface defect. Figure 5.2-10 shows the location and size of the defect. As with specimen A8, this surface defect would be a major contributor in the cause of failure of the test specimen.

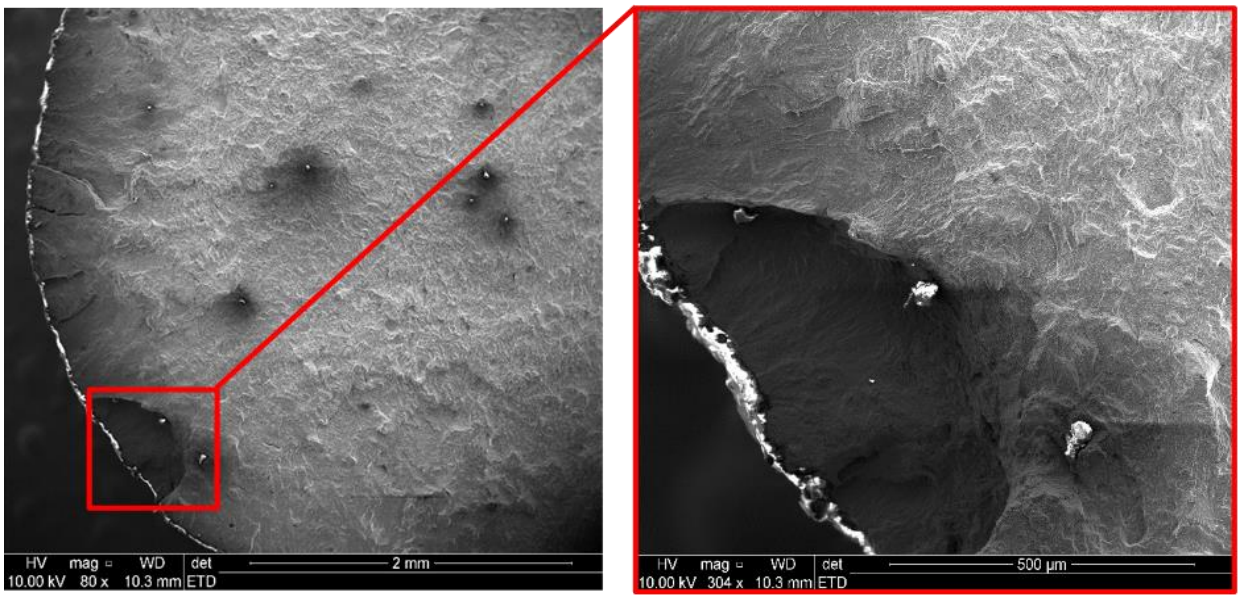

Figure 5.2-10: SEM image of specimen A2

The test specimens that were subjected to 35% of the UTS load all lasted more than 50 000 cycles with one specimen outlasting the other. Figure 5.2-11 below is the DIC results of test specimen A6 and the image confirms that the DIC system was able to accurately predict where the test specimen would fail. This prediction was accurate for both the images of the halfway mark of the fatigue test and image taken the instant before failure occurred. This result is important as it demonstrates that the DIC can accurately predict where a test specimen will fail. However, the DIC is too inconsistent to predict where a part will fail.

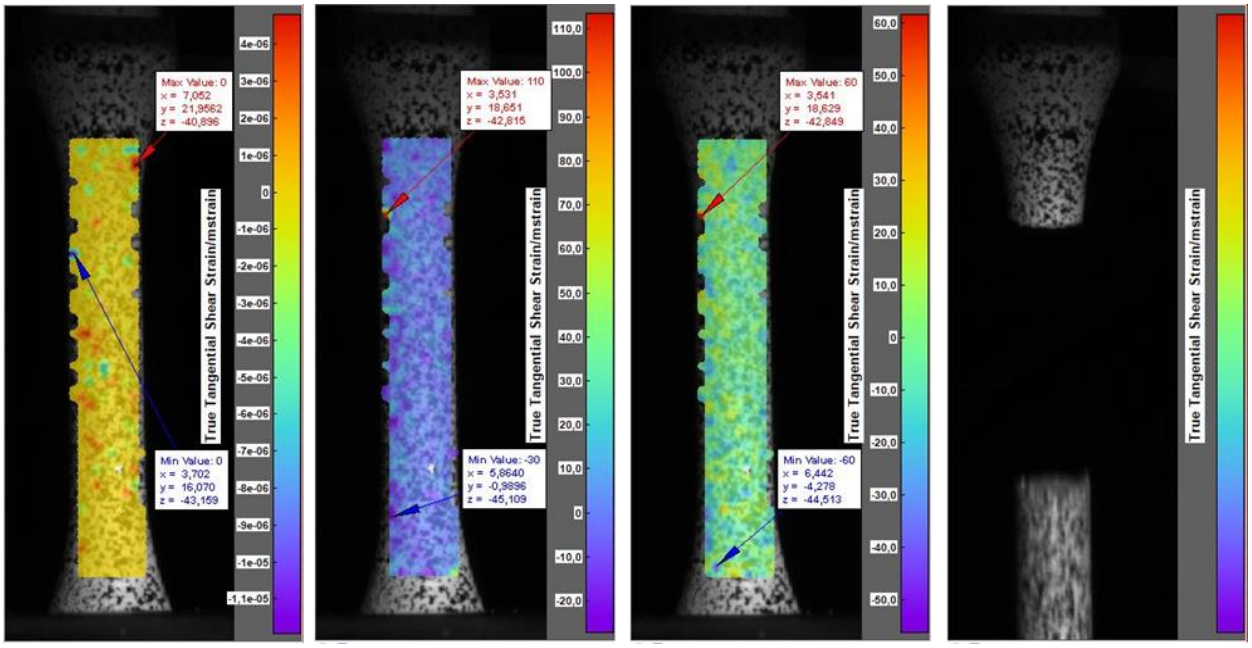

Figure 5.2-11: DIC results for test specimen A6

Figure 5.2-12 is the DIC results for test specimen A11. Specimen A11 was also subjected to the 35% UTS load. For this specimen the results obtained are completely opposite to those of specimen A6. The DIC images for specimen A11 could at no point accurately predict where the specimen would fail. This reaffirms the statement that the DIC system is too inconsistent to predict the point of failure for specimens subjected to fatigue loading.

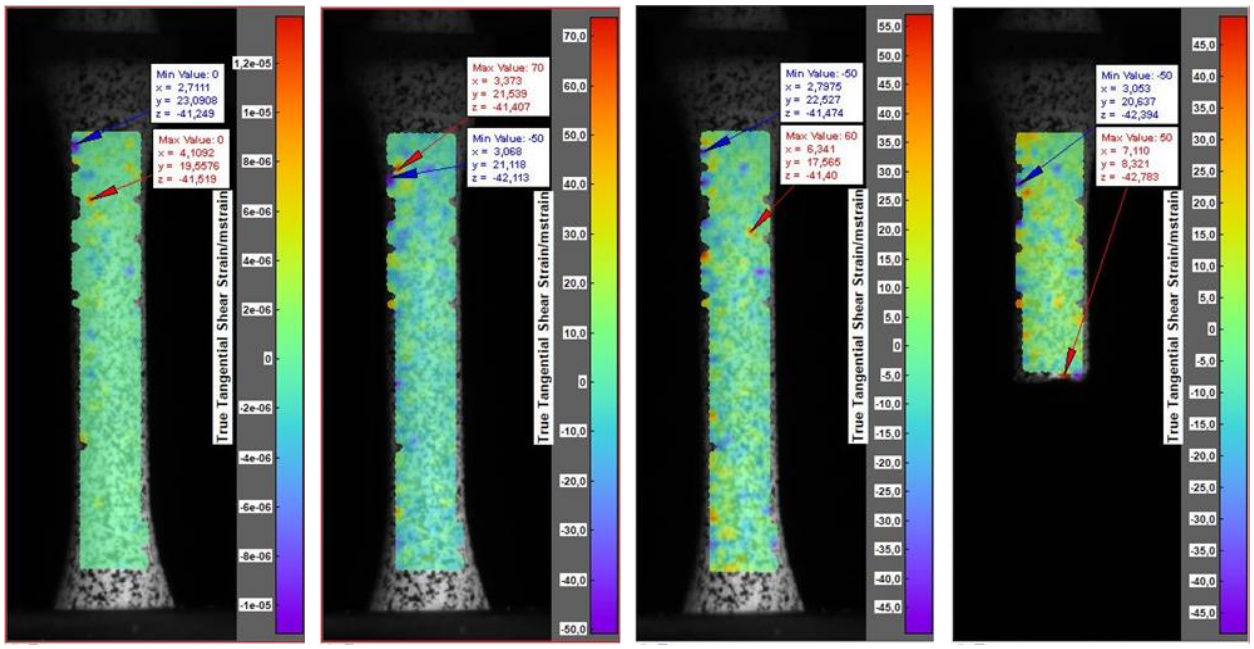

Figure 5.2-12: DIC results for specimen A11

5.2.3 FATIGUE TESTS CONCLUSION

As can be seen from both Table 5-5 and Table 5-6, the fatigue tests were completed at a wide range of loads. This is done so that the endurance limit of the material can be determined. Traditionally the endurance limit of most metals are reached at 50% UTS load. As can be seen from the results in the abovementioned tables, the fatigue endurance limit was not achieved at a load that is far less than 50% of the UTS. This is observed in both orientations of the specimens that were used. It is expected that the fatigue results would not be at an optimum as the specimens were tested in the as-built condition, which in essence is the least favourable condition for fatigue testing.

5.3 DIC RESULTS DISCUSSION

The DIC images are included in Appendix B with each fatigue test specimen. A discussion of the results as can be seen from these images is covered here.

As the fatigue tests were being carried out, the DIC system was simultaneously being used to acquire images of the tests. A trigger was activated once the MTS reached a certain load on the rising slope of the stress-life cycle's first cycle. Every 50th cycle was captured to prevent an overload of images from being stored on the computer. The images were evaluated using ISTRA 4D software and the true shear strain was visualised in the images obtained. The maximum and minimum values for the shear strain are also included in the images. Three images of each specimen are included in the appendix: an image at the beginning of the test, at half of the fatigue life, the instant before failure. In some cases, images are included after the specimen has failed. The following three tables gives a summary of the prediction success of the DIC system.

5.3.1 SUMMARY OF DIC SYSTEM'S PREDICTION ABILITY

Two tables are drawn up to summarise the results of the DIC system's ability to predict the failure point of each specimen through the use of visualising the shear strain concentration on images taken of the specimen during testing. The ***RED*** cell containing the word ***NEGATIVE*** indicates that the visualisation was not in the same place as the point of failure, whilst a ***GREEN*** cell containing the word ***POSITIVE*** indicates that the shear strain concentration was visualised at the correct point of failure.

Table 5-7: Summary of 0º fatigue tests' DIC results

SPECIMEN NAME/NUMBER	SHEAR STRAIN CONCENTRATION VISUALISED AT FAILURE POINT	
	50% OF FATIGUE LIFE IMAGE	FINAL IMAGE TAKEN
B1	NEGATIVE	POSITIVE
B2	NEGATIVE	NEGATIVE
B3	NEGATIVE	NEGATIVE
B4	NEGATIVE	NEGATIVE
B5	NEGATIVE	NEGATIVE
B6	NEGATIVE	NEGATIVE
B7	NEGATIVE	NEGATIVE
B8	NEGATIVE	POSITIVE
B9	NO DATA	NO DATA
B10	NEGATIVE	NEGATIVE
B11	NEGATIVE	NEGATIVE
TOTAL	0/10	2/10
PERCENTAGE	0%	20%

Only 20% of the 0º test specimens' failure point was visible at the same point at which the test specimen had failed, and it could only be seen in the image taken of the test specimen the moment before it failed.

Table 5-8: Summary of 90º fatigue tests' DIC results

SPECIMEN NAME/NUMBER	SHEAR STRAIN CONCENTRATION VISUALISED AT FAILURE POINT	
	50% OF FATIGUE LIFE IMAGE	FINAL IMAGE TAKEN
A1	NEGATIVE	NEGATIVE
A2	NEGATIVE	NEGATIVE
A3	NEGATIVE	NEGATIVE
A4	NEGATIVE	NEGATIVE
A5	NEGATIVE	NEGATIVE
A6	POSITIVE	POSITIVE
A7	NEGATIVE	POSITIVE
A8	NO DATA	NO DATA
A9	NEGATIVE	NEGATIVE
A10	POSITIVE	POSITIVE
A11	NEGATIVE	NEGATIVE
TOTAL	2/10	3/10
PERCENTAGE	20%	30%

Only 30% of the DIC images taken of the specimens right before failure, showed the maximum shear strain in the same place as the point of failure. Twenty percent (20%) of the images taken

at 50% of the fatigue life of the specimens were correct in visualising the shear strain in the same place as the point of failure.

Of the entire population of test specimens that were used, only 10% of the DIC images showed the maximum shear strain to be in the same spot as the failure point of the specimens. For the images taken the moment before failure, the DIC correctly showed the maximum shear strain to be at the same spot as the failure point in 25% of the specimens.

5.4 SEM RESULTS DISCUSSION

The SEM images of specimens that were evaluated are included at each specimen in Appendix B.

The results from the SEM imaging showed some interesting defects that were present in the test samples. A few of the test samples that were SEMed had significant surface defects and this would arguably have been the cause of failure for most of the specimens. Internal defects can also be seen in the SEM images as well as the Ti-6Al-4V powder that was not sintered during the manufacturing process.

CHAPTER 6

CONCLUSION AND RECOMMENDATIONS

The purpose of the study was to determine whether or not a DIC system could be used to determine the fatigue life of Ti-6Al-4V tensile test specimens. Discovering this entailed completing the fatigue test until failure occurred. The evaluated images that were obtained from the DIC system would be used to scrutinise the fracture point and identify at what percentage of the fatigue life the strain first appeared in the same area where the failure occurred. A few conclusions were made from this study:

1. The Ti-6Al-4V test specimens reacted very brittle during testing, as was expected for the as-built condition in the sense that it failed catastrophically. The test specimens never underwent any significant strain in the form of necking before failing. The accuracy of the DIC system was tested with this in mind to determine whether it could accurately identify the strain concentration in the specimens. It was difficult to identify a strain concentration in the area where the part had failed, at any given time of the fatigue test given that the specimens failed catastrophically. In some cases the strain concentration was captured in the same place as the point of failure, but this rarely happened.
2. The surface defects that were present in the parts, as can be seen in Appendix B from the SEM images, are considered to be the main cause of failure in most of the specimens. The literature is relatively clear on the argument that surface defects have the highest impact on the fatigue life of as-built test specimens, as can be seen in the conclusions of [19].
3. The DIC system is not yet a viable testing system to replace other non-destructive testing methods such as micro-CT scanning for Ti-6Al-4V test specimens that have been additively manufactured and tested in the as-built condition.
4. The hypothesis that the DIC system will predict where all the specimens fail cannot be accepted as this was only true for some of the specimens.

Recommendations for the study would be to use different combinations of post-processing on the Ti-6Al-4V test specimens. The post-processing methods that can be applied to the test specimens include heat treatment of the specimens, shot peening and polishing. Combinations of these post-processing methods can also be done on the test specimens. From literature it can be seen that the post processing of Ti-6Al-4V increases the fatigue life of the test specimens. This might allow the test specimen to elongate slightly more and show clearer strain concentrations in the gauge area, thus allowing the DIC system to accurately predict where the specimen might fail.

Recommendations for the improvement of the DIC system would include adding more cameras to the system as this is possible with the system. Observing the test specimen from more angles will give a clearer picture of where strain concentrations form. Using cameras with a higher pixel count will also improve results as better images will be captured even when the cameras are zoomed in.

REFERENCES

[1] S. A.M. Tofail *et al.,* “Additive manufacturing: scientific and technological challenges, market uptake and opportunities,” *Materials Today*, vol. 21, no. 1, pp. 22–37, 2018.

[2] A. Bača, R. Konečná, G. Nicoletto, and L. Kunz, “Influence of Build Direction on the Fatigue Behaviour of Ti6Al4V Alloy Produced by Direct Metal Laser Sintering,” *Materials Today: Proceedings*, vol. 3, no. 4, pp. 921–924, 2016.

[3] A. Bača, R. Konečná, and G. Nicoletto, “Influence of the Direct Metal Laser Sintering Process on the Fatigue Behavior of the Ti6Al4V Alloy,” *MSF*, vol. 891, pp. 317–321, 2017.

[4] M. Benedetti *et al.,* “The effect of post-sintering treatments on the fatigue and biological behavior of Ti-6Al-4V ELI parts made by selective laser melting,” (eng), *Journal of the mechanical behavior of biomedical materials*, vol. 71, pp. 295–306, 2017.

[5] *EOS Industrial 3D printing - Process, method and benefits.* [Online] Available: https://www.eos.info/additive_manufacturing/for_technology_interested. Accessed on: Jan. 18 2019.

[6] B. Redwood, F. Schöffer, and B. Garret, *The 3D Printing Handbook: Technologies, design and applications,* 1st ed. Amsterdam, The Netherlands: 3D Hubs, 2017.

[7] Loughborough University, *Directed Energy Deposition*.

[8] AMFG, *Metal 3D Printing: What is Direct Energy Deposition?* [Online] Available: https://amfg.ai/2018/09/27/metal-3d-printing-what-is-direct-energy-deposition/. Accessed on: Apr. 04 2019.

[9] Loughborough University, *About Additive Manufacturing: Sheet Lamination.* [Online] Available: https://www.lboro.ac.uk/research/amrg/about/the7categoriesofadditivemanufacturing/sheetlamination/. Accessed on: Apr. 04 2019.

[10] NIRAJ, “Microsoft PowerPoint - Additive_Manufacturing.pptx,”

[11] I. Gibson, D. Rosen, and B. Stucker, *Additive Manufacturing Technologies*. New York, NY: Springer New York, 2015.

[12] V. Bhavar, P. Kattire, and S. Khot, Eds., *A review on powder bed fusion technology of metal additive manufacturing*, 2014.

[13] T. M. Mower and M. J. Long, “Mechanical behavior of additive manufactured, powder-bed laser-fused materials,” *Materials Science and Engineering: A*, vol. 651, pp. 198–213, 2016.

[14] H. Ali, Le Ma, H. Ghadbeigi, and K. Mumtaz, “In-situ residual stress reduction, martensitic decomposition and mechanical properties enhancement through high temperature powder bed pre-heating of Selective Laser Melted Ti6Al4V,” *Materials Science and Engineering: A*, vol. 695, pp. 211–220, 2017.

[15] L. E. Murr *et al.,* “Metal Fabrication by Additive Manufacturing Using Laser and Electron Beam Melting Technologies,” *Journal of Materials Science & Technology*, vol. 28, no. 1, pp. 1–14, 2012.

[16] Ian D. Harris, Ed., *New Developments in Welding and Metal Additive Manufacturing Using Directed Energy Deposition*, 2015.

[17] X. Li, C. Wang, W. Zhang, and Y. Li, “Fabrication and characterization of porous Ti6Al4V parts for biomedical applications using electron beam melting process,” *Materials Letters*, vol. 63, no. 3-4, pp. 403–405, 2009.

[18] S. L. Sing, J. An, W. Y. Yeong, and F. E. Wiria, “Laser and electron-beam powder-bed additive manufacturing of metallic implants: A review on processes, materials and designs,” (eng), *Journal of orthopaedic research : official publication of the Orthopaedic Research Society*, vol. 34, no. 3, pp. 369–385, 2016.

[19] M. Benedetti, M. Cazzolli, V. Fontanari, and M. Leoni, “Fatigue limit of Ti6Al4V alloy produced by Selective Laser Sintering,” *Procedia Structural Integrity*, vol. 2, pp. 3158–3167, 2016.

[20] A. Hemmasian Ettefagh, C. Zeng, S. Guo, and J. Raush, “Corrosion behavior of additively manufactured Ti-6Al-4V parts and the effect of post annealing,” *Additive Manufacturing*, vol. 28, pp. 252–258, 2019.

[21] “Introduction to Steel: Metallurgical Characteristics and Properties,”

[22] R.C. Hibbeler, *Mechanics of Materials*. New Jersey, USA: Pearson Prentice Hall, 2005.

[23] H.E. Boyer, “Fatigue Testing,” *Atlas of Fatigue Curves*, 1986.

[24] A. Du Plessis, I. Yadroitsev, I. Yadroitsava, and S. G. Le Roux, “X-Ray Microcomputed Tomography in Additive Manufacturing: A Review of the Current Technology and Applications,” *3D Printing and Additive Manufacturing*, vol. 5, no. 3, pp. 227–247, 2018.

[25] A. Du Plessis and S. G. Le Roux, “Standardized X-ray tomography testing of additively manufactured parts: A round robin test,” *Additive Manufacturing*, vol. 24, pp. 125–136, 2018.

[26] Dantec Dynamics, *DIC Applications.* [Online] Available: https://www.dantecdynamics.com/dic-applications. Accessed on: May 27 2019.

[27] C. Herbst and K. Splitthof, “Basics of 3D Digital Image Correlation,”

[28] J. Gordon, J. Hochhalter, C. Haden, and D. G. Harlow, “Enhancement in fatigue performance of metastable austenitic stainless steel through directed energy deposition additive manufacturing,” *Materials & Design*, vol. 168, p. 107630, 2019.

[29] C. Içöz, L. Patriarca, M. Filippini, and S. Beretta, “Strain Accumulation in TiAl Intermetallics via High-resolution Digital Image Correlation (DIC),” *Procedia Engineering*, vol. 74, pp. 443–448, 2014.

[30] K. Akhtar, S. A. Khan, S. B. Khan, and A. M. Asiri, “Scanning Electron Microscopy: Principle and Applications in Nanomaterials Characterization,” in *Handbook of Materials Characterization*, S. K. Sharma, Ed., Cham: Springer International Publishing, 2018, pp. 113–145.

[31] Weilie Zhou, Robert P. Apkarian, Zhong Lin Wang, and David Joy, “Fundamentals of Scanning Electron Microscopy (SEM),”

[32] O. P. Choudhary and P. ka, “Scanning Electron Microscope: Advantages and Disadvantages in Imaging Components,” *Int.J.Curr.Microbiol.App.Sci*, vol. 6, no. 5, pp. 1877–1882, 2017.

[33] E. Charkaluk and V. Chastand, “Fatigue of Additive Manufacturing Specimens: A Comparison with Casting Processes,” *Proceedings*, vol. 2, no. 8, p. 474, 2018.

[34] S.-M.-J. Razavi, P. Ferro, and F. Berto, “Fatigue Assessment of Ti–6Al–4V Circular Notched Specimens Produced by Selective Laser Melting,” *Metals*, vol. 7, no. 8, p. 291, 2017.

[35] Richard Gedney, *Stress-Life Fatigue Testing Basics.* [Online] Available: https://www.qualitymag.com/articles/94171-stress-life-fatigue-testing-basics. Accessed on: Sep. 03 2019.

[36] Richard G. Budynas and J. Keith Nisbett, *Shingley's Mechanical Engineering Design*. New York, NY: McGraw-Hill Education, 2015.

[37] DESKTOP-9H3KIS4\CP Kloppers (DESKTOP-9H3KIS4), “ASTM E606 Specimen,”

[38] *Test Method for Strain-Controlled Fatigue Testing*.

[39] “EOS_M280_Metal-Machine,”

[40] “MTS LANDMARK 370.10,”

[41] S. Beretta and S. Romano, “A comparison of fatigue strength sensitivity to defects for materials manufactured by AM or traditional processes,” *International Journal of Fatigue*, vol. 94, pp. 178–191, 2017.

[42] Daniella Da Costa, *Investigating the Fatigue Behaviour of Raw Ti-6Al-4V*.

[43] Geo Joubert, *Investigation and balidation of the effects of a notch on the fatigue life of stainless steel 316*.

APPENDIX A

TENSILE TEST RESULTS

This section of the appendix contains the stress-strain curves obtained from the tensile tests that were performed to determine the material properties.

A.1 0º TESTS

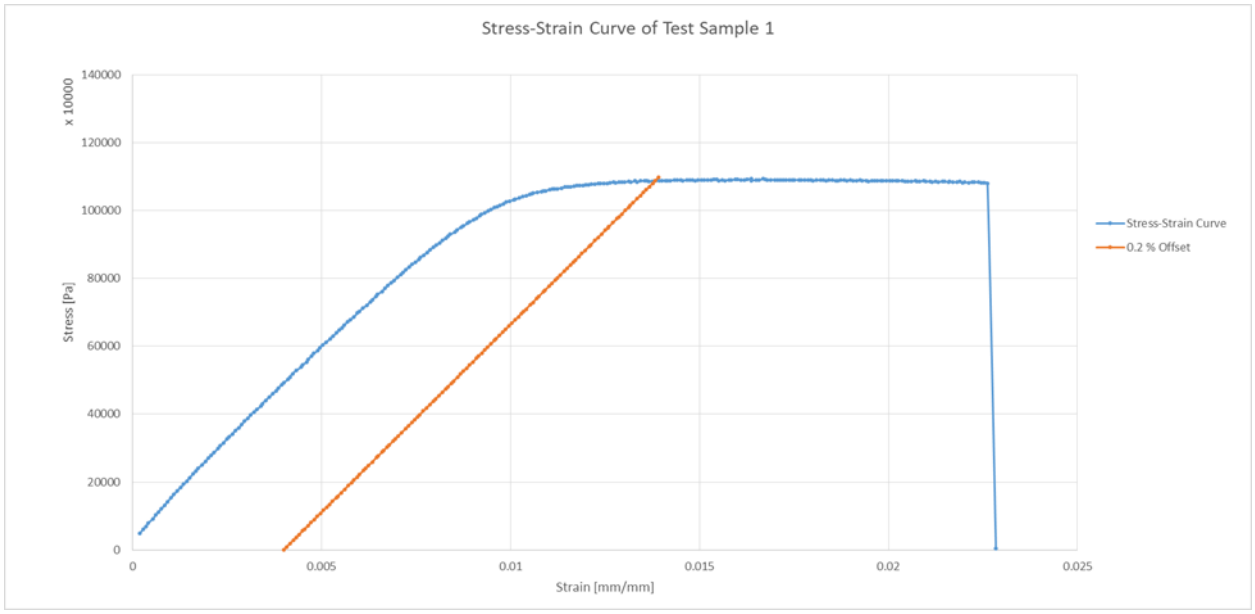

Figure A.1-1: Stress-Strain Curve for 0º tensile test specimen 1

From the figure above it is clear that the maximum stress (UTS) is just above 1000 MPa, the yield stress is the measured where the 0.02% offset line intersects the stress-strain curve. We also note that maximum strain is measured between 0.02 mm/mm and 0.025 mm/mm.

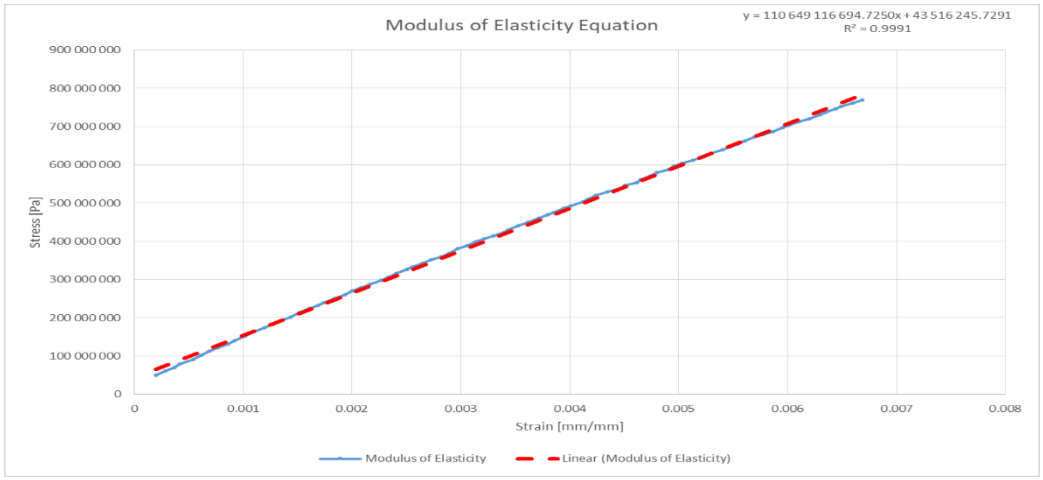

Figure A.1-2: Modulus of elasticity for 0º tensile test specimen 1

The modulus of elasticity is obtained from plotting the elastic region of the stress-strain curve where stress and strain are directly equivalent. The gradient of the line is the modulus of elasticity and from that we see that the modulus of elasticity is 110 GPa.

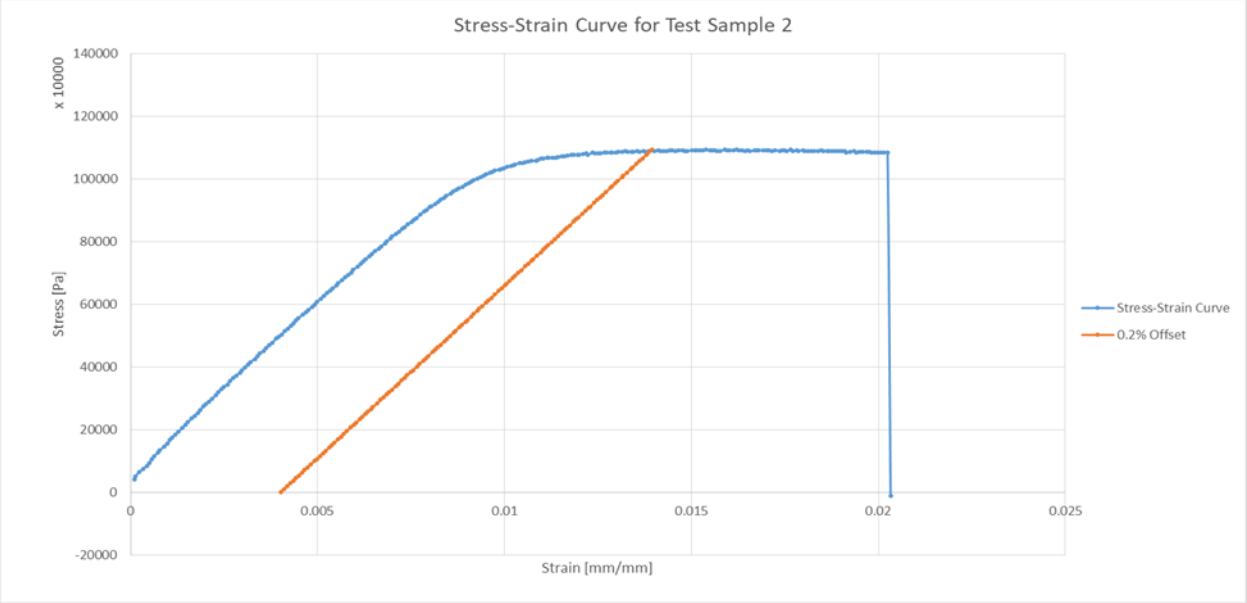

Figure A.1-3: Stress-Strain Curve for test sample 2

From the figure above it is clear that the maximum stress (UTS) is just above 1000 MPa and close to 1100 MPa, the yield stress is the measured where the 0.02% offset line intersects the stress-strain curve. We also note that maximum strain is measured at just above 0.02 mm/mm.

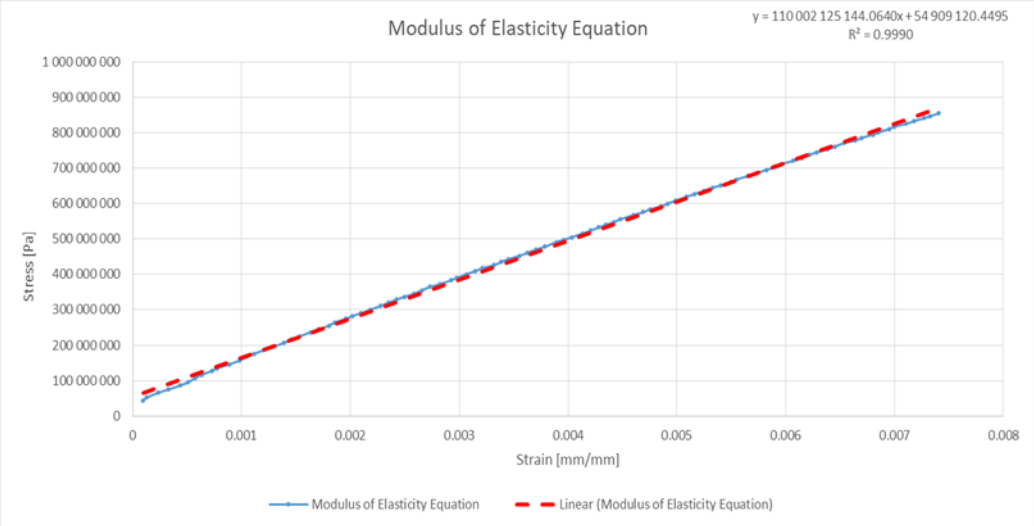

Figure A.1-4: Modulus of Elasticity for tensile test specimen 2

As with the first test specimen the elastic region of the stress-strain curve is plotted with a linear trend line plotted over it to obtain the gradient for the modulus of elasticity, which is 110 GPa.

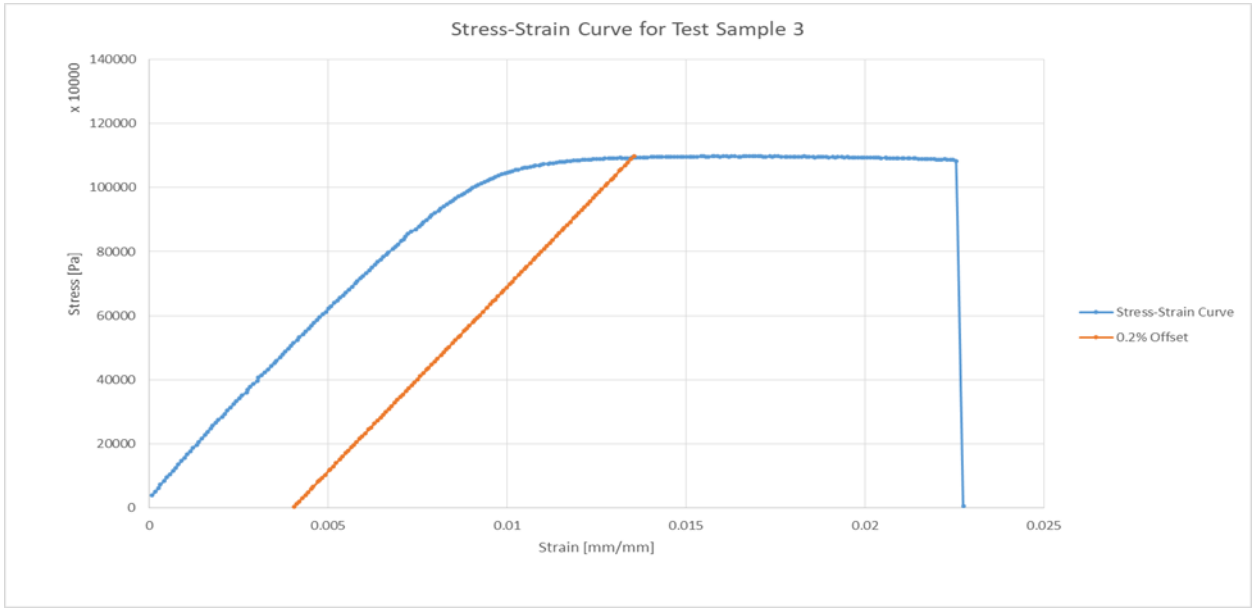

Figure A.1-5: Stress-Strain Curve for test sample 3

From Figure A.1-5 it is clear that the maximum stress (UTS) is in the stress region of 1100 MPa, the yield stress is measured where the 0.02% offset line intersects the stress-strain curve, also in the region of the UTS. We also note that maximum strain is measured at around 0.0225 mm/mm.

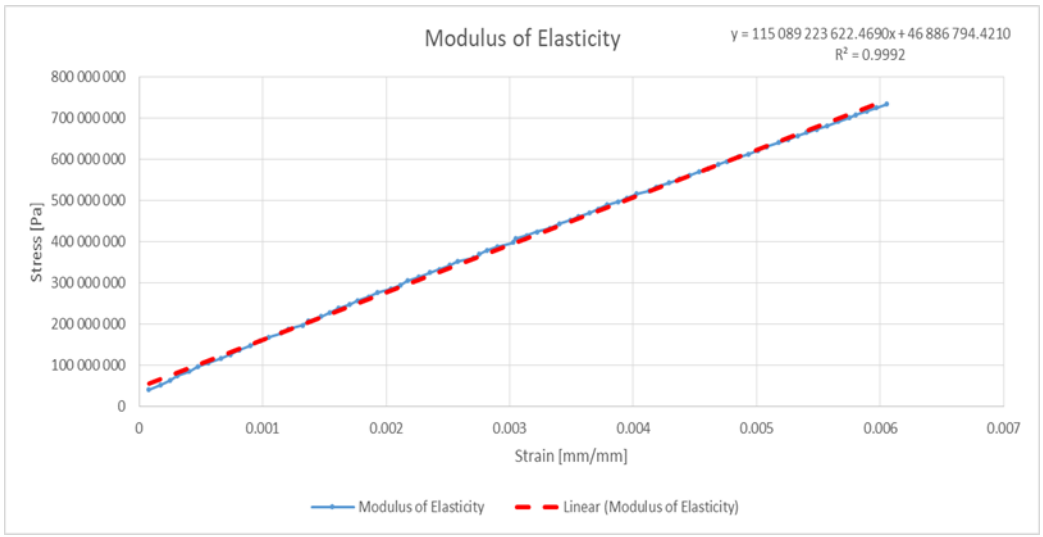

Figure A.1-6: Modulus of Elasticity of 0º tensile test specimen 3

The equation obtained from plotting the elastic region of the stress-strain curve indicates that tensile test specimen 3 from the 0º orientation has a modulus of elasticity of 115 GPa.

A.2 90º TESTS

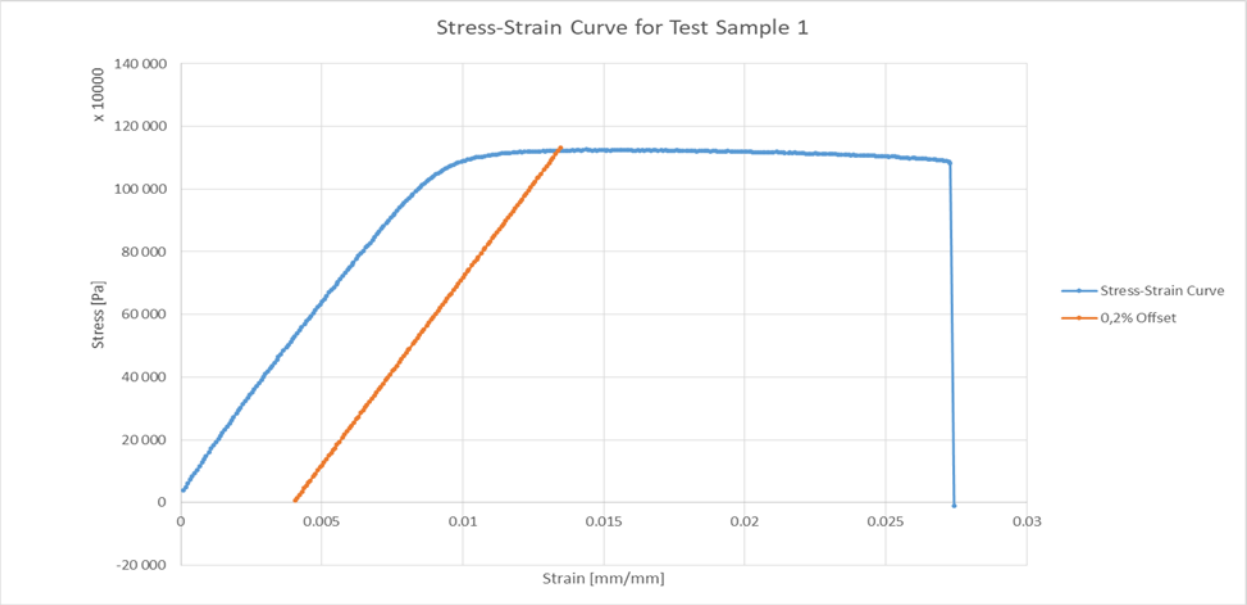

Figure A.2-1: Stress-Strain Curve for 90º tensile test specimen 1

From Figure A.2-1 it is clear that the maximum stress (UTS) is in the stress region of just above 1100 MPa, the yield stress is the measured where the 0.02% offset line intersects the stress-strain curve, also in the region of the UTS. We also note that maximum strain is measured at around 0.0275 mm/mm.

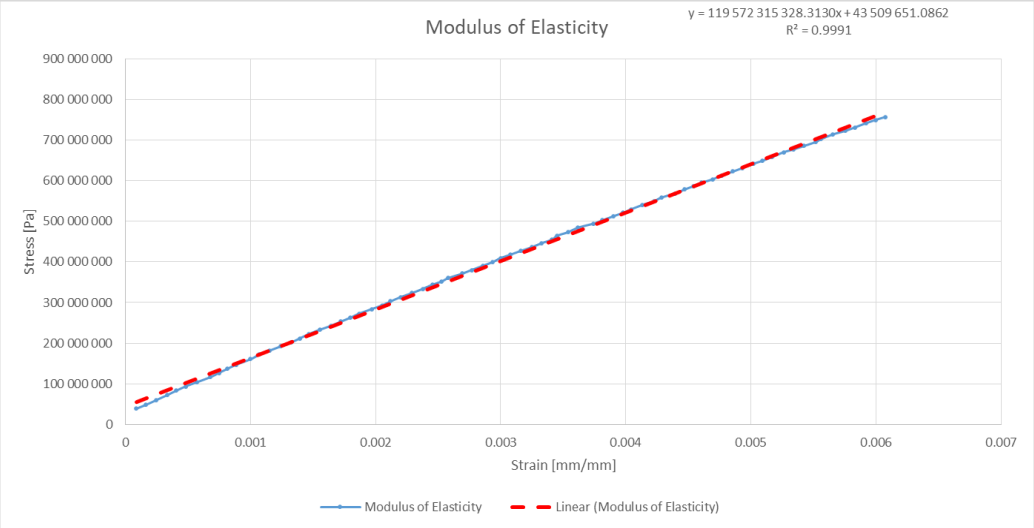

Figure A.2-2: Modulus of Elasticity for 90º tensile test specimen 1

The modulus of elasticity for the first tensile test specimen in the 90º-orientated specimens produces a gradient for the equation of 119 GPa.

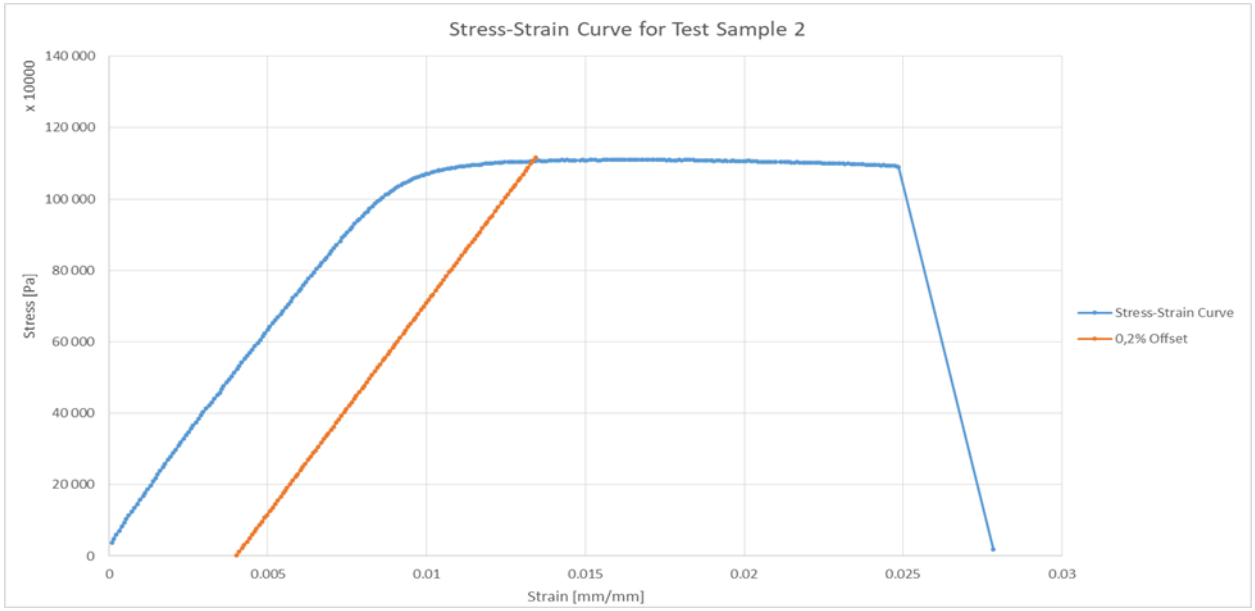

Figure A.2-3: Stress-Strain Curve for 90° tensile test specimen 2

From the figure above it is clear that the maximum stress is in the stress region of just above 1100 MPa, the yield stress is also in the region of the UTS. We also note that maximum strain is measured at around 0.025 mm/mm.

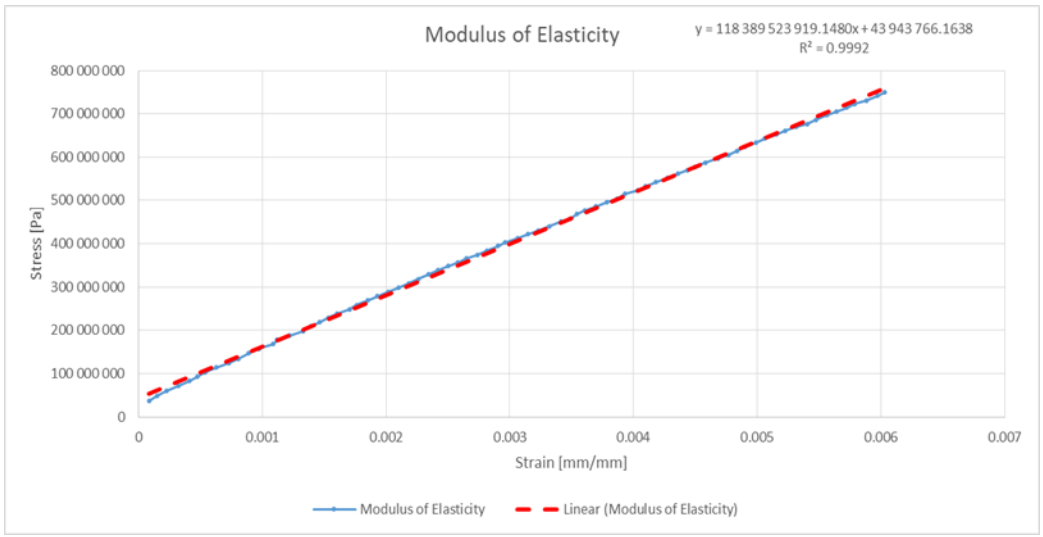

Figure A.2-4: Modulus of Elasticity for 90° tensile test specimen 2

From the equation it is noted that the modulus of elasticity for this specific test specimen is 118 GPa.

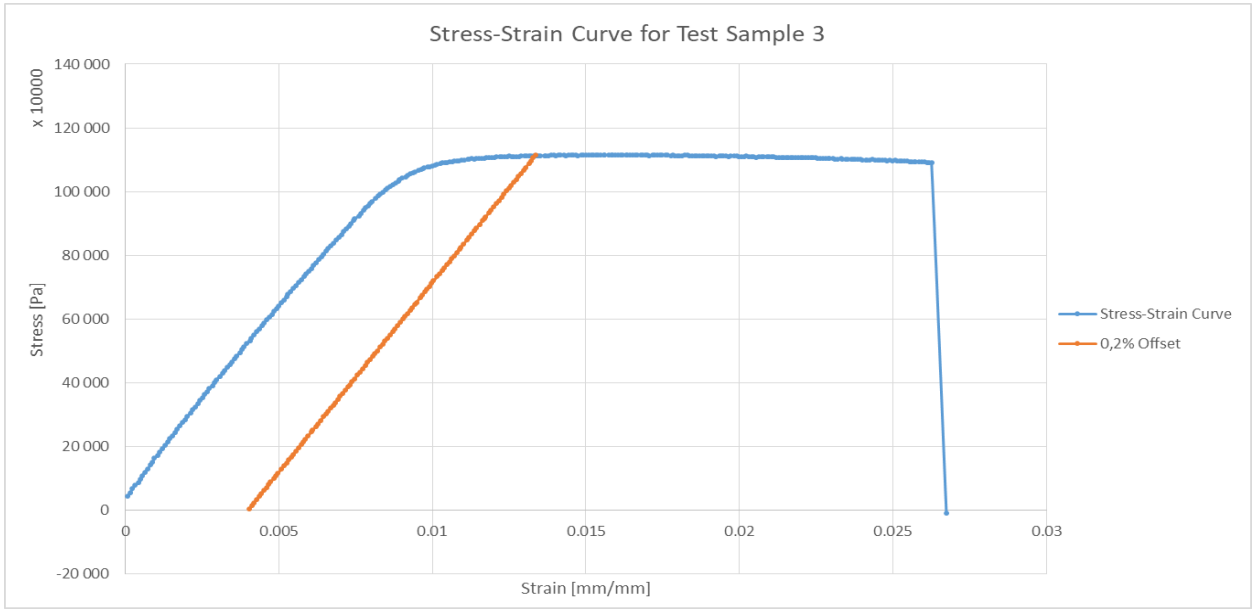

Figure A.2-5: Stress-Strain Curve for 90° tensile test specimen 3

From the figure above it is clear that the maximum stress is in the stress region of just above 1100 MPa, the yield stress is also in the region of the UTS. We also note that maximum strain is measured at around 0.025 mm/mm.

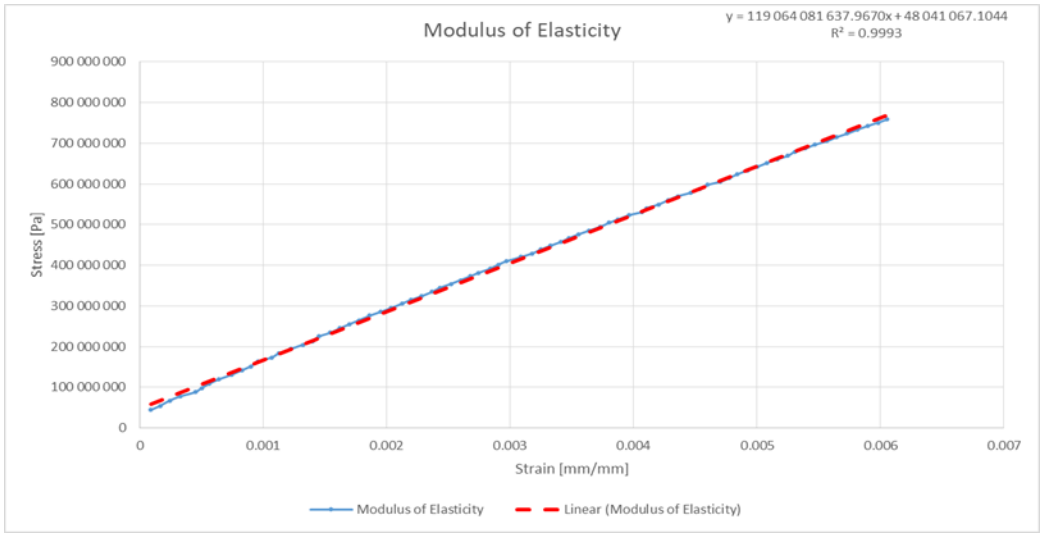

Figure A.2-6: Modulus of Elasticity for 90° tensile test specimen 3

The modulus of elasticity for this specimen, determined by plotting the stress-strain curve's elastic region, is noted as 119 GPa.

APPENDIX B

FATIGUE TESTS RESULTS

This section of the report gives the results obtained from the fatigue tests that were carried out. The DIC images of each specimen is included in this section together with specific SEM images of tests specimens that were analysed using a scanning electron microscope.

0º Fatigue test specimens

B.1 SPECIMEN B1

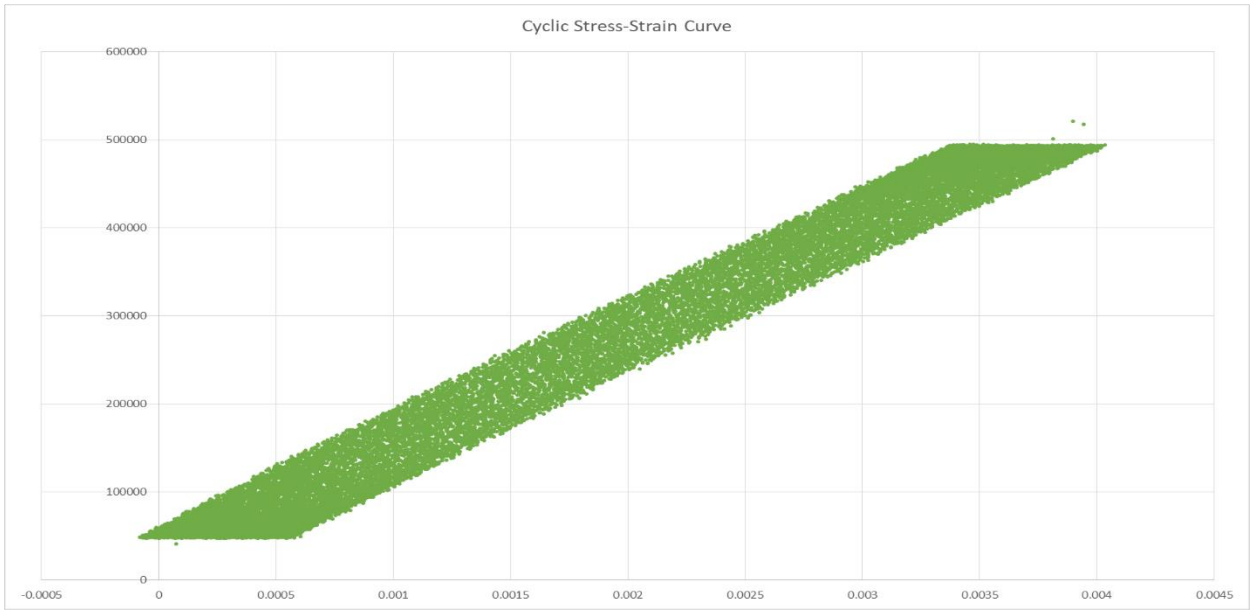

Figure B.1-1: Specimen B1 hysteresis stress-strain curve

Looking at figure B.1-1 it is clear that the stress-strain hysteresis curve shows a test specimen that does not strain a lot (a little more than 0.0005 mm/mm) before failure. It is also necessary to note that the hysteresis loop is the stress-strain plot for half-life of the fatigue test.

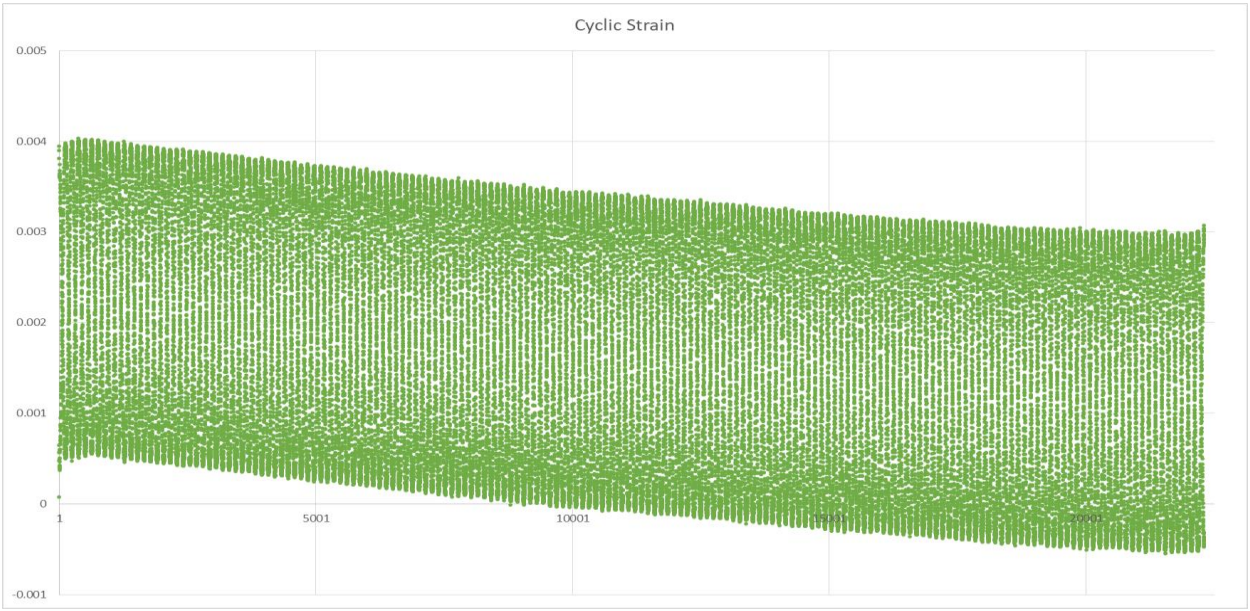

Figure B.1-2: Strain-life graph for specimen B1

From the strain-life graph for the test specimen it is noted that the test specimen begins the fatigue test with positive strain values for each cycle up until the test specimen half-life, whereafter the strain enters the negative value, which indicates that the test specimen experiences compression.

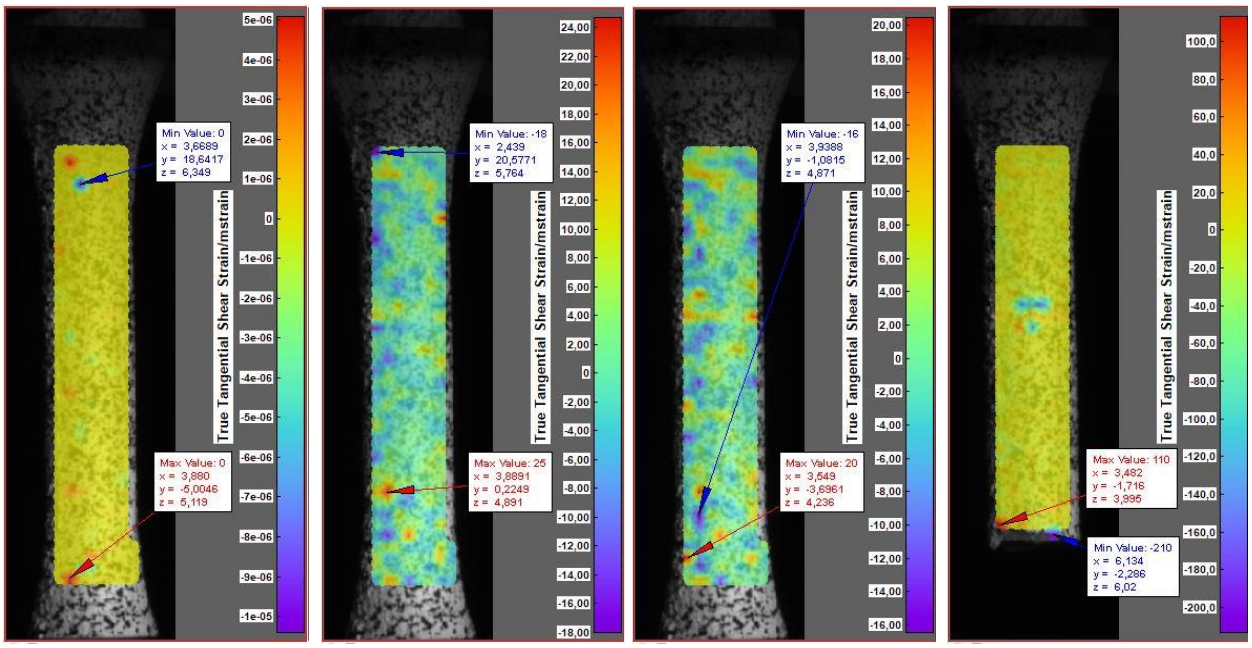

Figure B.1-3: From left to right: B1 reference image, B1 half-life image, B1 final image, B1 failure image

Looking at figure B.1-3, especially the final image, it is clear that the specimen broke in the bottom half of the test specimen's gauge area. A maximum value for the shear strain in the bottom of the test specimen, which is where it failed, is observed in the third images from the left.

B.2 SPECIMEN B2

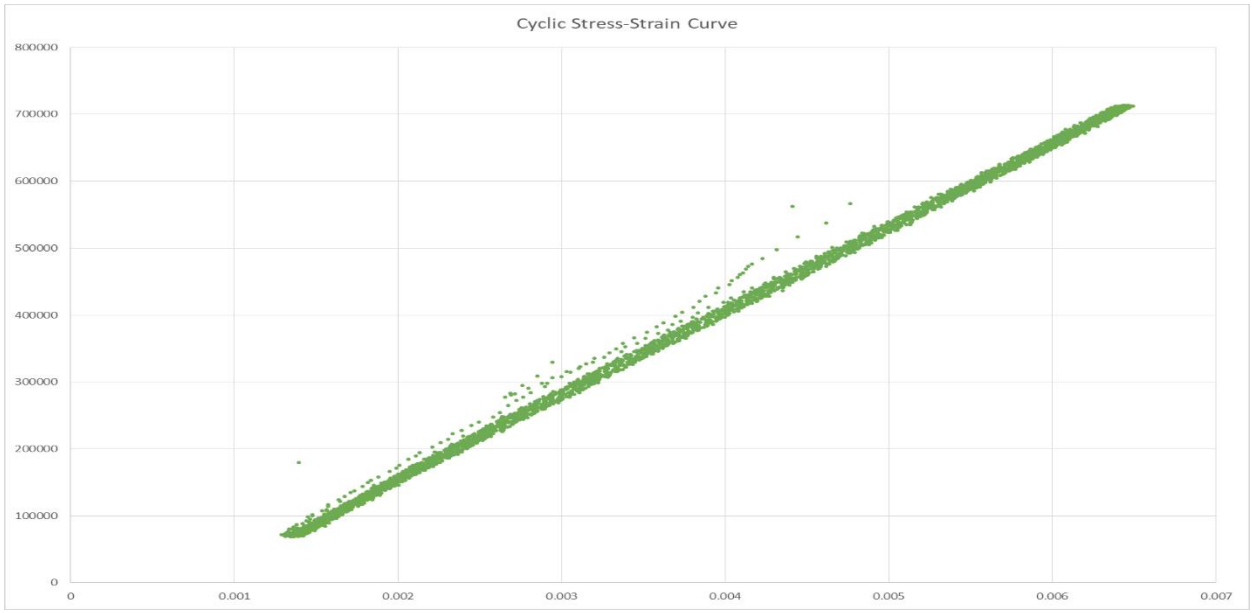

Figure B.2-1: Specimen B2 hysteresis stress-strain curve

For this test specimen the hysteresis stress-strain curve shows little change in the strain, with this being a stress-controlled fatigue test, before failure occurred.

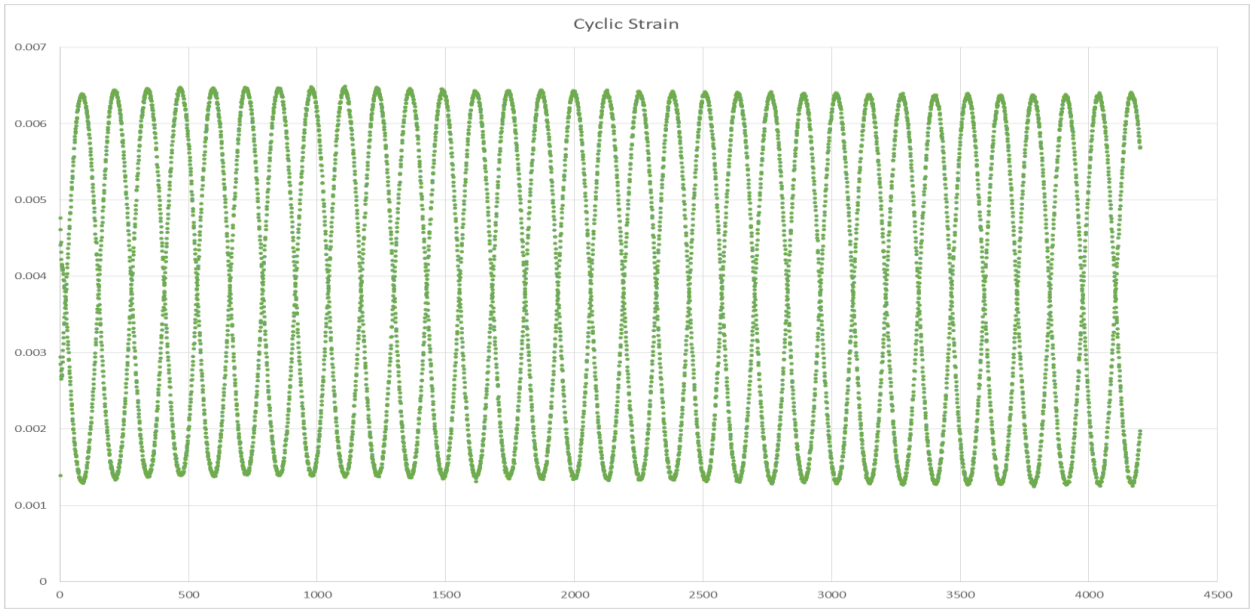

Figure B.2-2: Strain life graph for specimen B2

The strain life of the specimen shows no change in the peak values for strain during the entirety of the fatigue test which lasted just more than 4000 cycles.

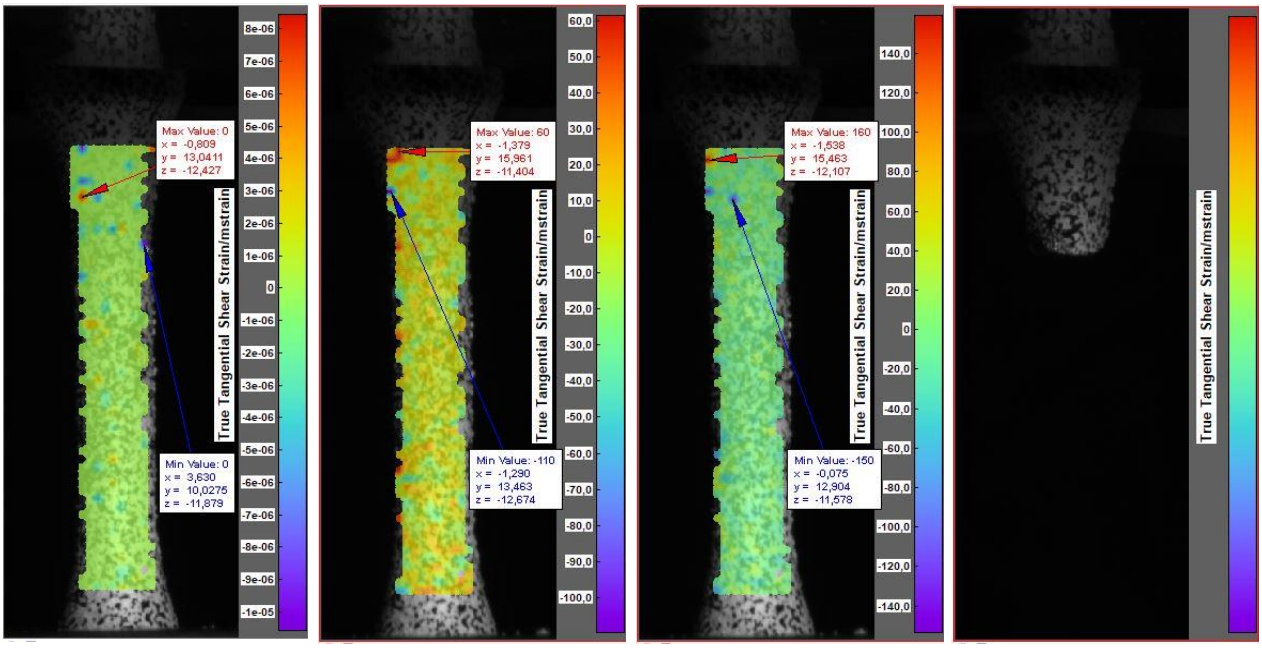

Figure B.2-3: From left to right: B2 reference image, B2 half-life image, B2 final image, B2 failure image

From the images above we can see that the specimen broke in the upper part of the gauge area, with a maximum value for the shear strain indicated (third image from left) right at the top of the specimen.

B.3 SPECIMEN B3

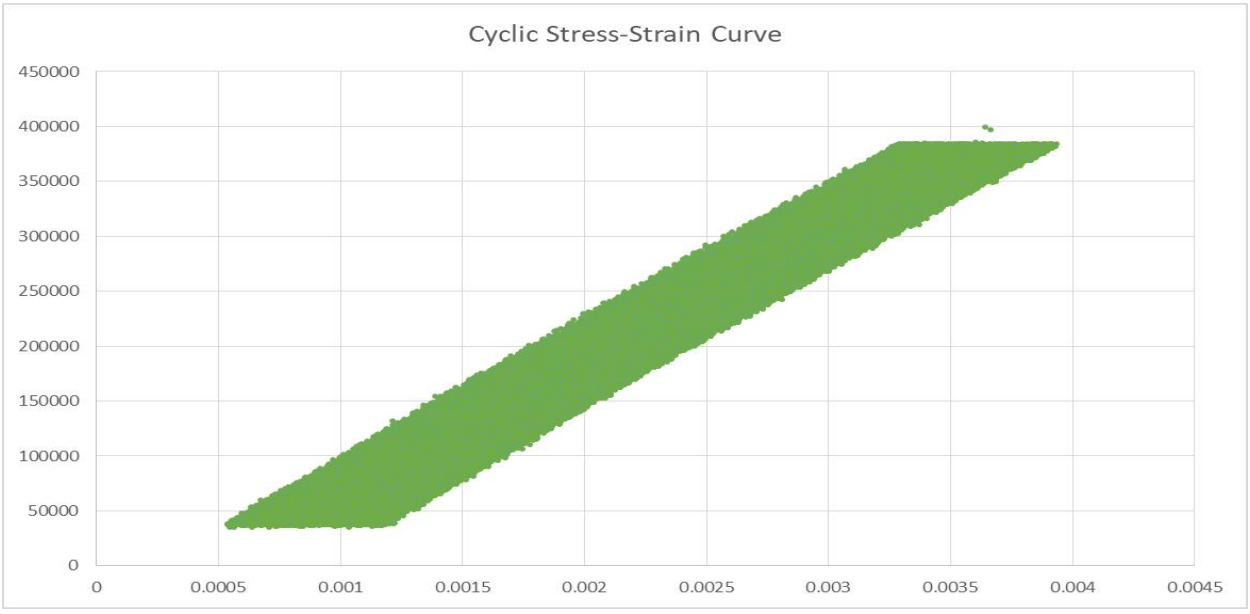

Figure B.3-1: Hysteresis stress-strain curve for specimen B3

As with the other hysteresis curves in this section the constant stress is applied during fatigue testing and change in strain is plotted. The change is not significant (just a little more than 0.0005 mm/mm) indicating a hard and brittle material.

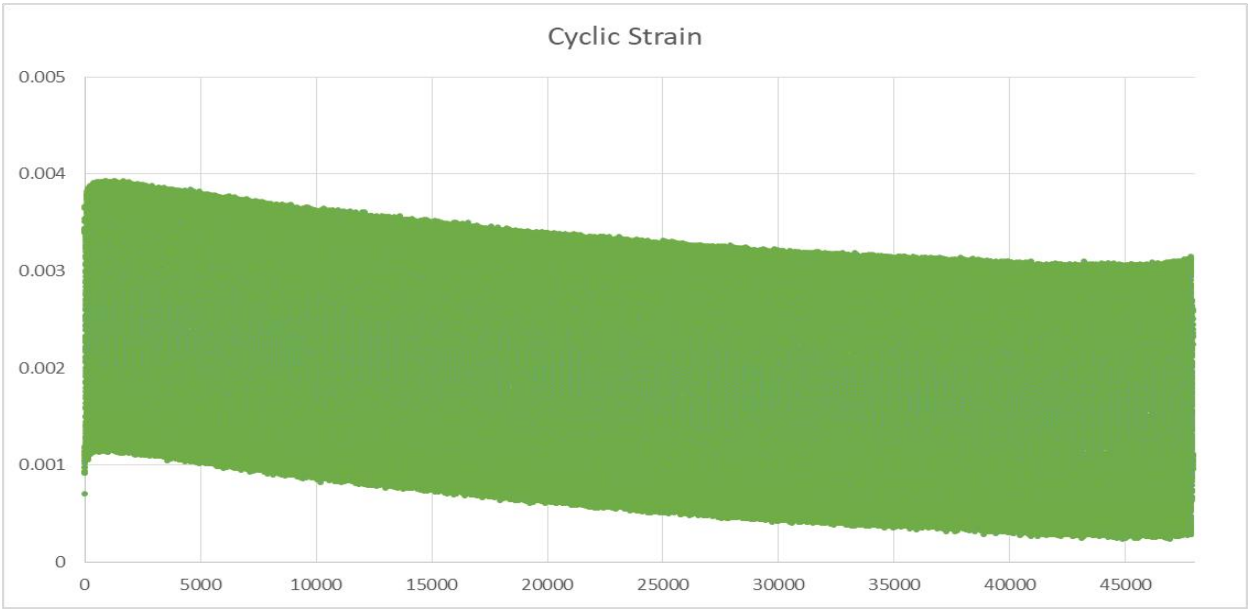

Figure B.3-2: Strain life graph for specimen B3

From figure B.3-2 we see that the peak values for the strain reduces as the fatigue life grows. A constant stress fatigue test is carried out on the specimen and it breaks after 45 000 cycles.

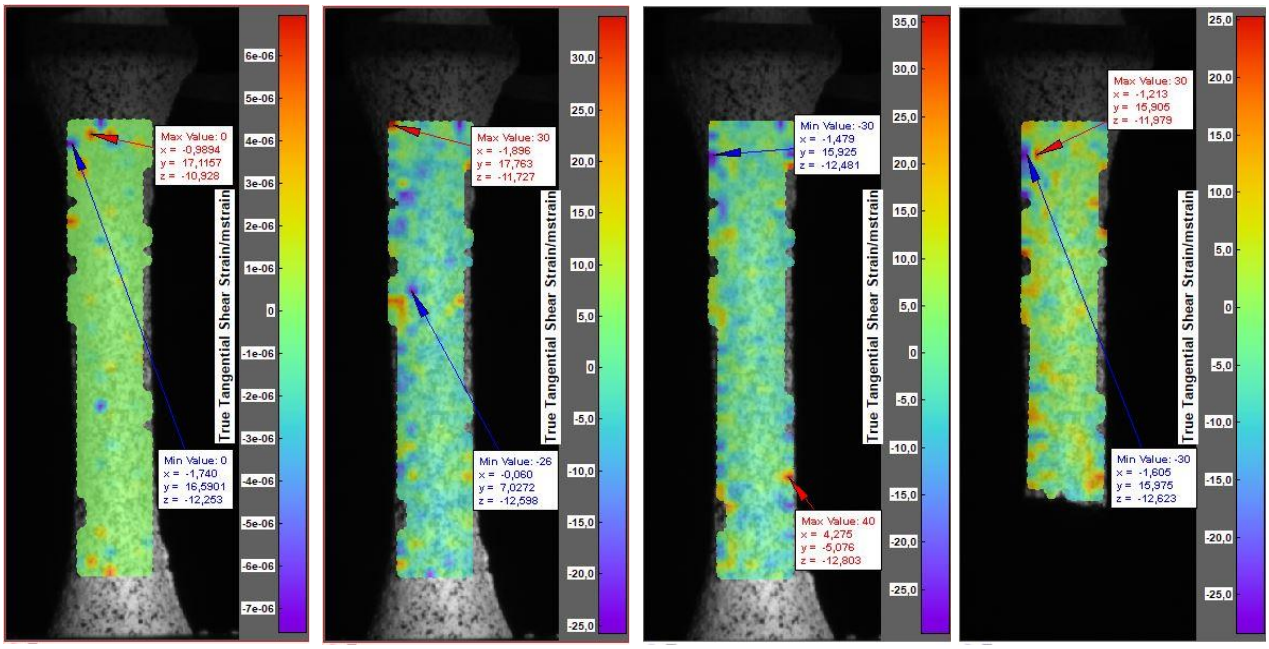

Figure B.3-3: From left to right: B3 reference image, B3 half-life image, B3 final image, B3 failure image

The images illustrated above reveal, by looking at the image third from the left in particular, that there is a maximum shear strain concentration near the point of failure, but the maximum shear strain is not observed in the same position at the half-life image.

B.4 SPECIMEN B4

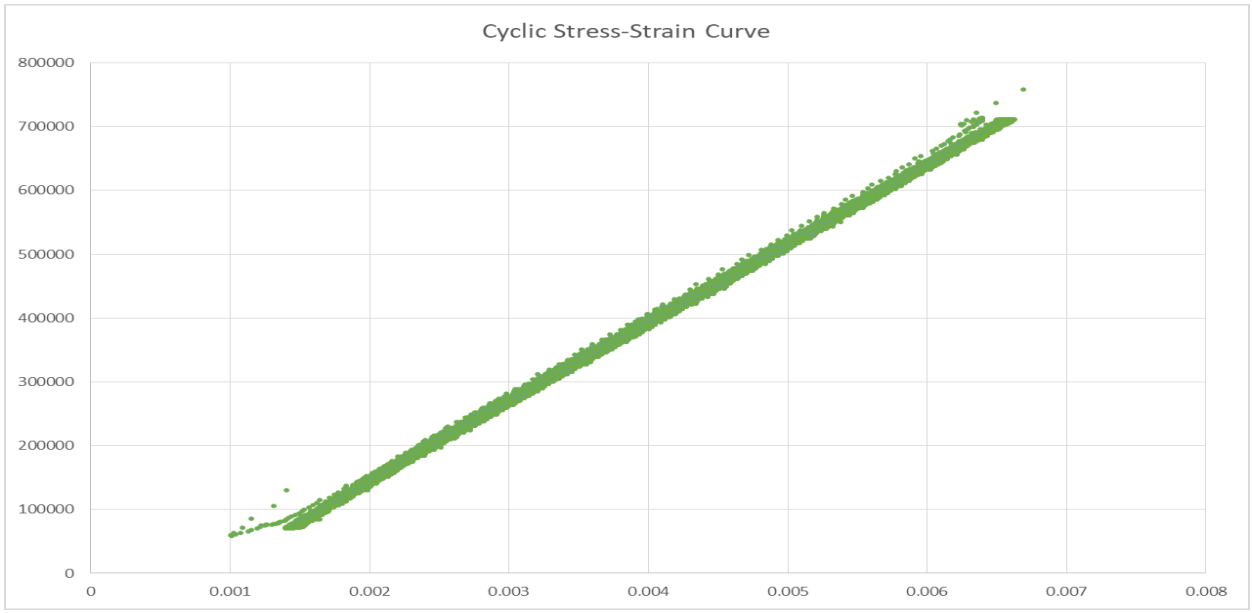

Figure B.4-1: Hysteresis stress-strain curve for specimen B4

Hysteresis stress-strain curve for specimen B4, showing very little change in strain after constant stress fatigue tests are carried out on it.

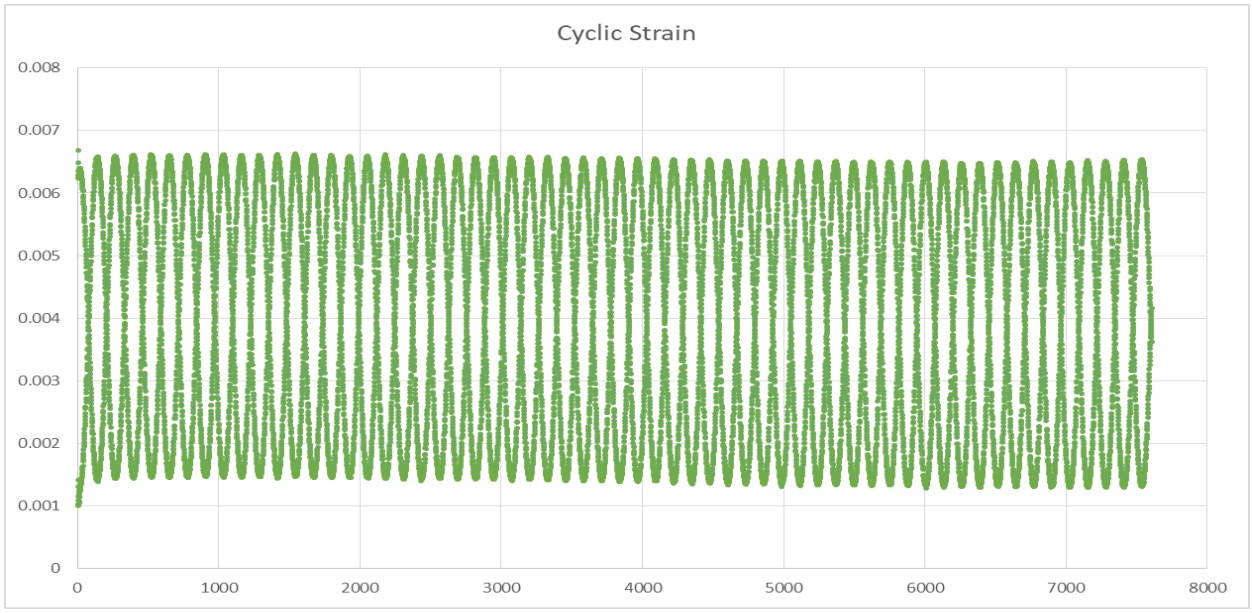

Figure B.4-2: Strain life graph for specimen B4

Strain life graph for specimen B4 showing relative constant strain range for the fatigue test. This indicates a brittle material as very little deformation is indicated.

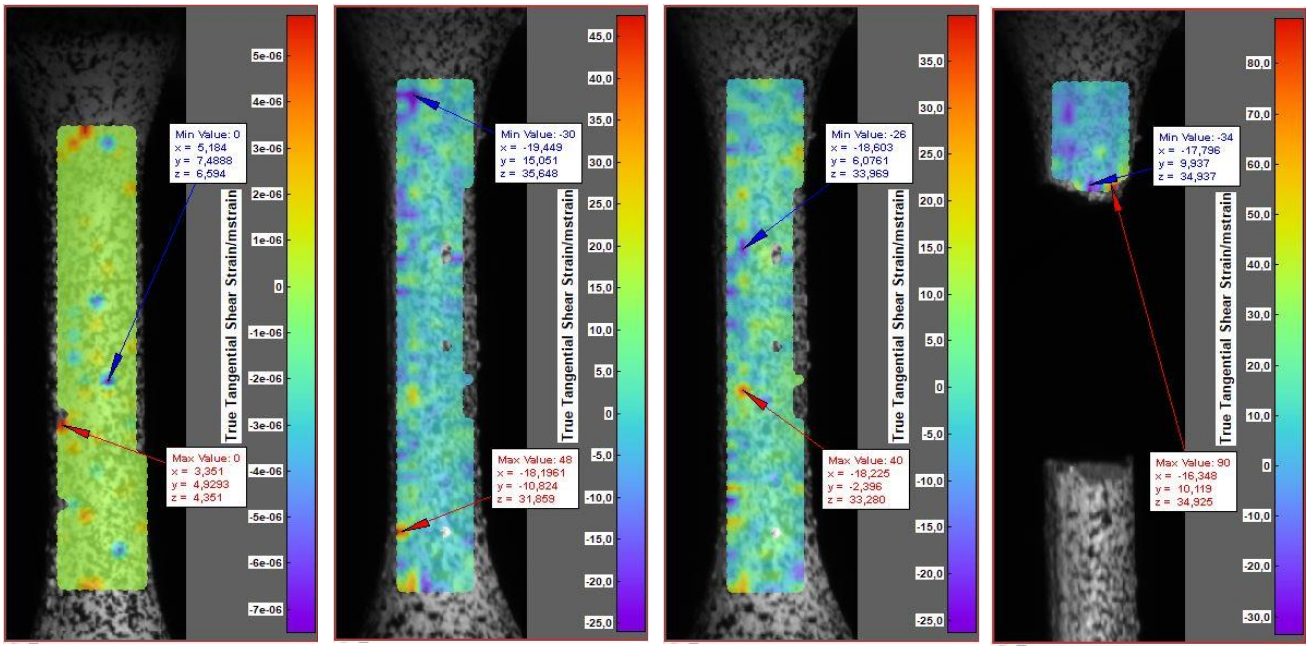

Figure B.4-3: From left to right: B4 reference image, B4 half-life image, B4 final image, B4 failure image

The images show a maximum stress concentration at a point just below the halfway point of the gauge area of the test specimen while the specimen broke at the top of the test specimen's gauge area.

B.5 SPECIMEN B5

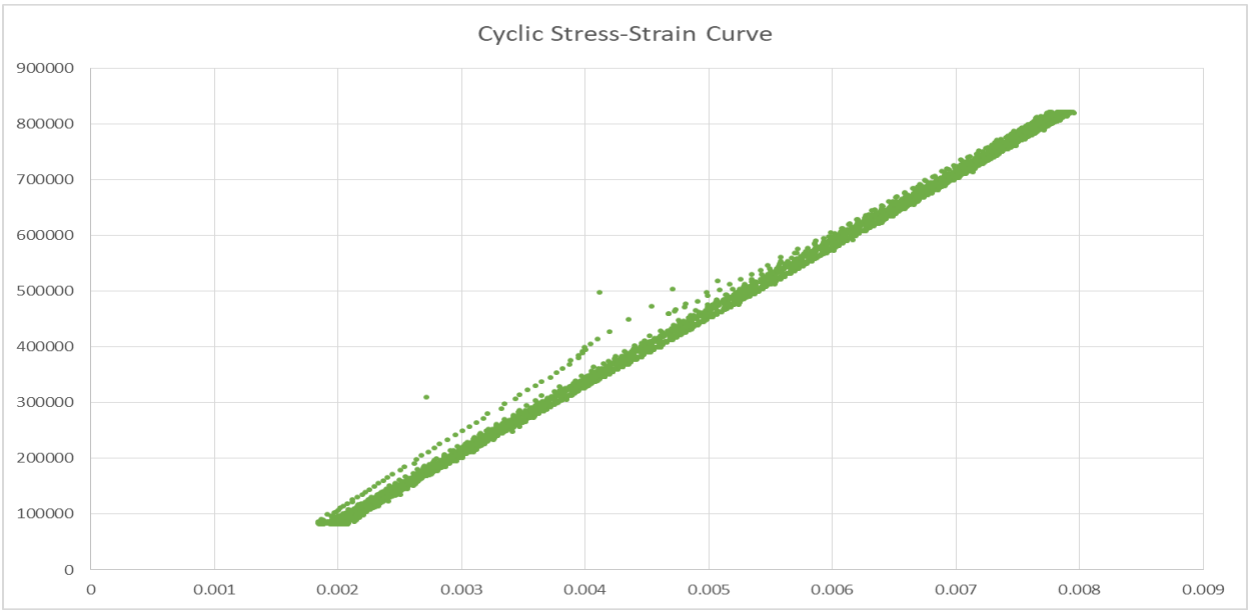

Figure B.5-1: Hysteresis stress-strain curve for specimen B5

As with the other test specimens, specimen B5 does not show drastic signs of strain.

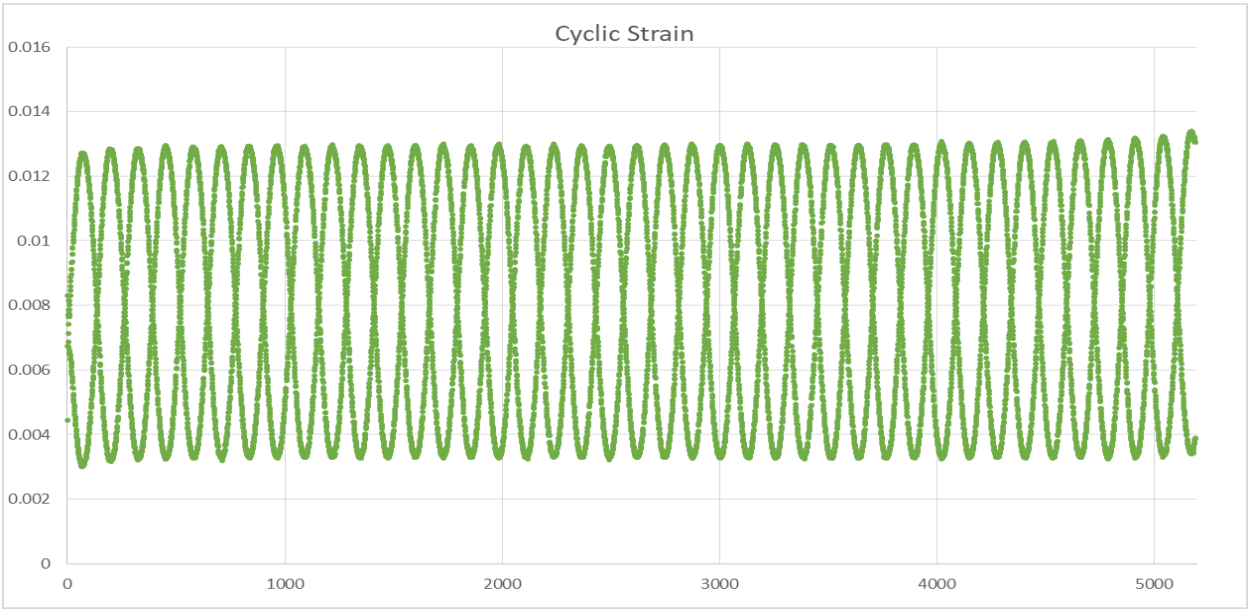

Figure B.5-2: Strain-life graph for specimen B5

The cyclic strain-life as seen in Figure B.5-2 shows that the strain remains more or less constant except when it nears the end, where the strain increases to a degree before failure.

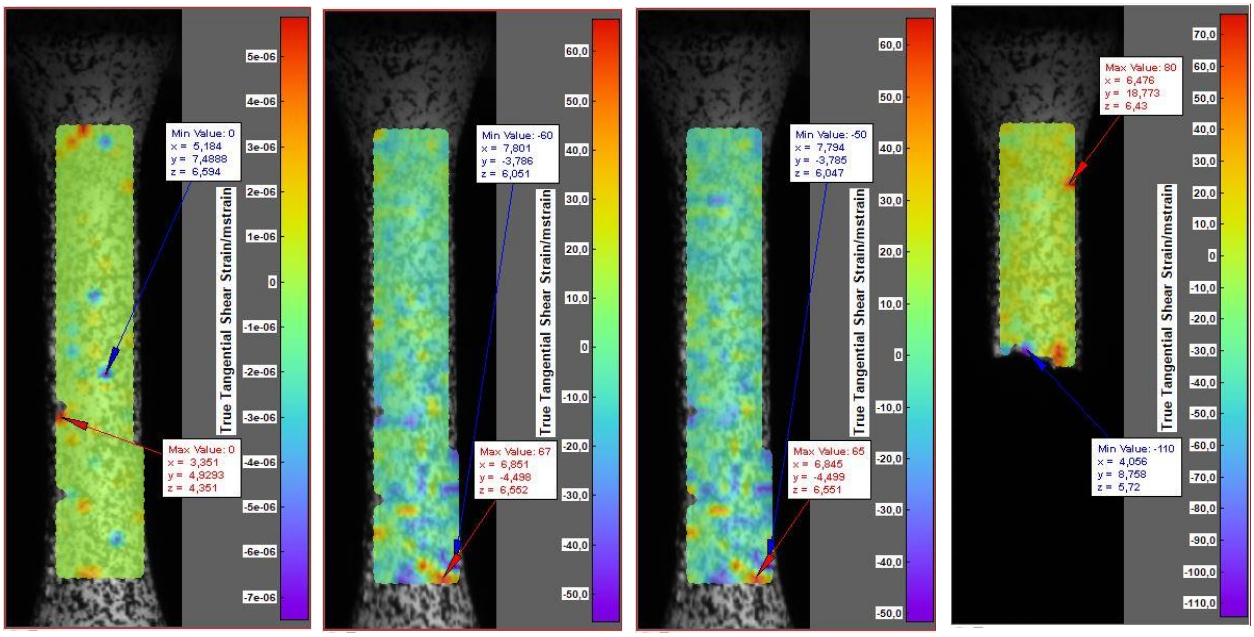

Figure B.5-3: From left to right: B5 reference image, B5 half-life image, B5 final image, B5 failure image

From the DIC images taken of specimen B5 it is clear that the maximum strain the moment before failure is nowhere near the actual point of failure. The specimen broke in the middle of the gauge length whilst the final image shows the maximum shear strain concentration at the bottom of the test specimen.

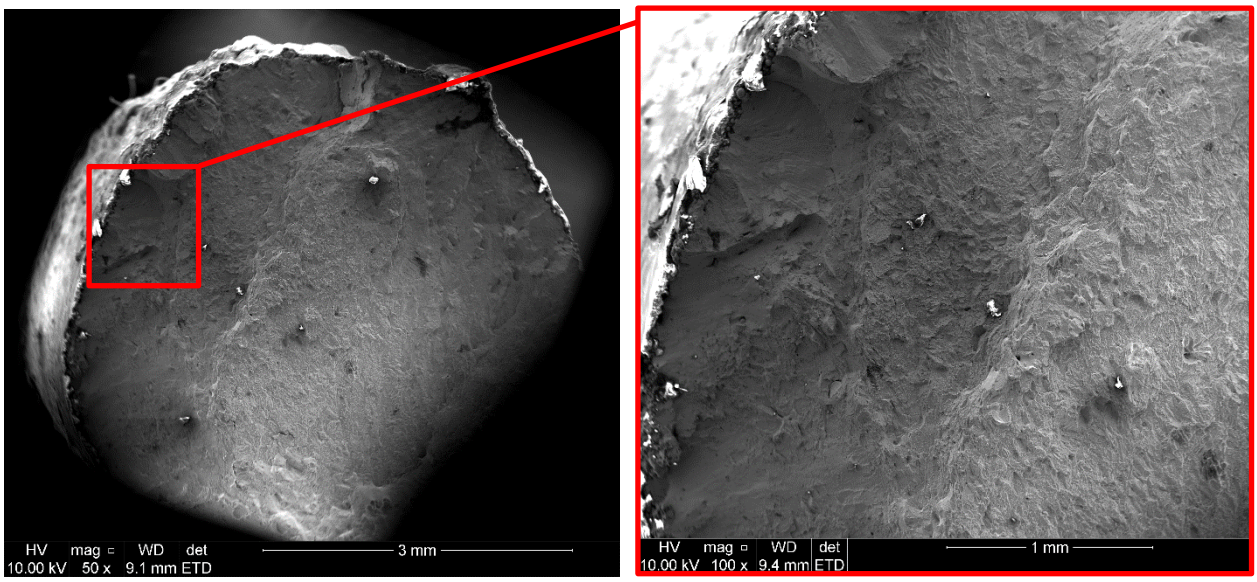

Figure B.5-4: SEM image of specimen B5

This SEM image taken of the specimen is taken at the interface where the specimen broke. The cross-sectional area is photographed revealing a small surface defect in the right image.

B.6 SPECIMEN B6

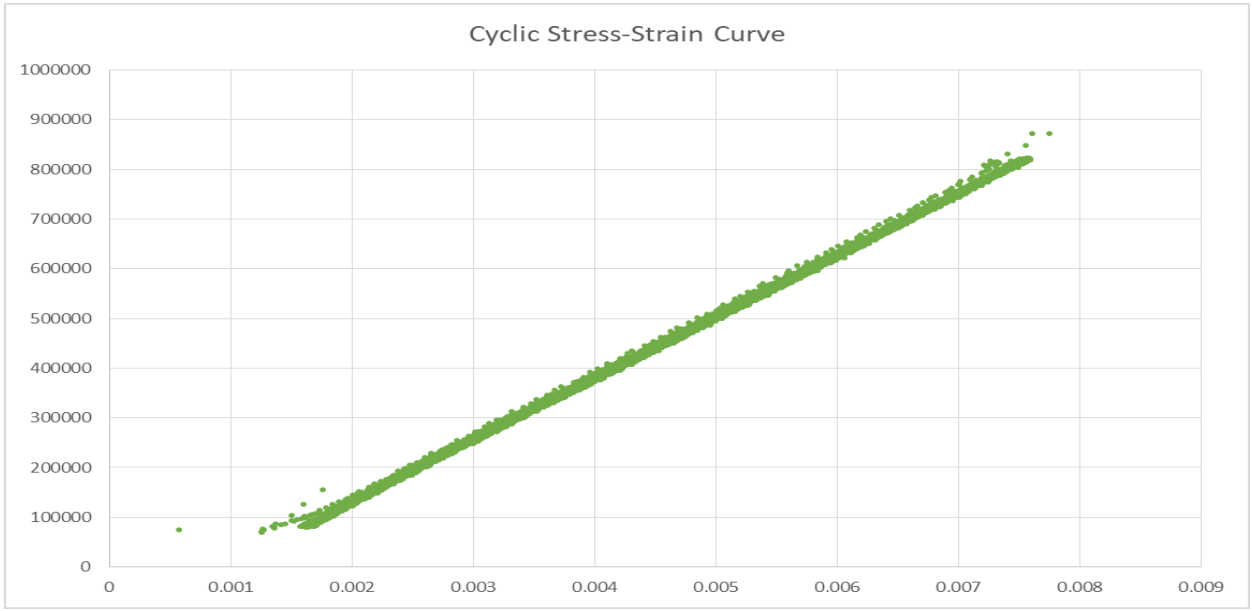

Figure B.6-1: Hysteresis stress-strain curve for specimen B6

Test specimen B6, just like most of the previous specimens, does not show any significant signs of strain, when constant stress fatigue tests are carried out.

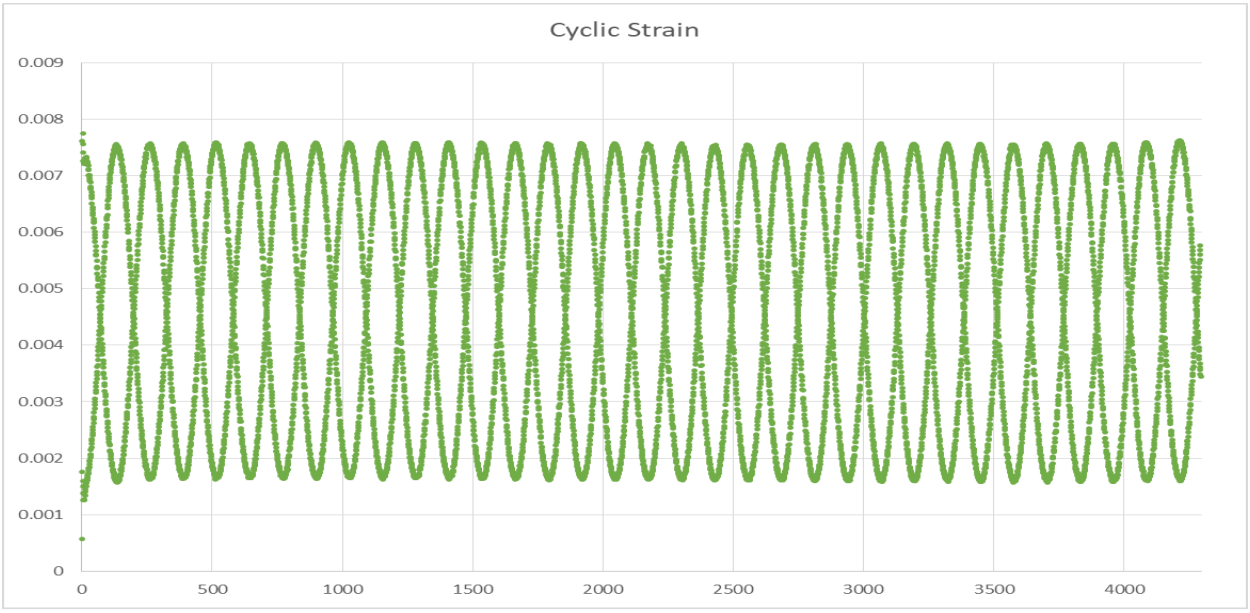

Figure B.6-2: Strain-life graph for specimen B6

Looking at the strain-life graph for the specimen, it is clear that the strain does not vary much from the initial strain when the fatigue test is started.

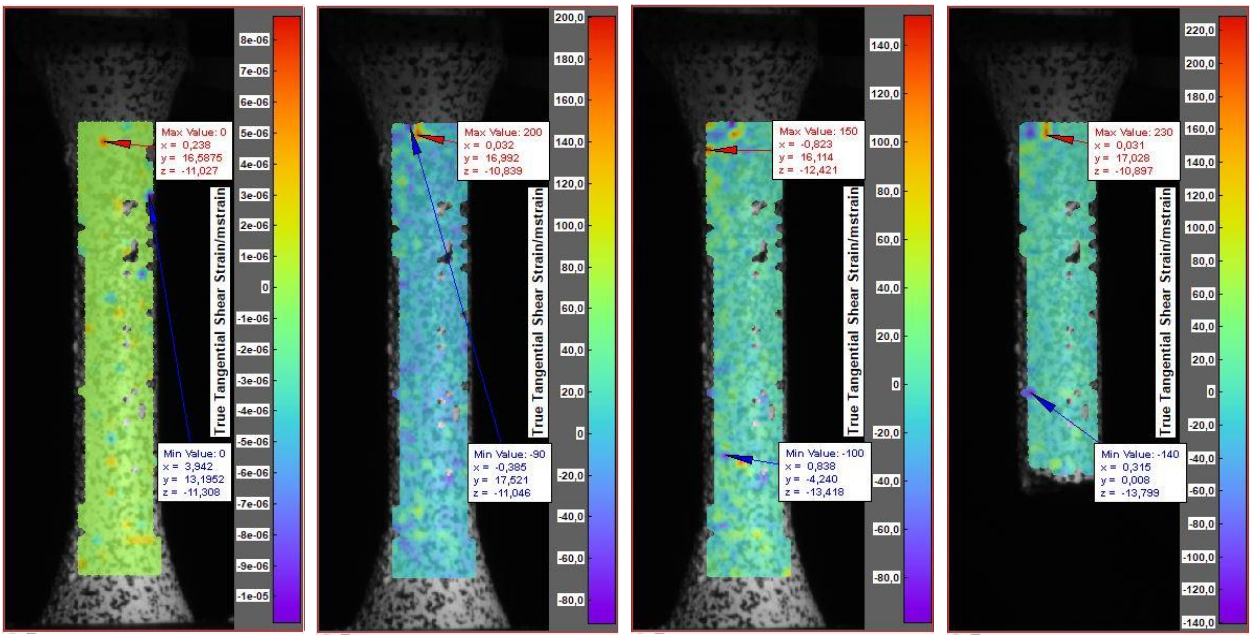

Figure B.6-3: From left to right: B6 reference image, B6 half-life image, B6 final image, B6 failure image

Looking at the images, it is easy to note that the area where the test specimen broke, and the area where the final image before failure says a maximum shear strain is, are different. The specimen broke at the bottom of the gauge length and the maximum shear strain is located at the top of the specimen.

B.7 SPECIMEN B7

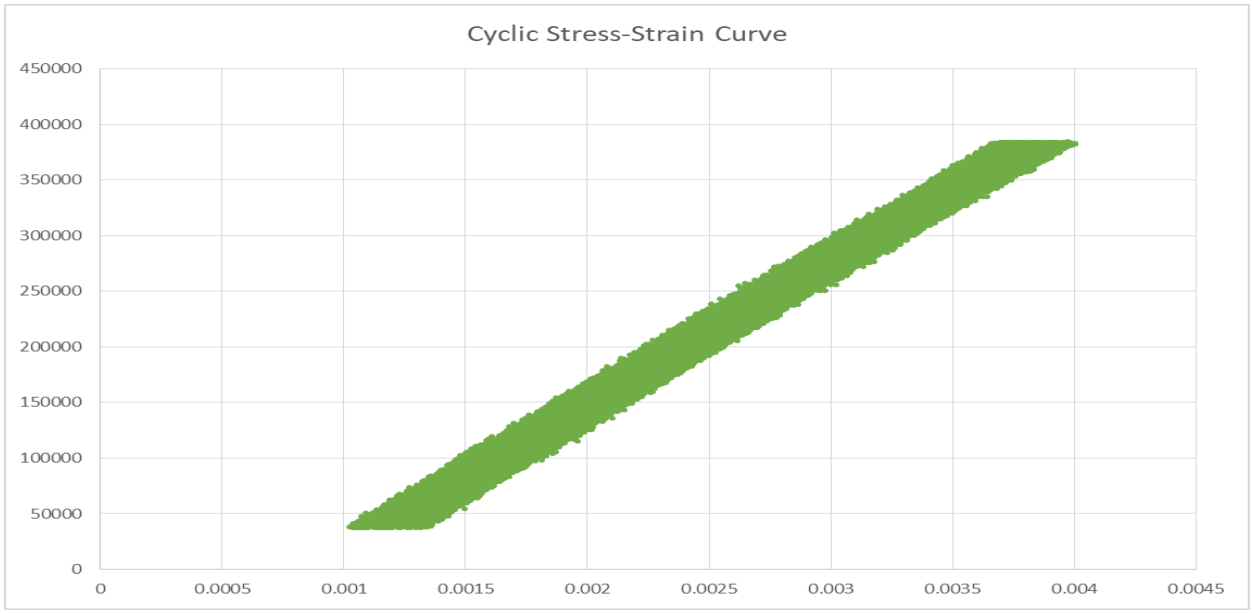

Figure B.7-1: Hysteresis stress-strain curve for specimen B7

As with the other specimens in this study, this specimen does not show significant strain development (a little less than 0.0005 mm/mm) during the fatigue test's first 15 000 cycles.

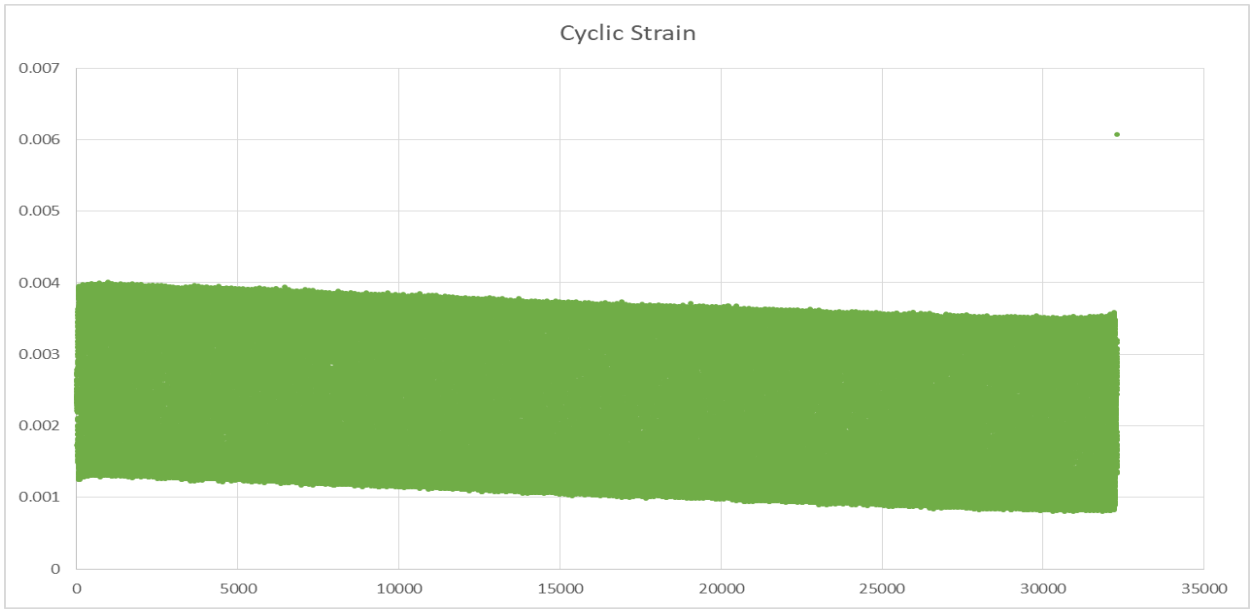

Figure B.7-2: Strain-life curve for specimen B7

The strain-life curve does not stay as constant with no change in peak values as previous specimens, but also has more cycles and once it has passed 5000 cycles the strain peak values begin to decrease.

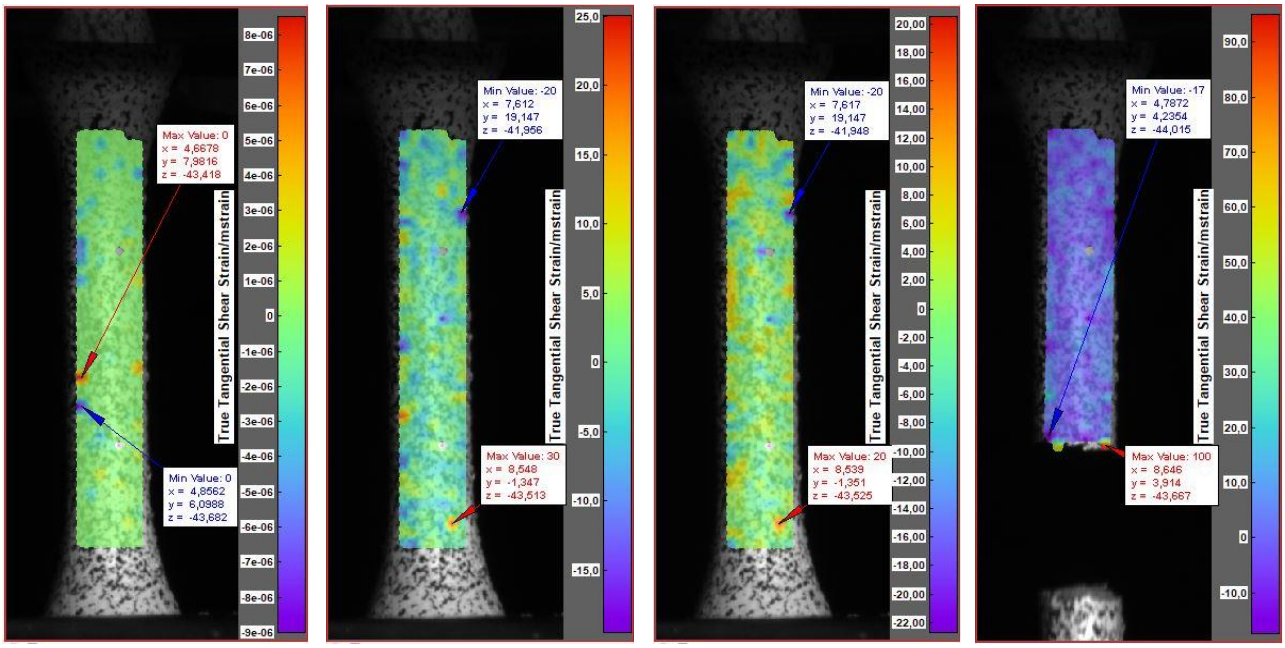

Figure B.7-3: From left to right: B7 reference image, B7 half-life image, B7 final image, B7 failure image

From the DIC data the images show that the test specimen broke near the region where the image before the specimen breaks indicates a maximum value for the shear strain concentration is.

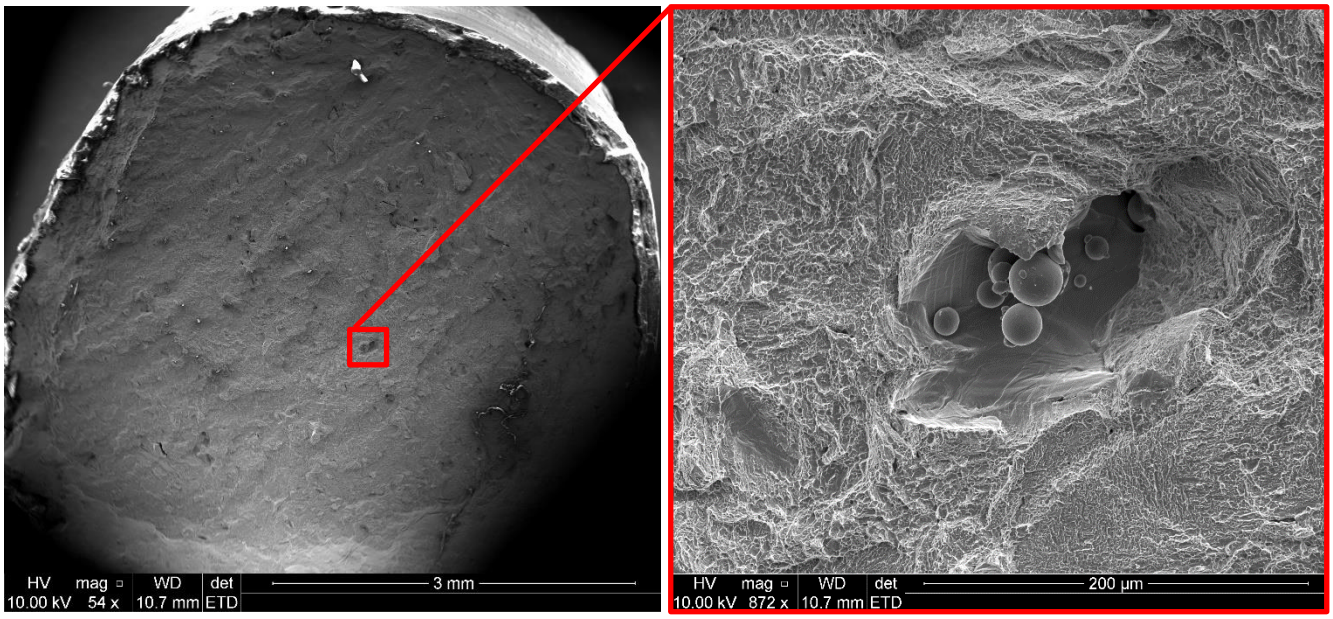

Figure B.7-4: SEM images for specimen B7

The SEM images from the specimen shows a common defect that occurs during the manufacturing process. The internal defect contains some unsintered metal powder and measures around 200 µm in length.

B.8 SPECIMEN B8

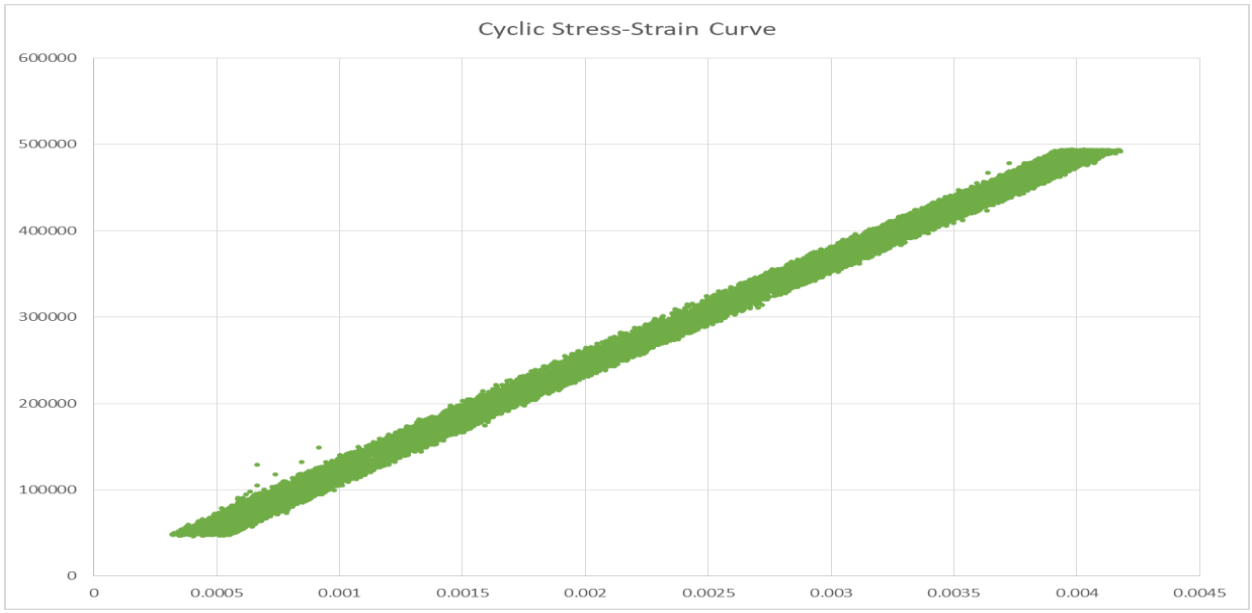

Figure B.8-1: Hysteresis stress-strain curve for specimen B8

The hysteresis curve for specimen B8 is shown and as with the other test specimens there is not a large variance in strain before failure occurs.

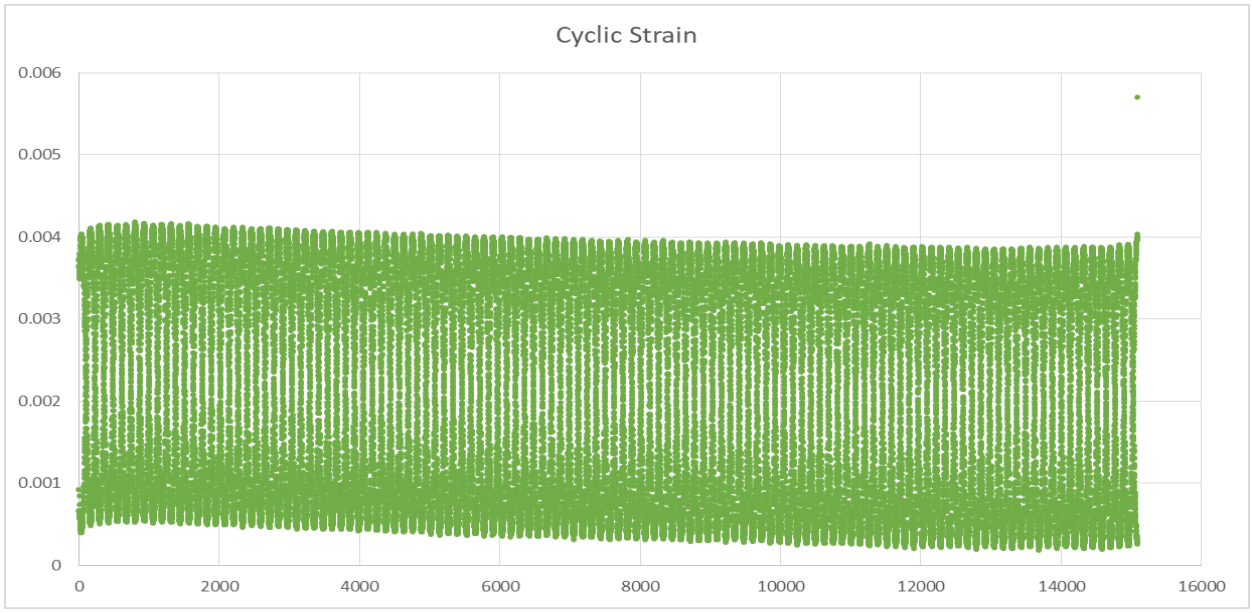

Figure B.8-2: Strain-life graph for specimen B8

The strain-life graph shows reasonable constant strain up until the 6000th cycle after which the strain reduces slightly.

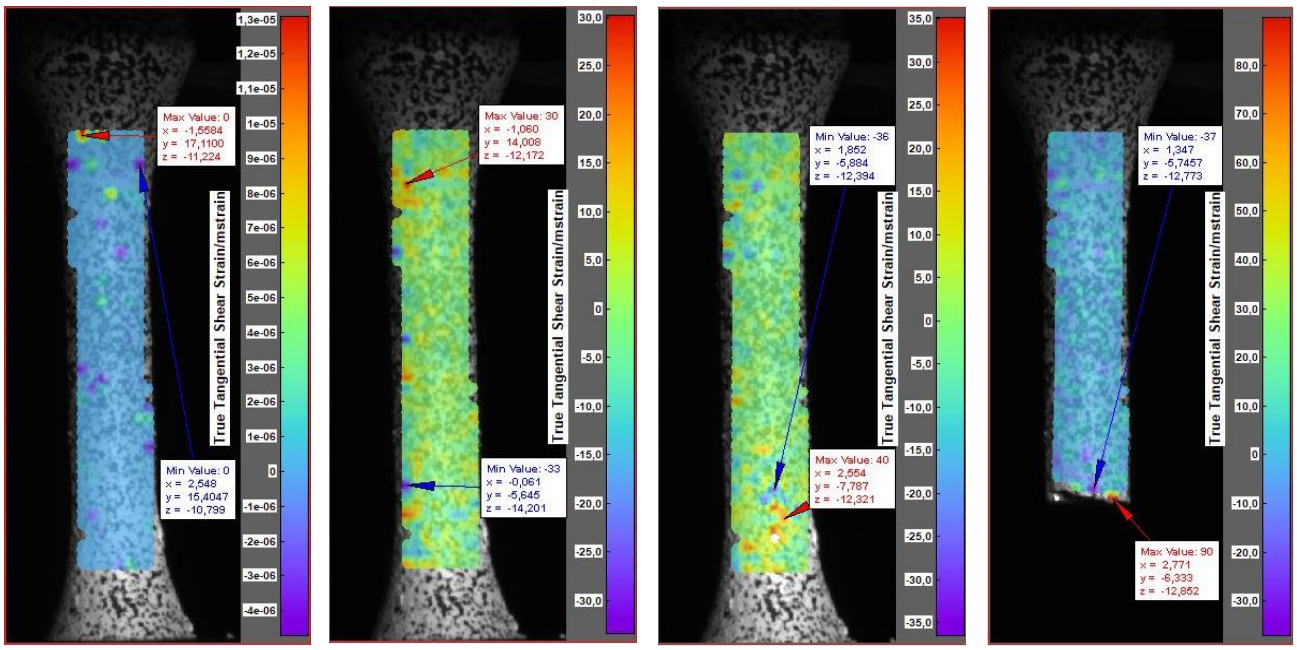

Figure B.8-3: From left to right: B8 reference image, B8 half-life image, B8 final image, B8 failure image

The third image from the left (the final image before failure) shows a shear strain concentration in the region of the gauge length very close to but not exactly at the point where the specimen failed. It cannot be seen at the half-life of the test specimen.

B.9 SPECIMEN B9

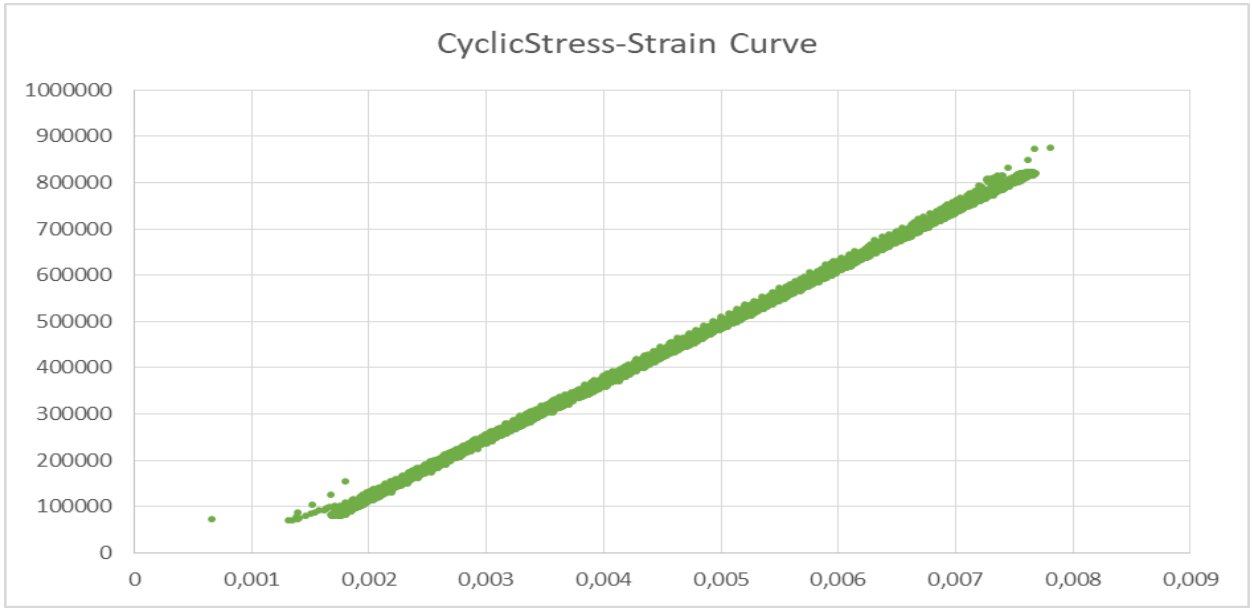

Figure B.9-1: Hysteresis stress-strain curve for specimen B9

This specimen was subjected to a high stress during the fatigue testing. It is clear from figure 9-27 that there is no significant strain for the specimen until failure.

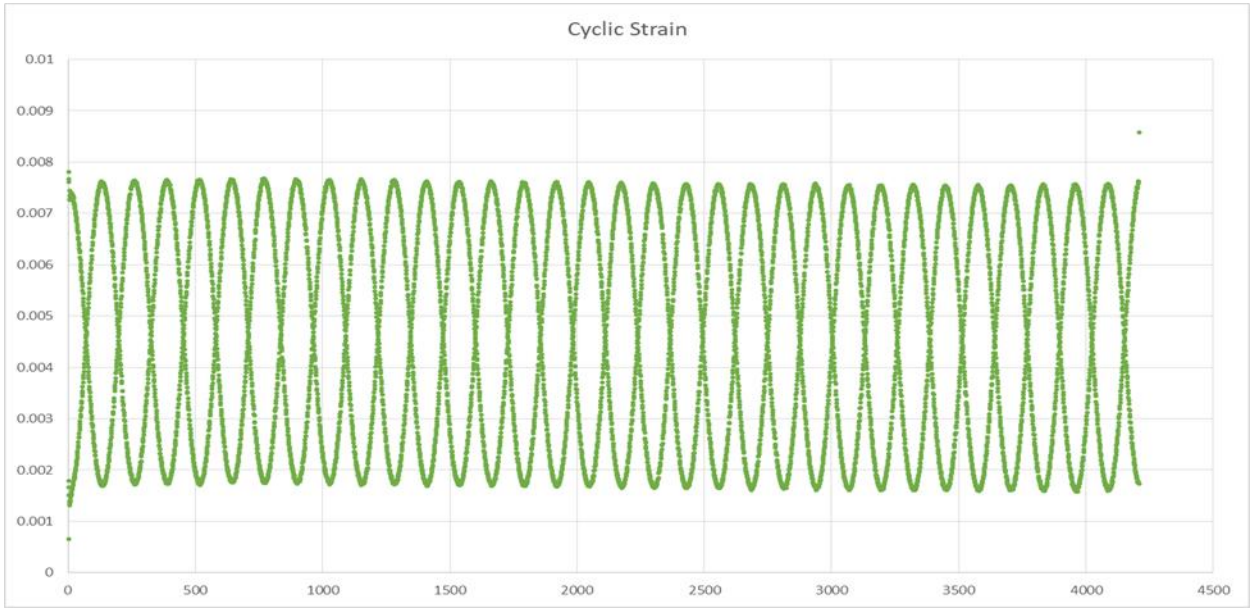

Figure B.9-2: Strain-life graph for specimen B9

Figure B.9-2 reaffirms what was stated in regard to Figure B.9-1 with there being no significant change in the strain that the specimen experiences up until failure occurs.

For this specimen there are no DIC images available. This is due to a power outage that occurred during testing.

B.10 SPECIMEN B10

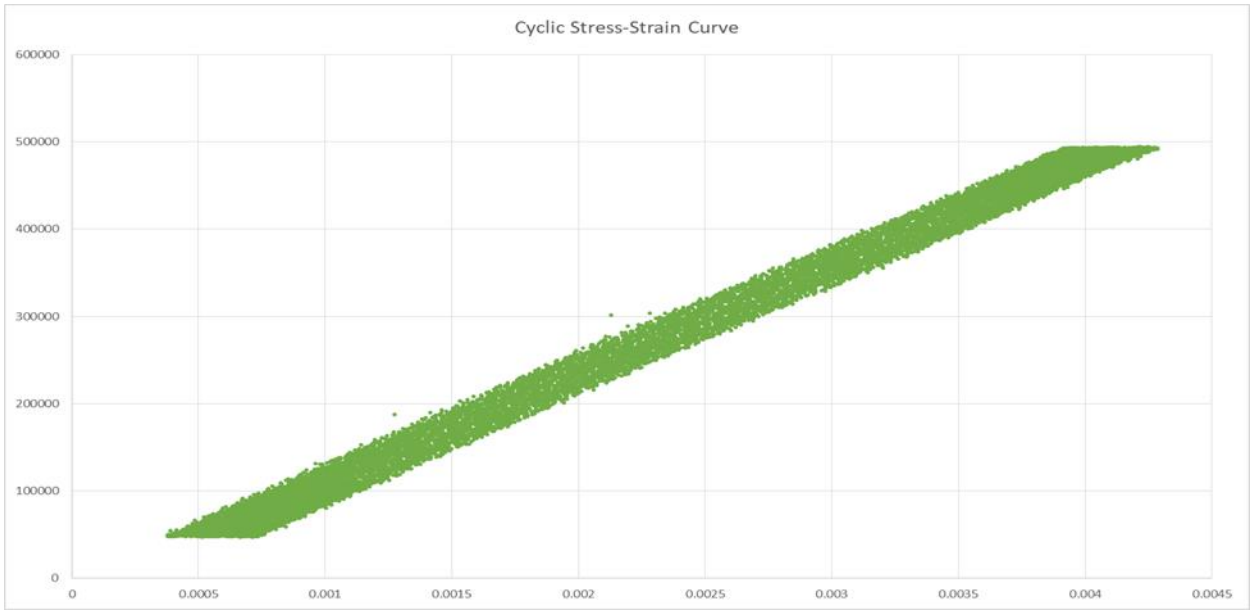

Figure B.10-1: Hysteresis stress-strain curve for specimen B10

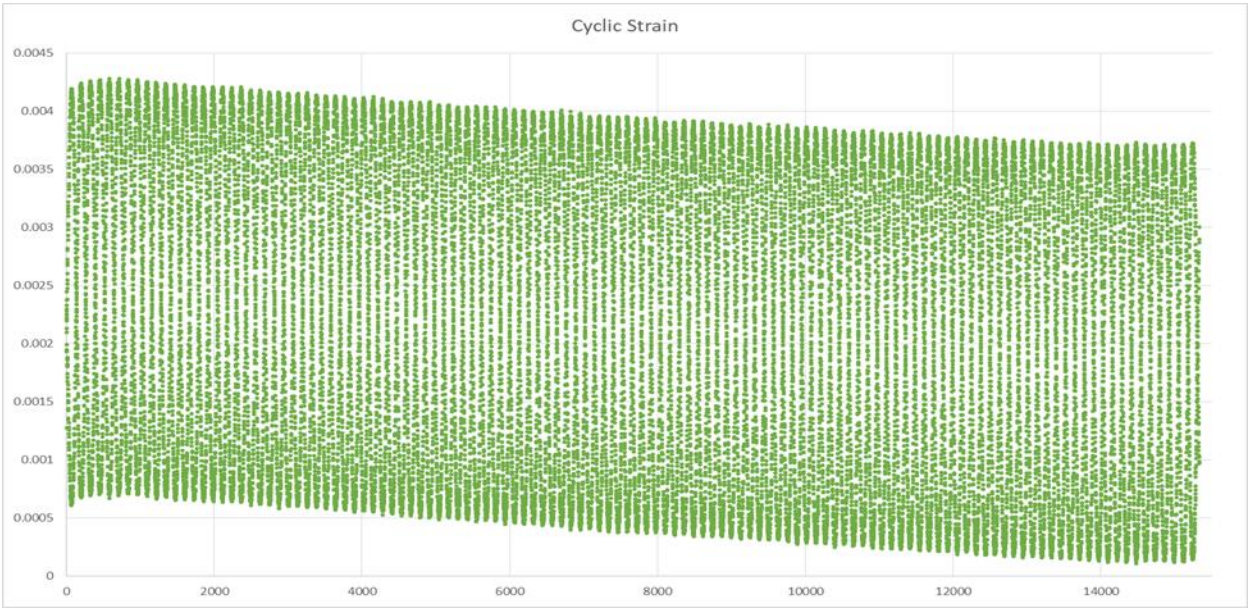

Figure B.10-2: Strain-life graph for specimen B10

From figures B.10-1 and B.10-2 it is clear that there is no significant change in the peak strain values which the specimen experiences up until the 3 000 cycle mark after which the peak values decrease.

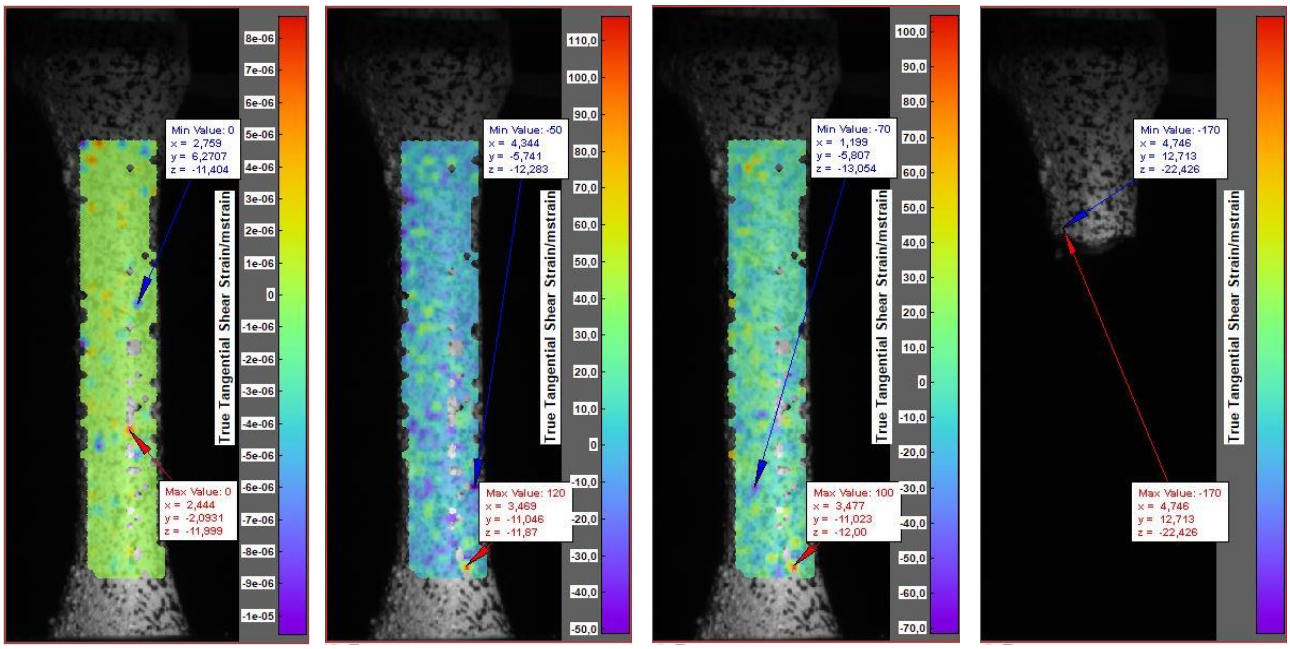

Figure B.10-3: From left to right: B10 reference image, B10 half-life image, B10 final image, B10 failure image

The images show no correlation between the areas where the maximum shear strain concentration is shown and where the test specimen failed. The maximum shear strain is indicated at the bottom of the test specimen with the failure point located at the top of the test specimen.

B.11 SPECIMEN B11

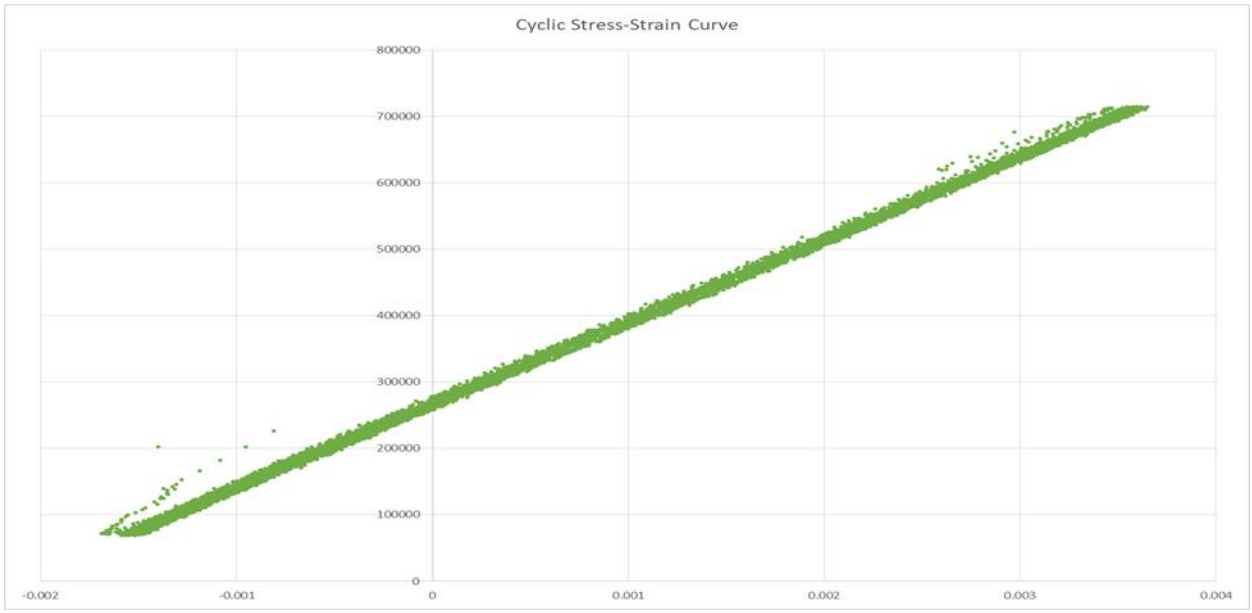

Figure B.11-1: Hysteresis stress-strain curve for specimen B11

From figure B.11-1 it is noticed that the specimen starts the fatigue test in compression, this is due to operator error with the MTS landmark. The test that was carried out was still a tensile-tensile test but the relaxation point was set to where the specimen was being compressed a bit by the machine. Regardless, no significant strain development is noticed in this specimen.

Figure B.11-2: Strain-life graph for specimen B11

From Figure B.11-2 it is clear that there is compression present, but more important to notice is that the strain does not grow during the fatigue test.

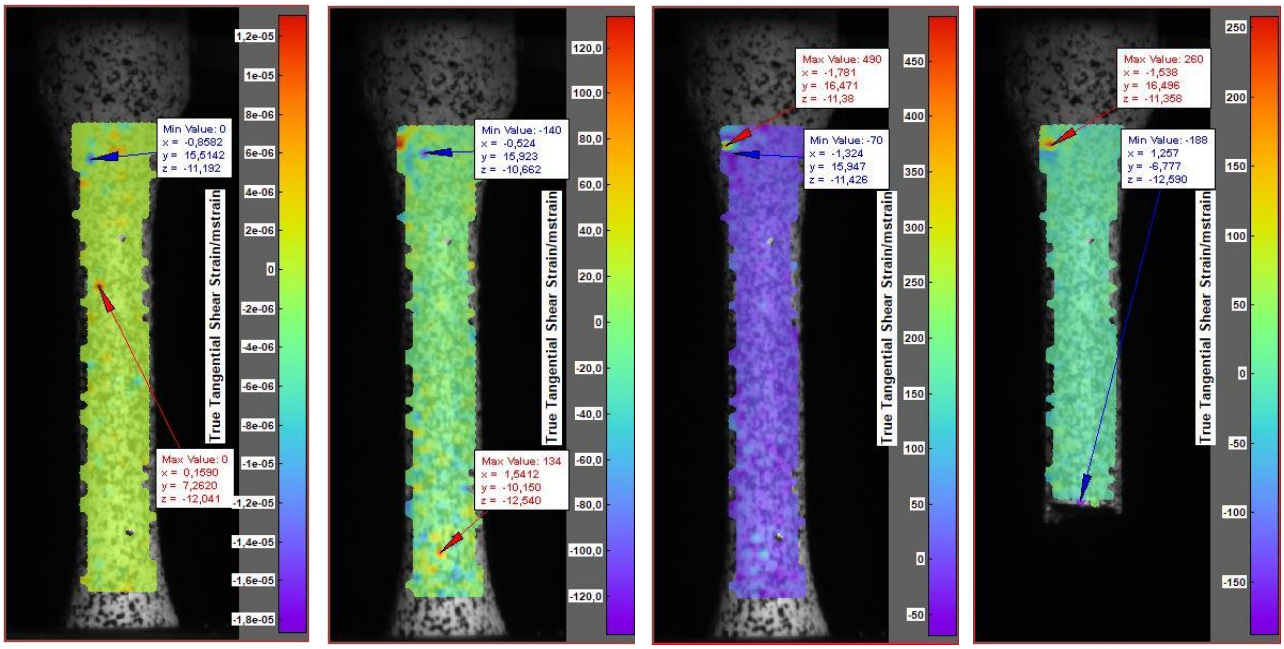

Figure B.11-3: From left to right: B11 reference image, B11 half-life image, B11 final image, B1 failure image

From the final two images in the figure above it can be noticed that the point of failure was once again not in the same region of the specimen as where the DIC indicates a maximum shear strain measurement in the image the moment before failure.

90º Fatigue test specimen

B.12 SPECIMEN A1

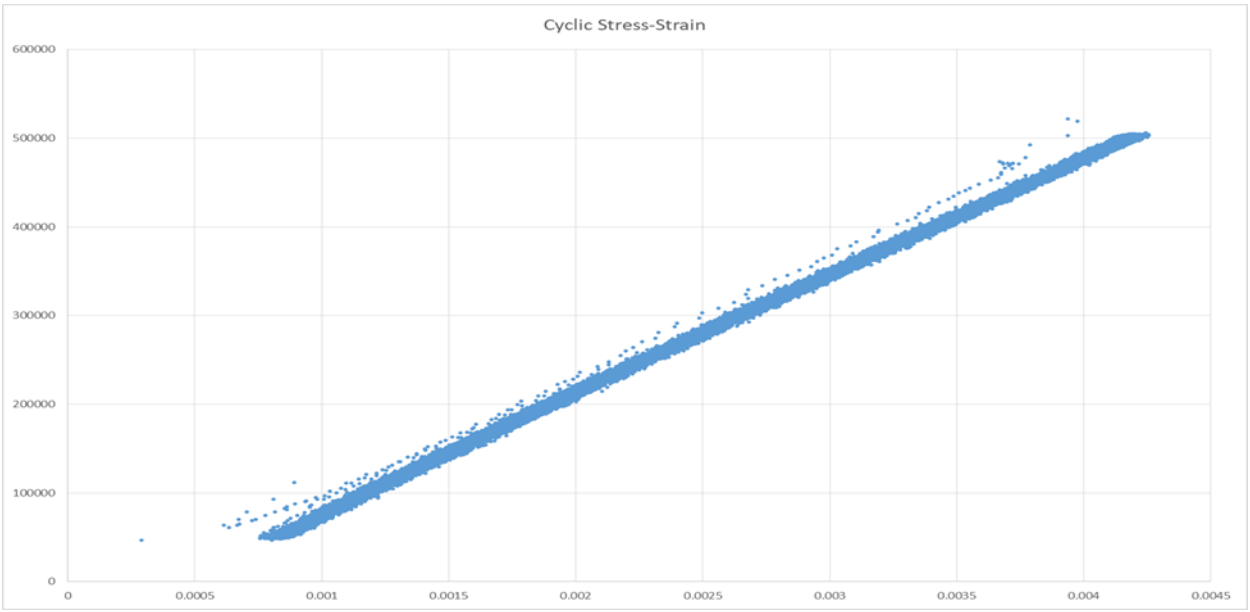

Figure B.12-1: Hysteresis stress-strain curve for specimen A1

As with the other specimens this particular specimen did not experience a great change in strain for the stress controlled fatigue test.

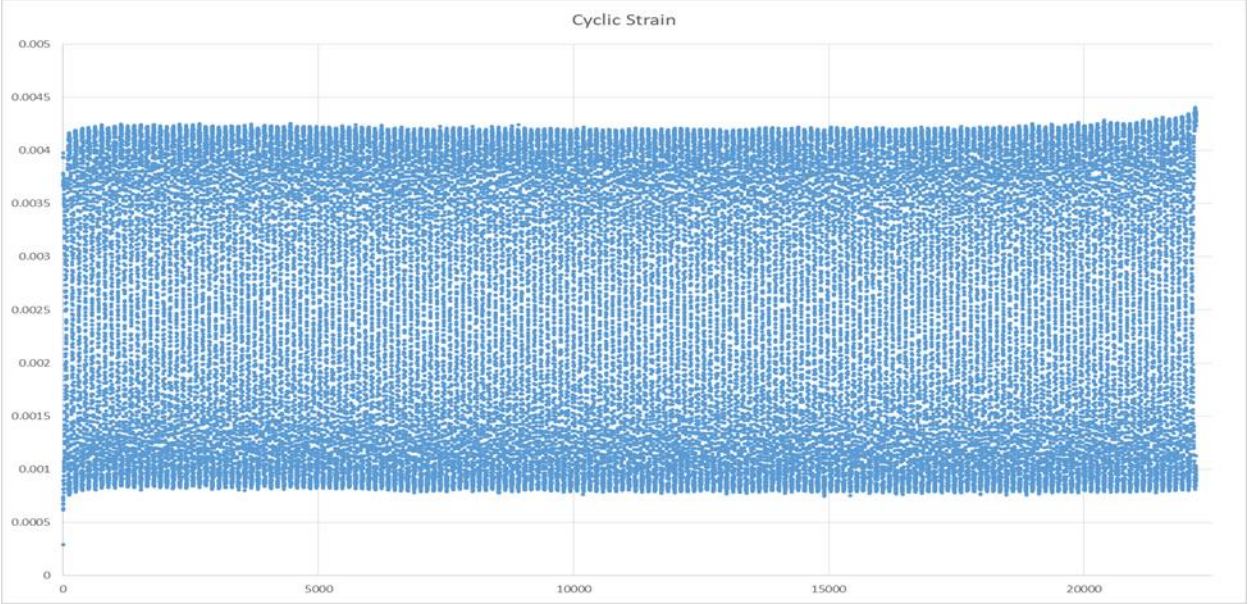

Figure B.12-2: Strain-life graph for specimen A1

Figure B.12-2 reaffirms the statement from above as it is noticeable that the peak values for the strain does not change except at the end of the fatigue life.

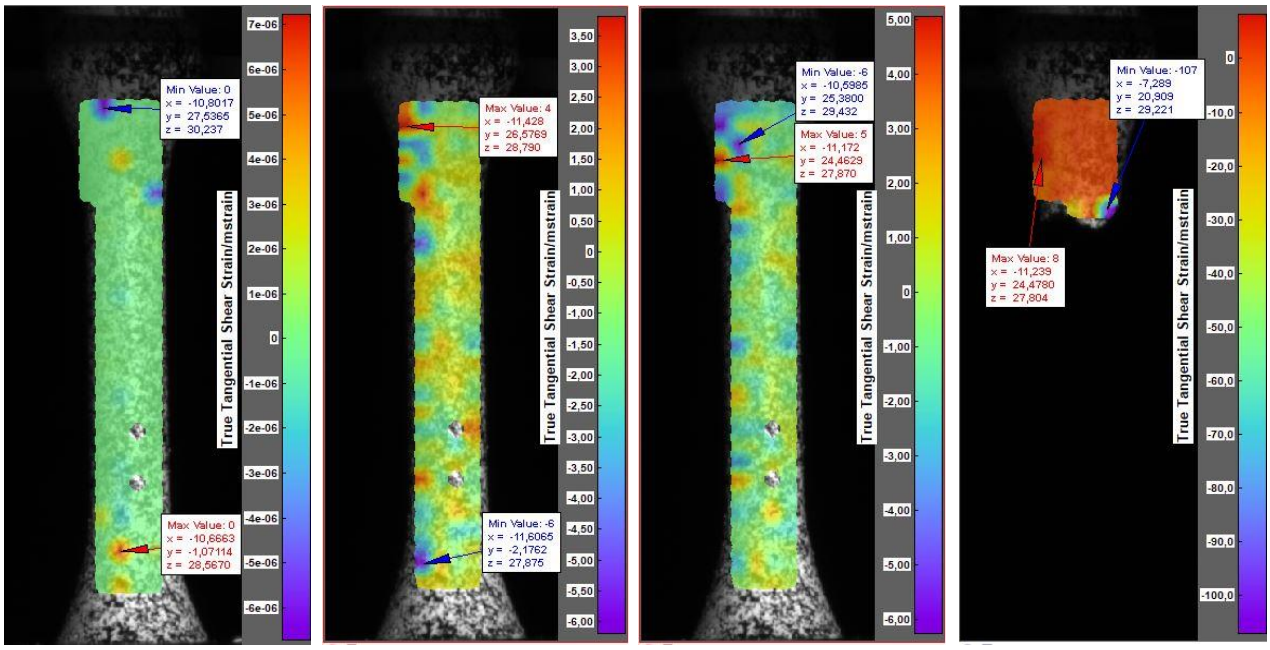

Figure B.12-3: From left to right: A1 reference image, A1 half-life image, A1 final image, A1 failure image

Looking at the last two images from Figure B.12-3 it can be seen that the shear strain concentration is visualised at the top of the gauge length of the test specimen. The specimen also

breaks in this region but it is important to note that the failure point is slightly lower than where it is indicated in the image taken right before failure.

B.13 SPECIMEN A2

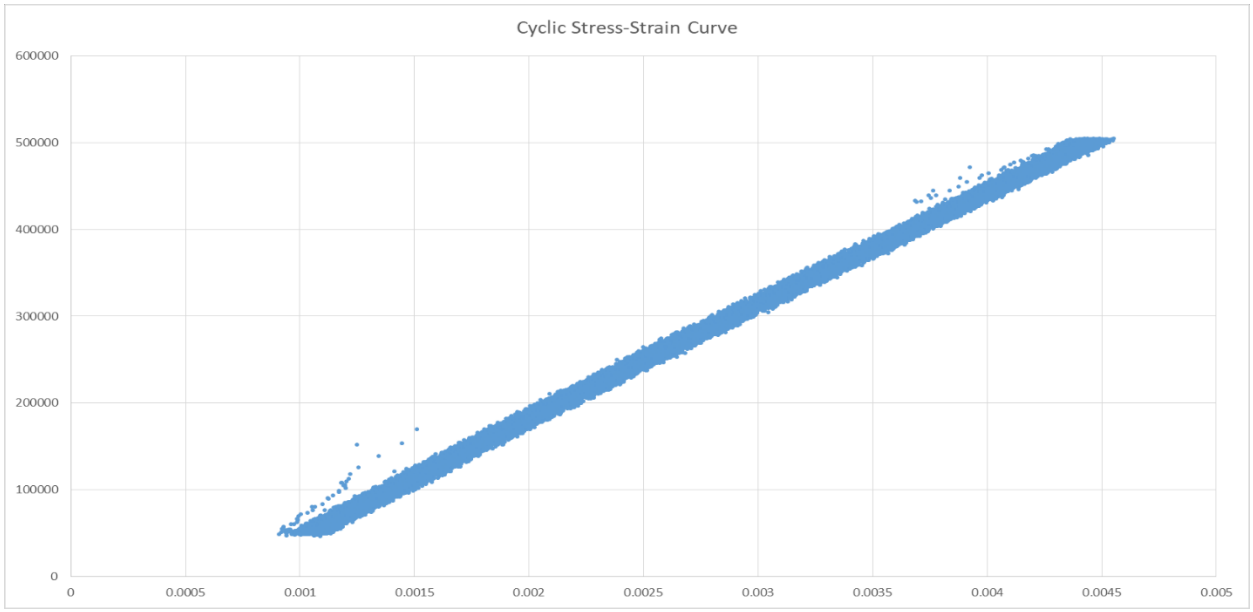

Figure B.13-1: Hysteresis stress-strain curve for specimen A2

For specimen A2 it is noticed that the strain for the specimen's half-life does not indicate that the specimen undergoes a great deal of elongation for the stress that is applied to it.

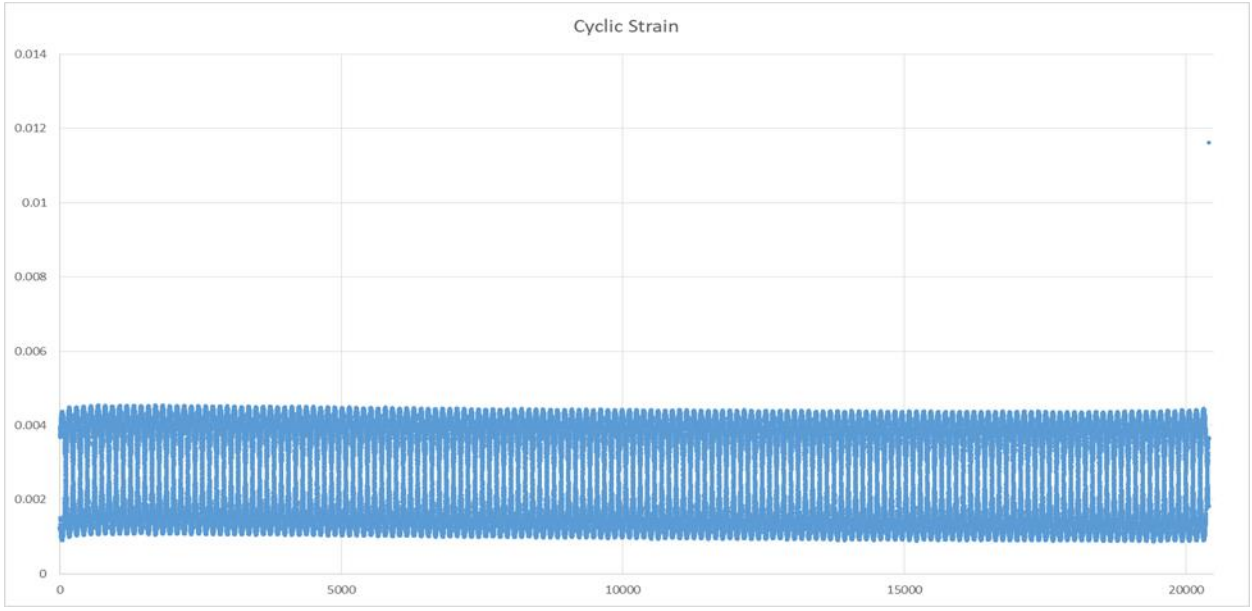

Figure B.13-2: Strain-life graph for specimen A2

Looking at the strain-life graph for specimen A2, it can be seen that the peak values for strain does not vary at the 20 000 cycle mark with regards to the initial values of strain.

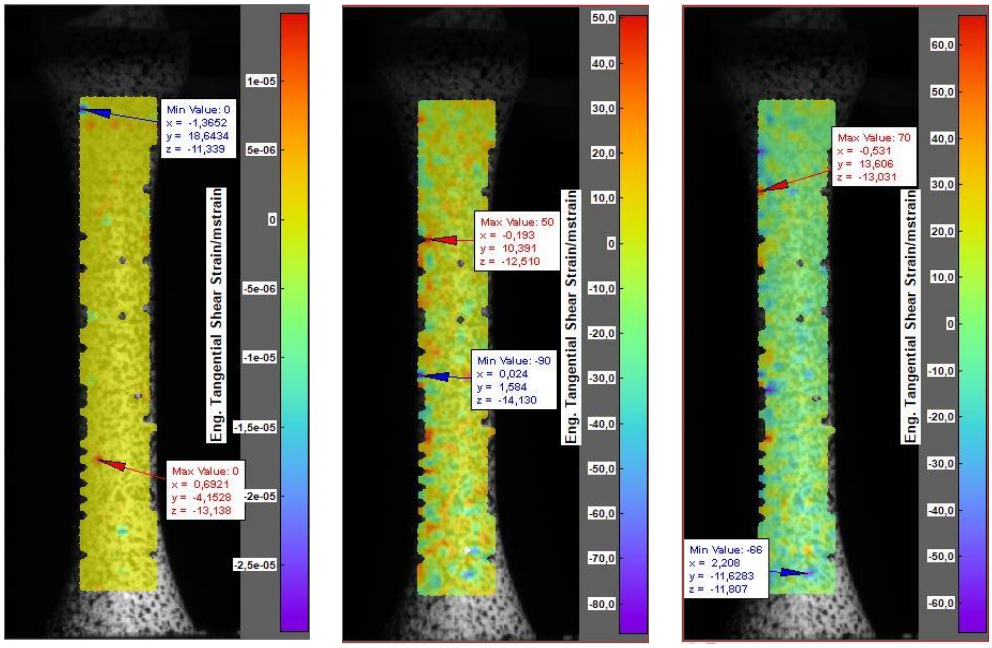

Figure B.13-3: From left to right: A2 reference image, A2 half-life image, A2 final image

For this test specimen, (which was the first test specimen that was tested) the DIC stopped recording images once the fatigue failure point was reached. That means that this specimen does not have a DIC image of the failure. Included is an image of the specimen taken after failure just to show where the specimen failed.

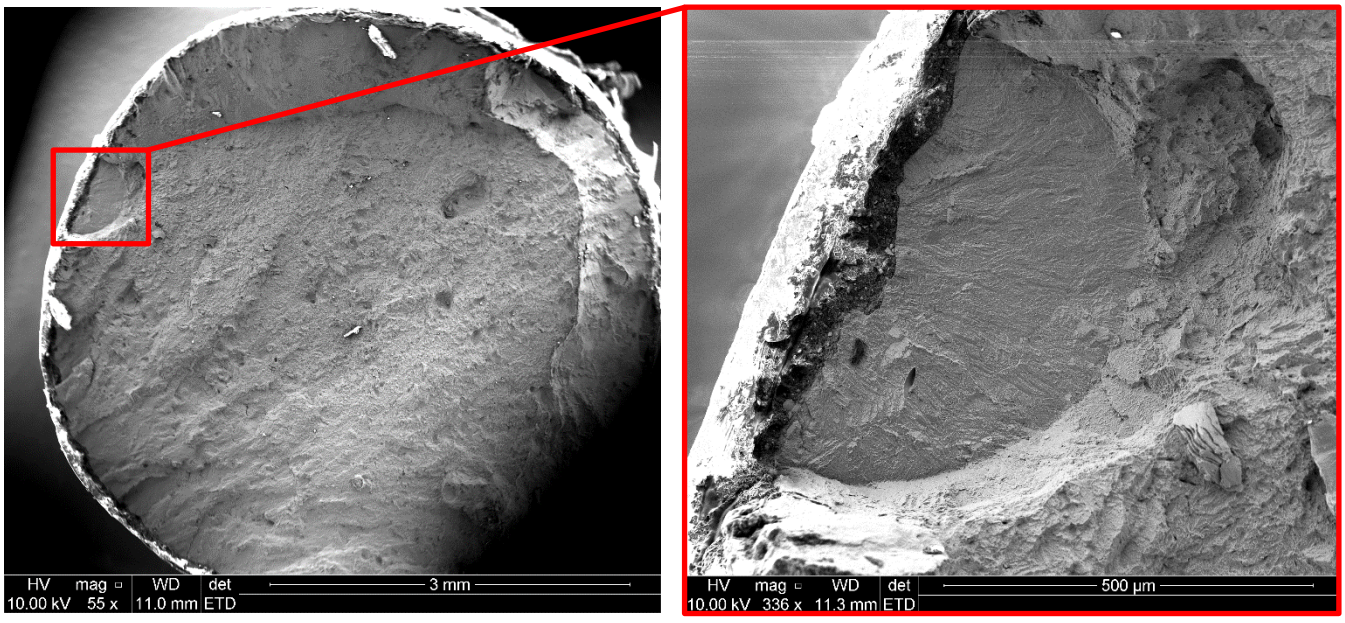

Figure B.13-4: SEM images for specimen A2

For this specimen it is noticeable that there is quite a large surface defect present (almost 500 µm) in length. This surface defect is thought to be the main cause of failure as it would promote crack-propagation due to a stress concentration in this area.

B.14 SPECIMEN A3

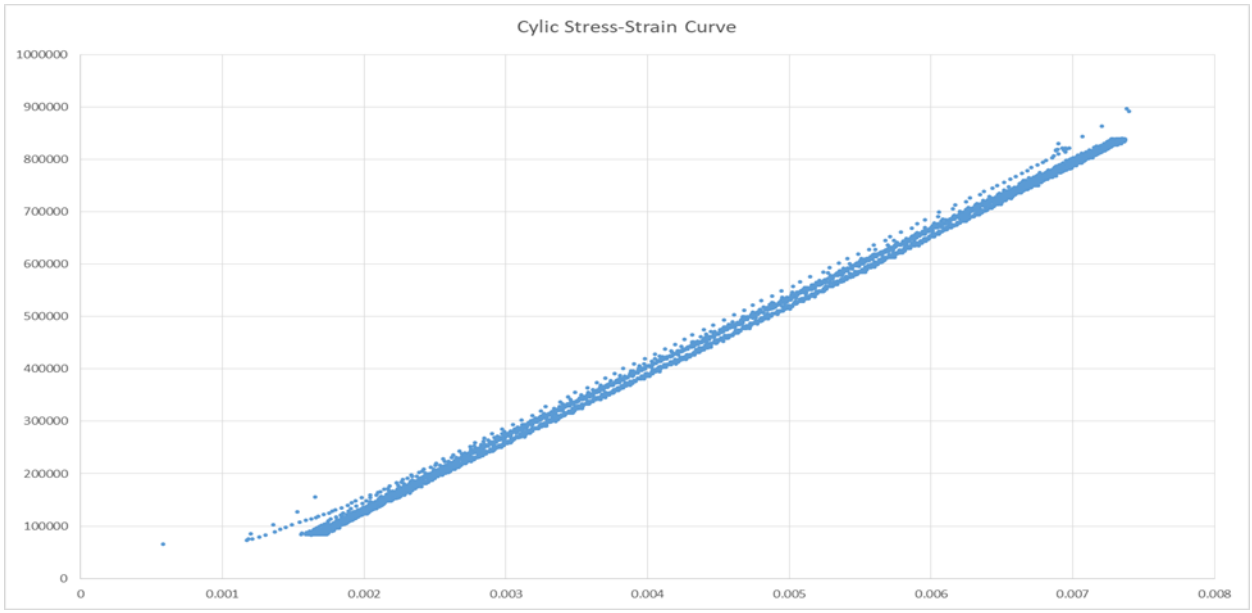

Figure B.14-1: Hysteresis stress-strain curve for specimen A3

As with most of the specimens, for which a hysteresis stress-strain curve is evaluated, it can be noticed that there is no great change in the strain values measured during the fatigue tests.

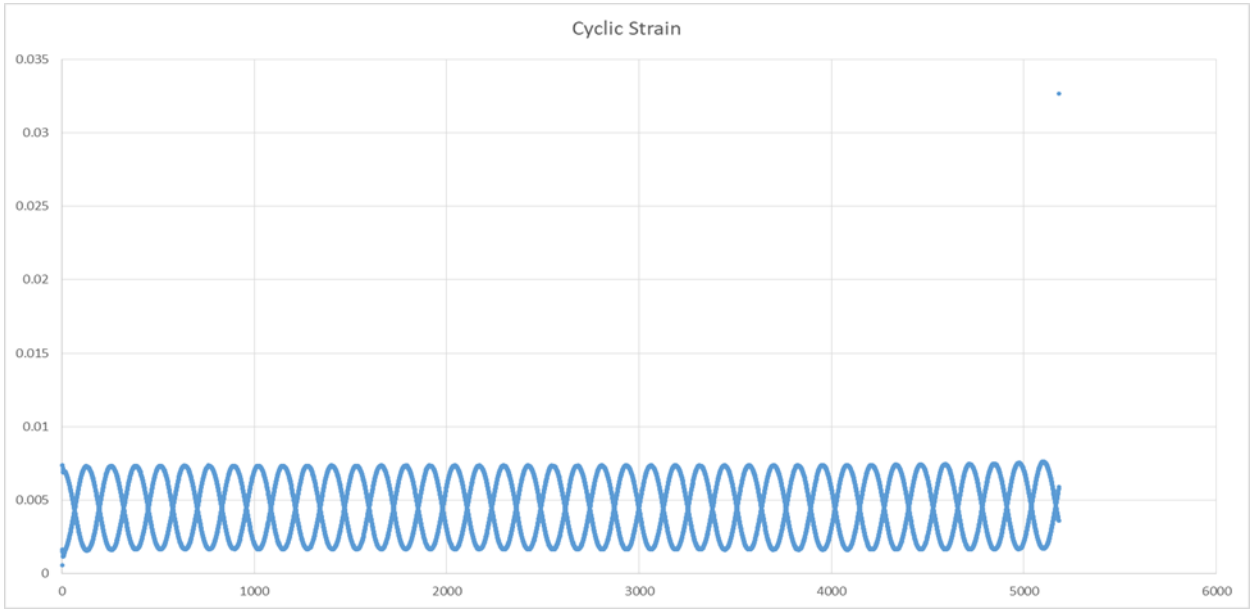

Figure B.14-2: Strain-life graph for specimen A3

Looking at figure B.14-2 it is clear that the peak values of the strain-life graph does not change throughout the entirety of the life-cycle.

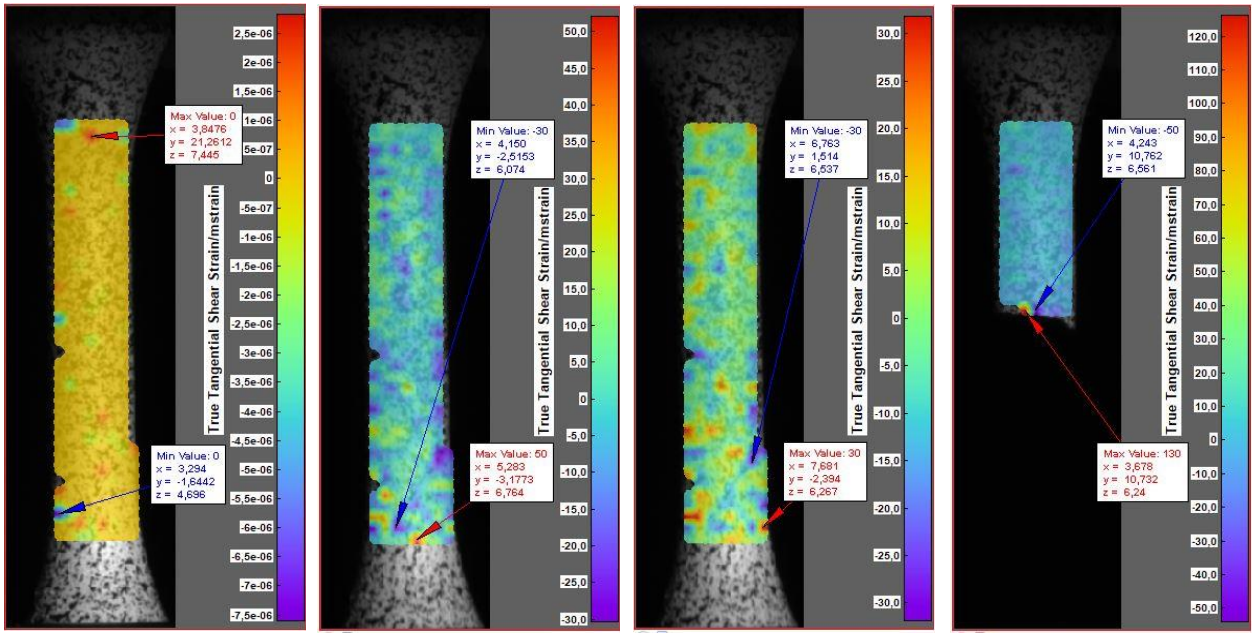

Figure B.14-3: From left to right: A2 reference image, A3 half-life image, A3 final image, A3 failure image

Figure B.14-3 shows that the test specimen broke somewhere near the middle of the gauge length. The shear strain concentration that was visualised indicates a maximum shear strain at the bottom of the gauge length.

B.15 SPECIMEN A4

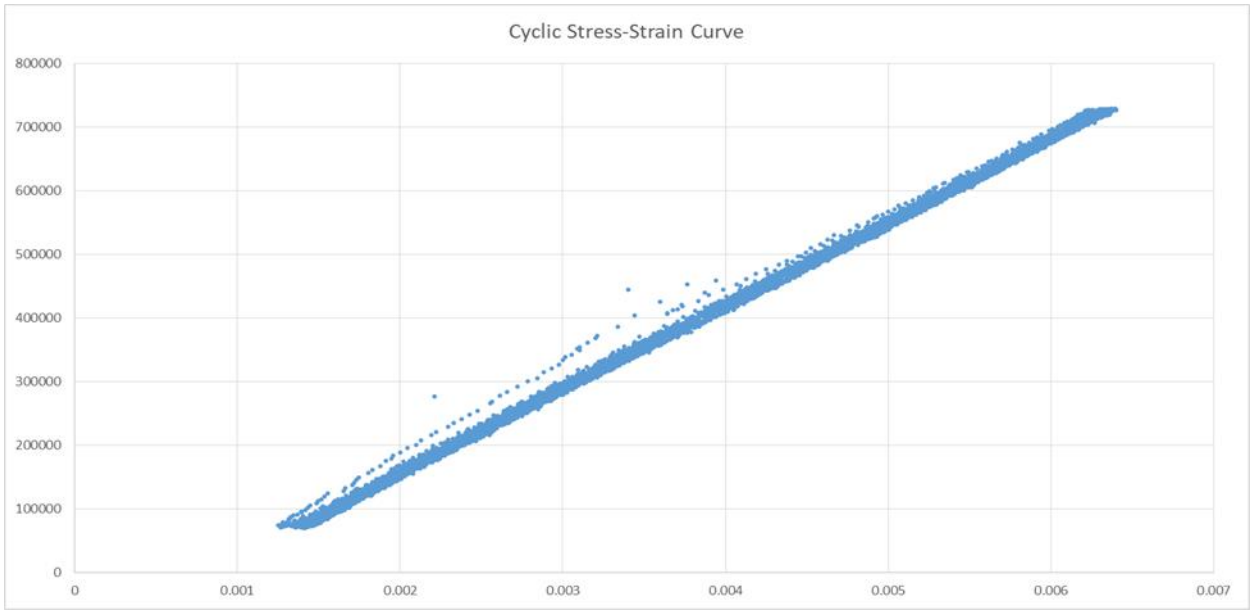

Figure B.15-1: Hysteresis stress-strain curve for specimen A4

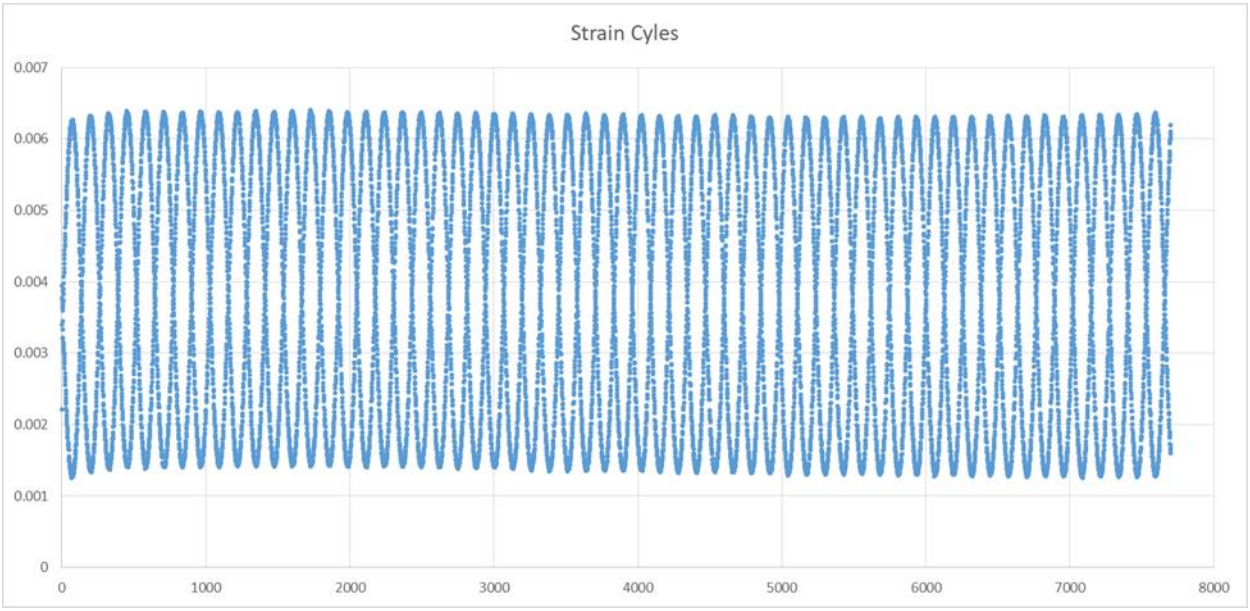

Figure B.15-2: Strain-life graph for specimen A4

Specimen A4 performed in the same manner as most of the other specimens from this study. Figures B.15-1 and B.15-2 shows this through the strain-life graph where there is no change in the peak values of strain for the duration of the fatigue test.

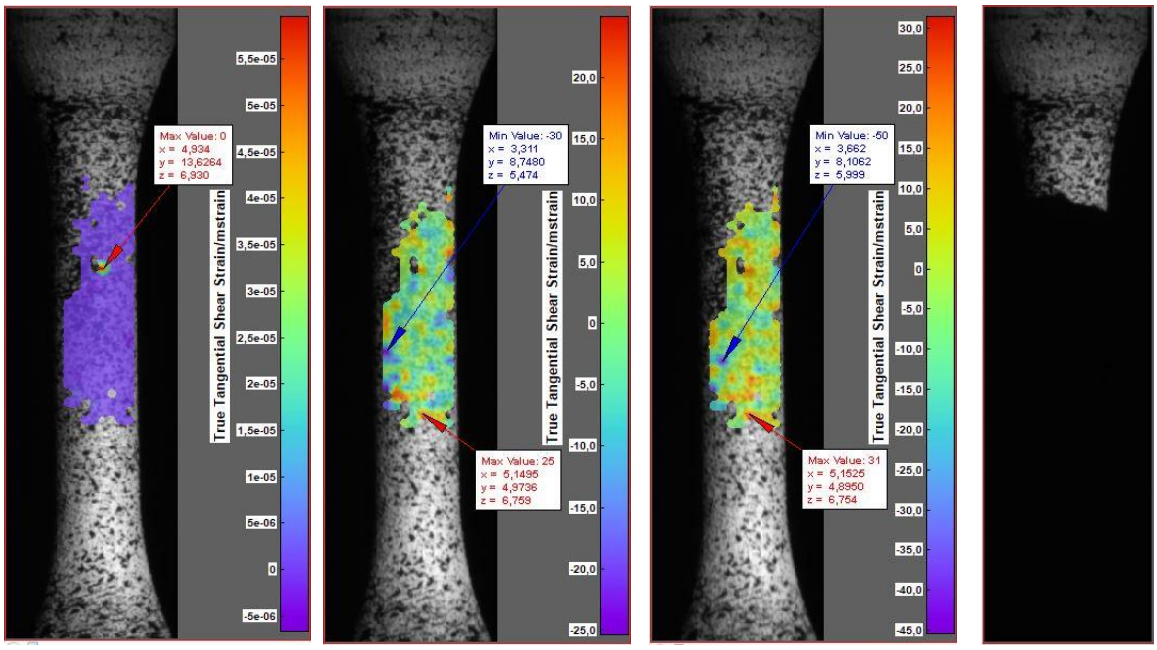

Figure B.15-3: From left to right: A4 reference image, A4 half-life image, A4 final image, A4 failure image

Image 4 in Figure B.15-3 shows the failure point located at the top of the gauge length, whilst image two and three, which are the images taken at the half life and the moment before failure, indicate a maximum shear strain near the middle of the test specimen's gauge length.

B.16 SPECIMEN A5

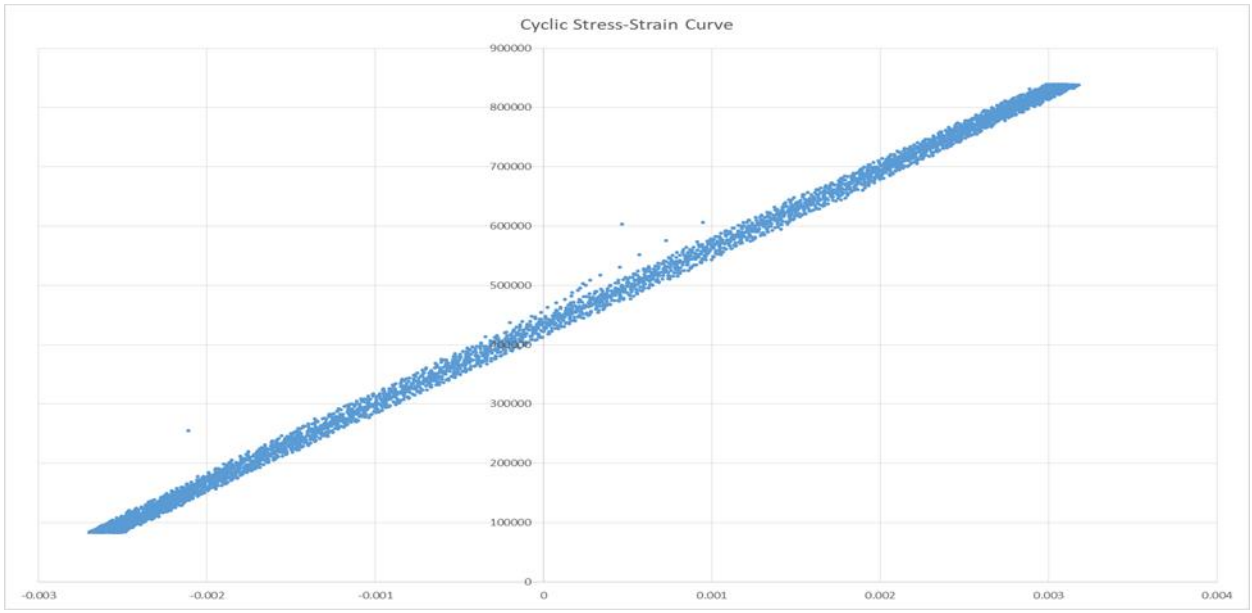

Figure B.16-1: Hysteresis stress-strain curve for specimen A5

Test specimen A5 is another specimen that experienced some compression during the test, even though with a stress ratio (R=0.1) indicating a tensile-tensile test. This occurrence is due to operator error during the setup of the fatigue test.

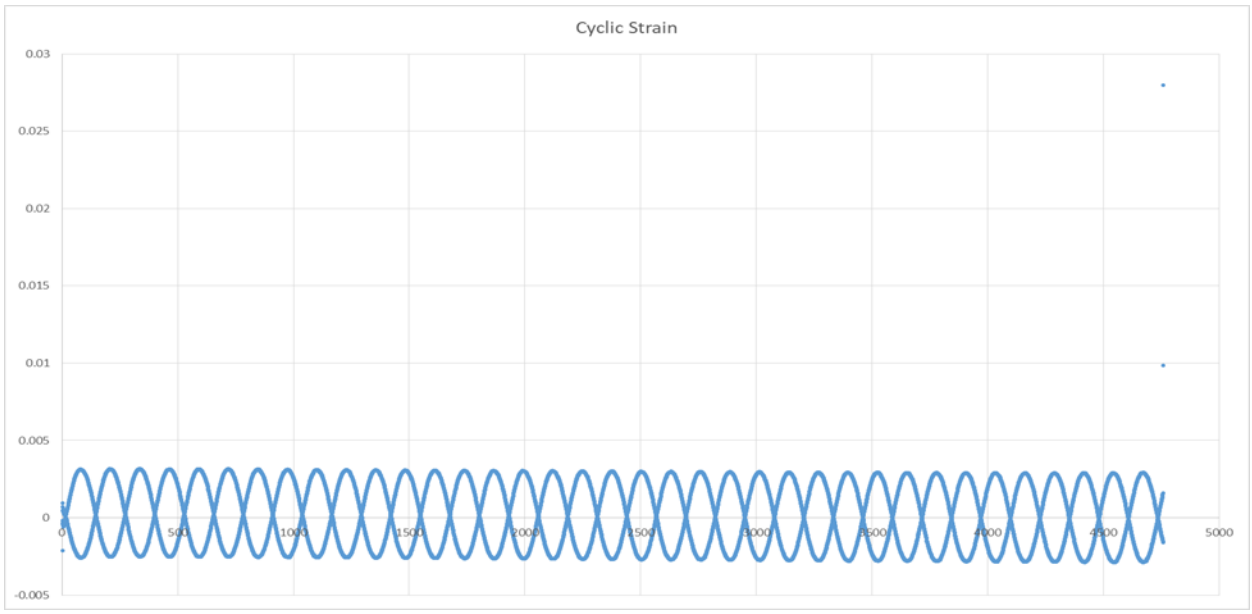

Figure B.16-2: Strain-life graph for specimen A5

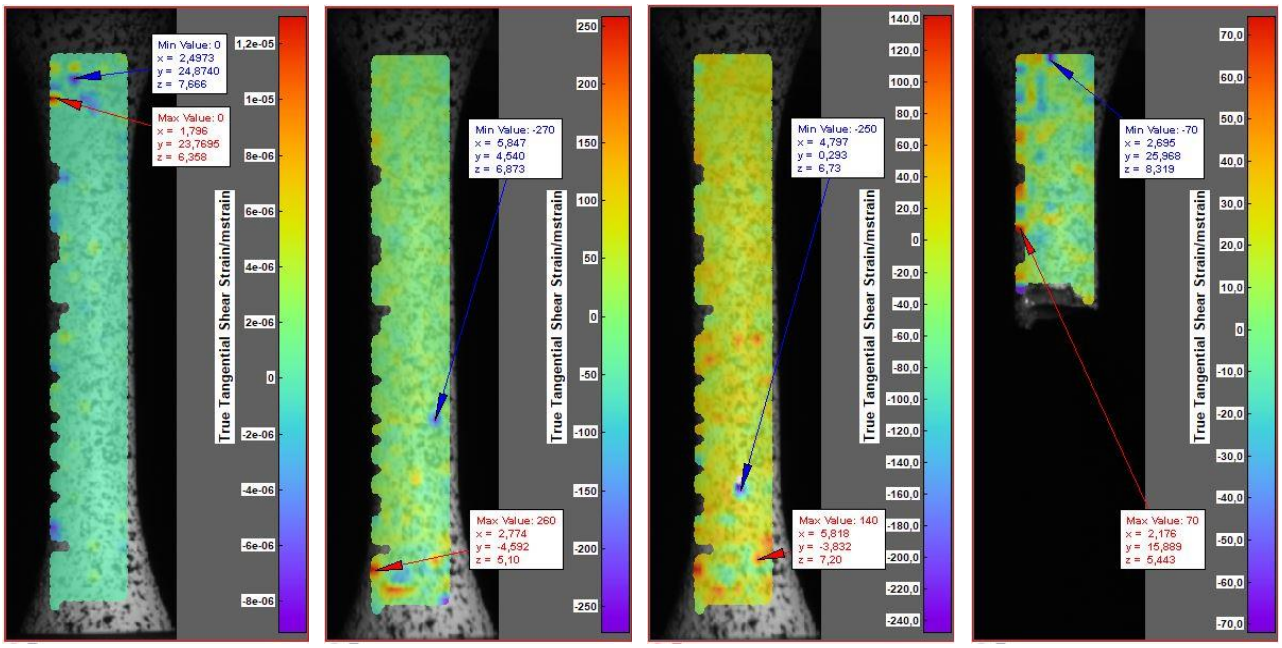

Figure B.16-3: From left to right: A5 reference image, A5 half-life image, A5 final image, A5 failure image

From figure B.16-3 it can be noticed that the test specimen did not break where the strain concentration of the final image that was taken indicates it is expected to break. This anomaly is observed in most specimens included in this study.

B.17 SPECIMEN A6

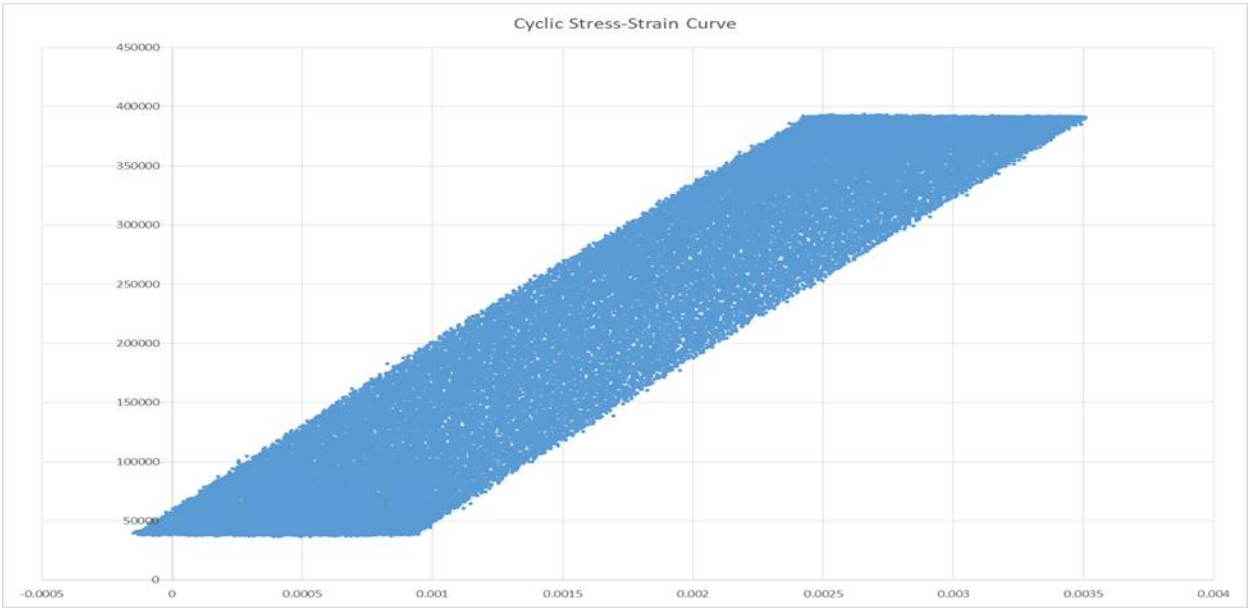

Figure B.17-1: Hysteresis stress-strain curve for specimen A6

From figure B.17-1 it can be noticed that there is a change in the strain from the beginning of the test to the half-life point of the fatigue test measured at approximately 0.001 mm/mm.

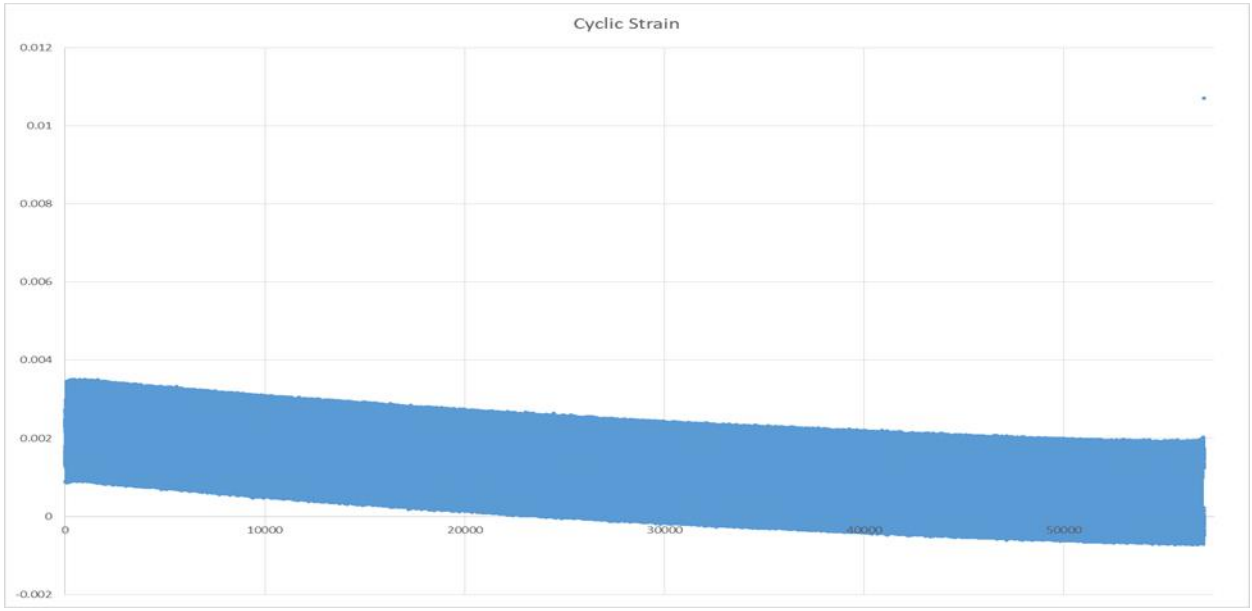

Figure B.17-2: Strain-life graph for specimen A6

This graph indicates that the test specimen enters a compression phase nearing the end of the fatigue test. This is something that is not expected as the fatigue test is a tensile-tensile test with the stress being controlled.

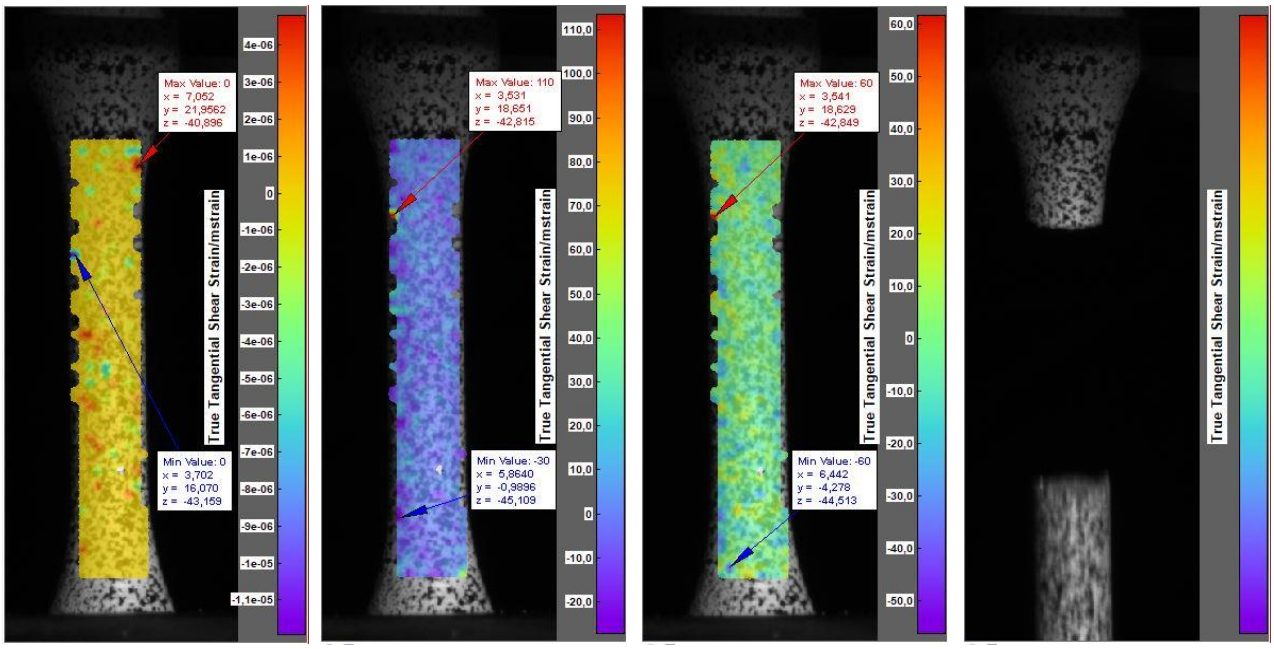

Figure B.17-3: From left to right: A6 reference image, A6 half-life image, A6 final image, A6 failure image

From image three and four in Figure B.17-3 it can be seen that the test specimen actually breaks in the region where the DIC system indicates that there is a maximum shear strain concentration. It can also be noticed in image two which was captured at the half-life of the fatigue test.

B.18 SPECIMEN A7

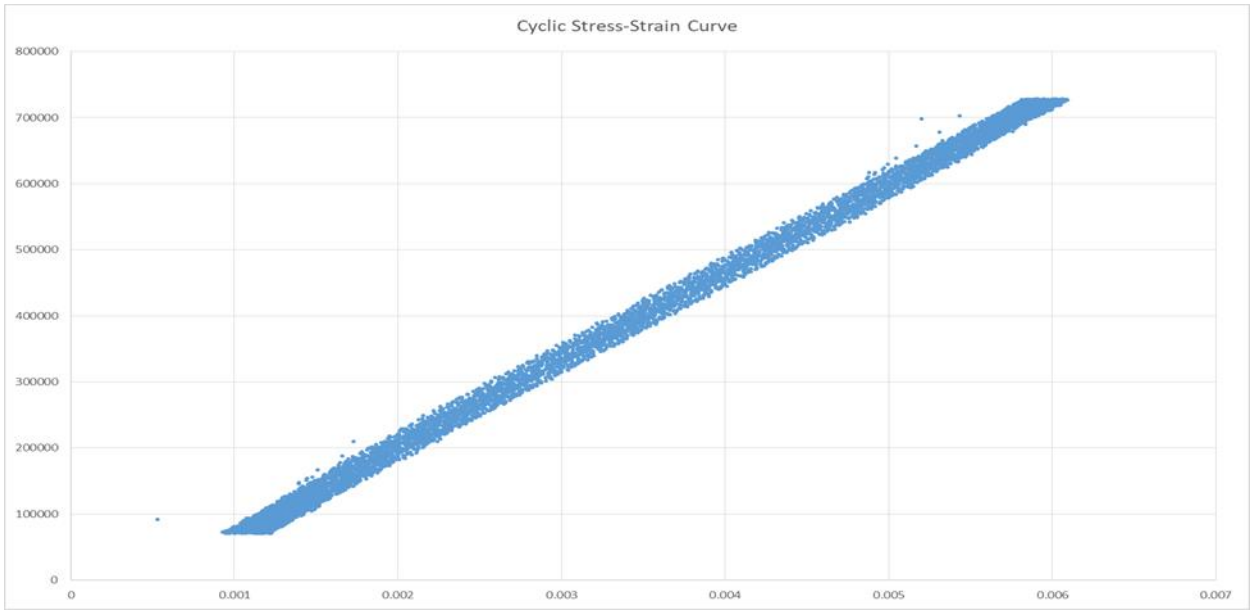

Figure B.18-1: Hysteresis stress-strain curve for specimen A7

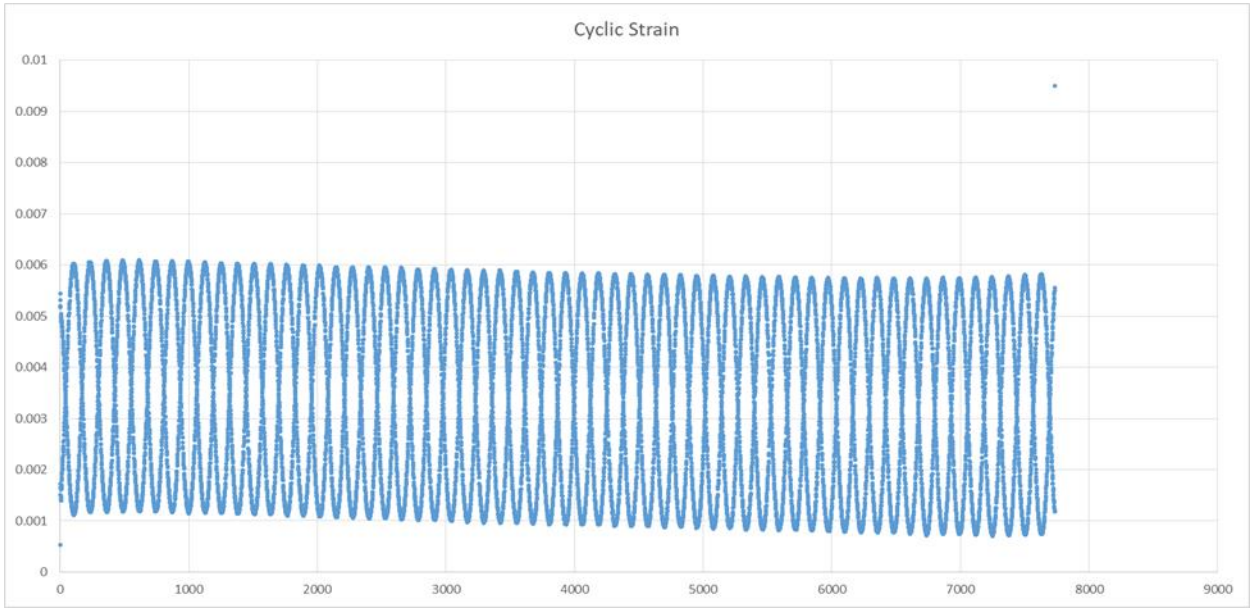

Figure B.18-2: Strain-life graph for specimen A7

Figures B.18-1 and B.18-2 again proves to illustrate that the strain does not vary significantly at the point of failure when compared to the first few cycles.

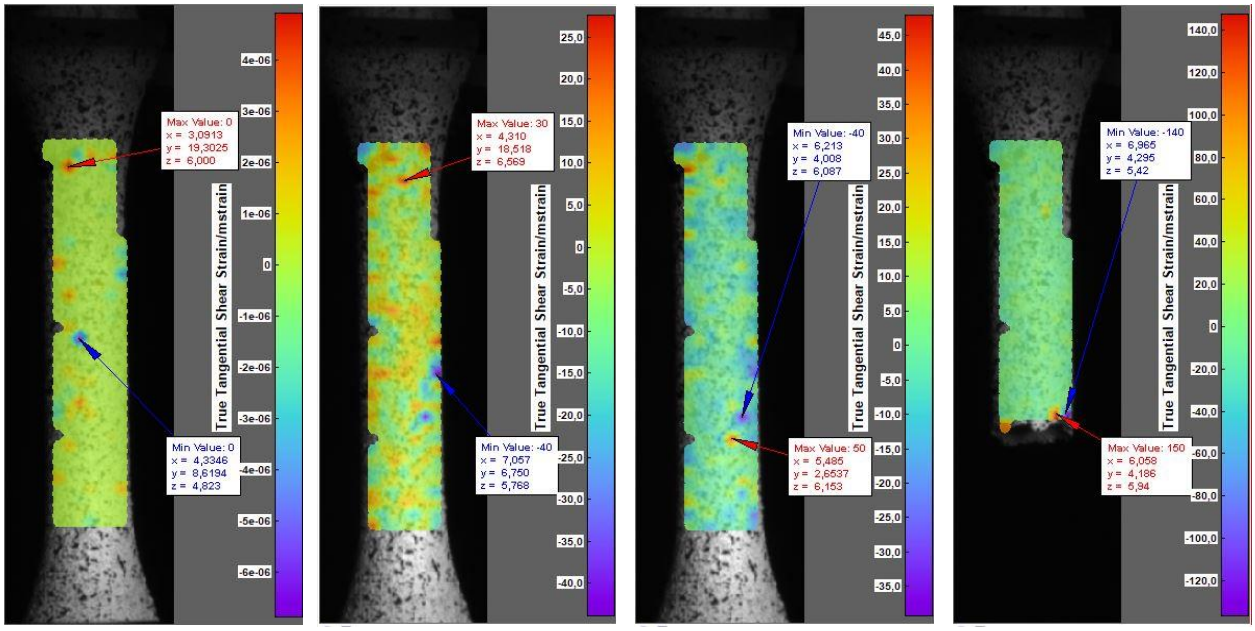

Figure B.18-3: From left to right: A7 reference image, A7 half-life image, A7 final image, A7 failure image

As with test specimen A6 there is quite a good correlation between the failure point as shown in image four of Figure B.18-3 and the maximum shear strain concentration visualised in image three. The one difference between this test specimen and specimen A6 is that in A6 the shear strain concentration at the half-life point was also in the region where the test specimen failed. This is not the case for specimen A7.

B.19 SPECIMEN A8

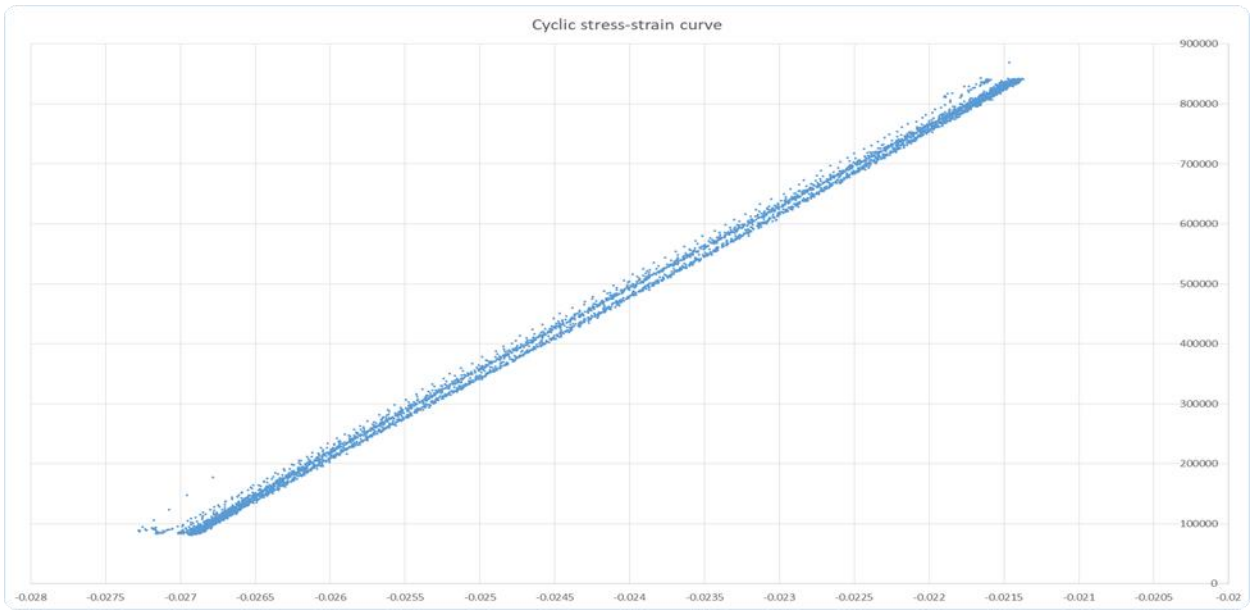

Figure B.19-1: Hysteresis stress-strain curve for specimen A8

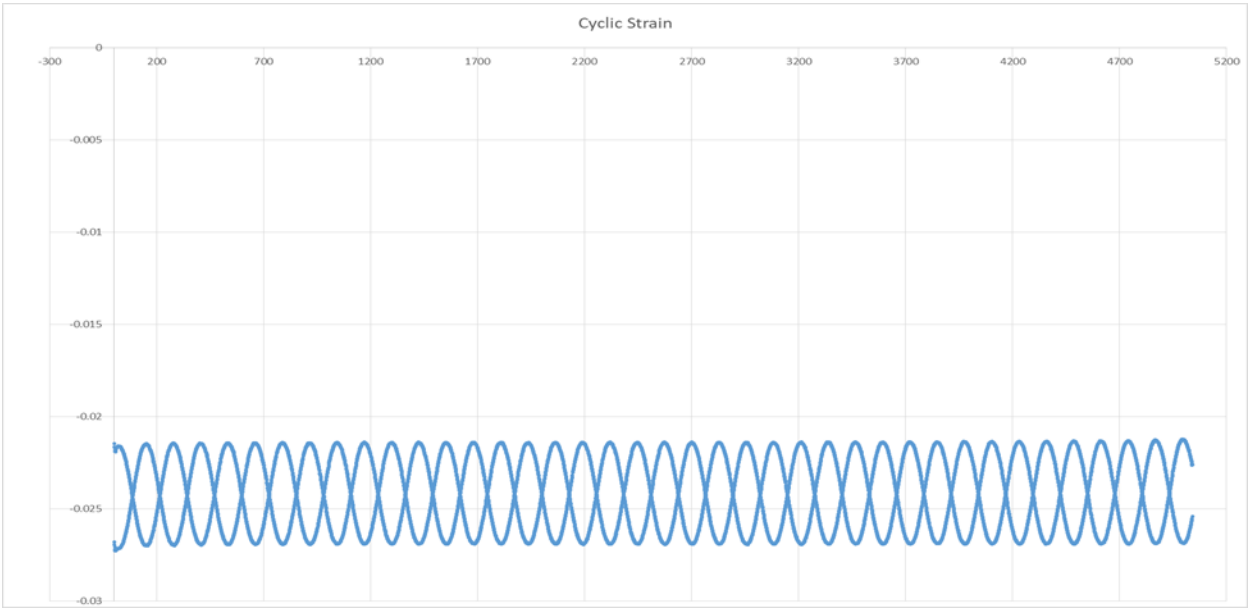

Figure B.19-2: Strain-life graph for specimen A8

For specimen A8 the test was completed but when the data was evaluated it was noticed that there was an initial compression applied on the test specimen. The cause of this was due to the bottom clamp of the test machine that was not returned to zero before testing commenced, thus causing the data to be irrelevant.

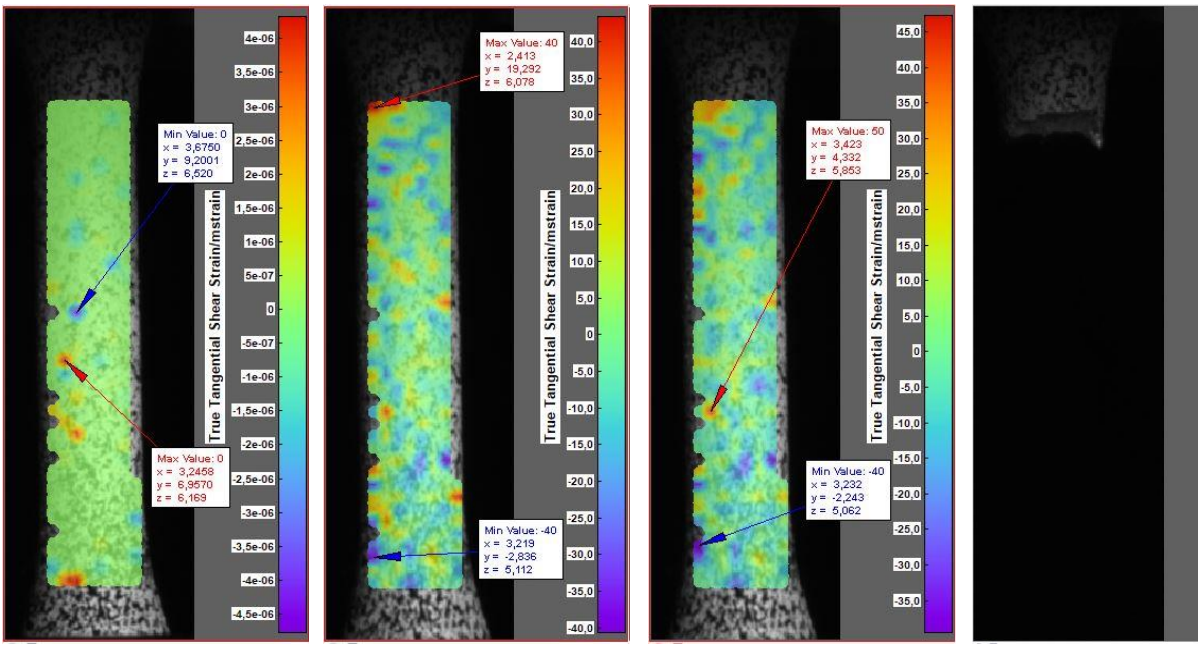

Figure B.19-3: From left to right: A8 reference image, A8 half-life image, A8 final image, A8 failure image

Even though the data from this test specimen is irrelevant, it is still important to note that the test specimen did not fail where the final image taken indicates it should fail.

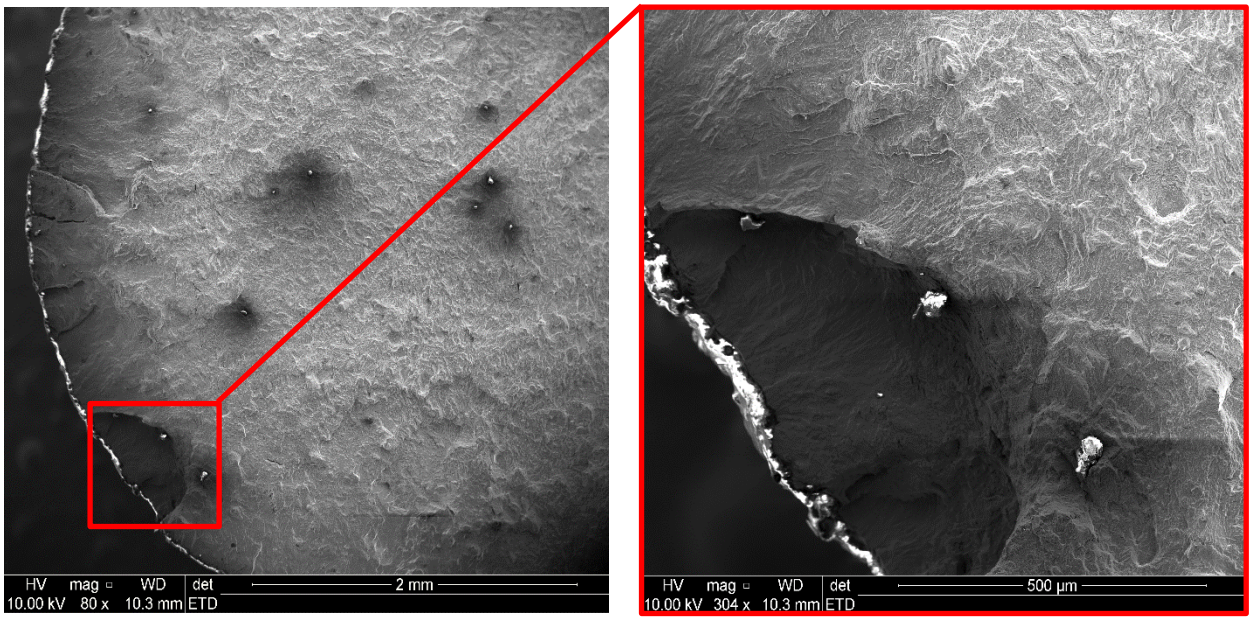

Figure B.19-4: SEM images for test specimen A8

An important conclusion is made from the SEM images taken of this test specimen. The significant size of the surface defect is expected to be the cause of failure for this test specimen.

B.20 SPECIMEN A9

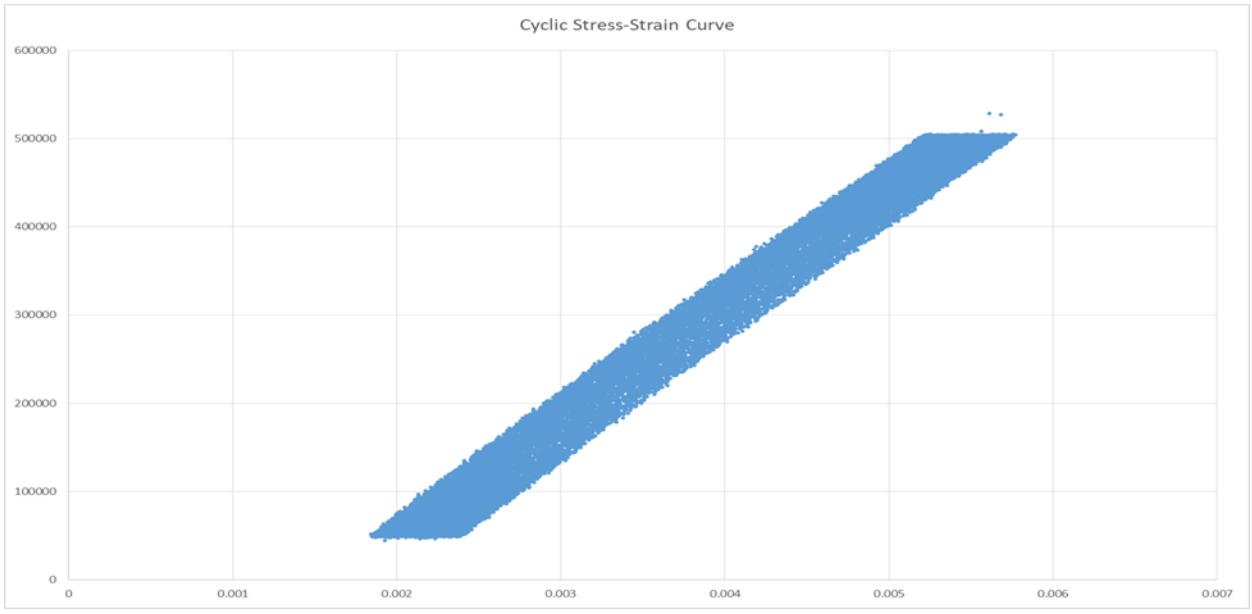

Figure B.20-1: Hysteresis stress-strain curve for specimen A9

Test specimen A9 undergoes a small change in strain, approximately 0.0005 mm/mm, over the course of just under 12 000 cycles.

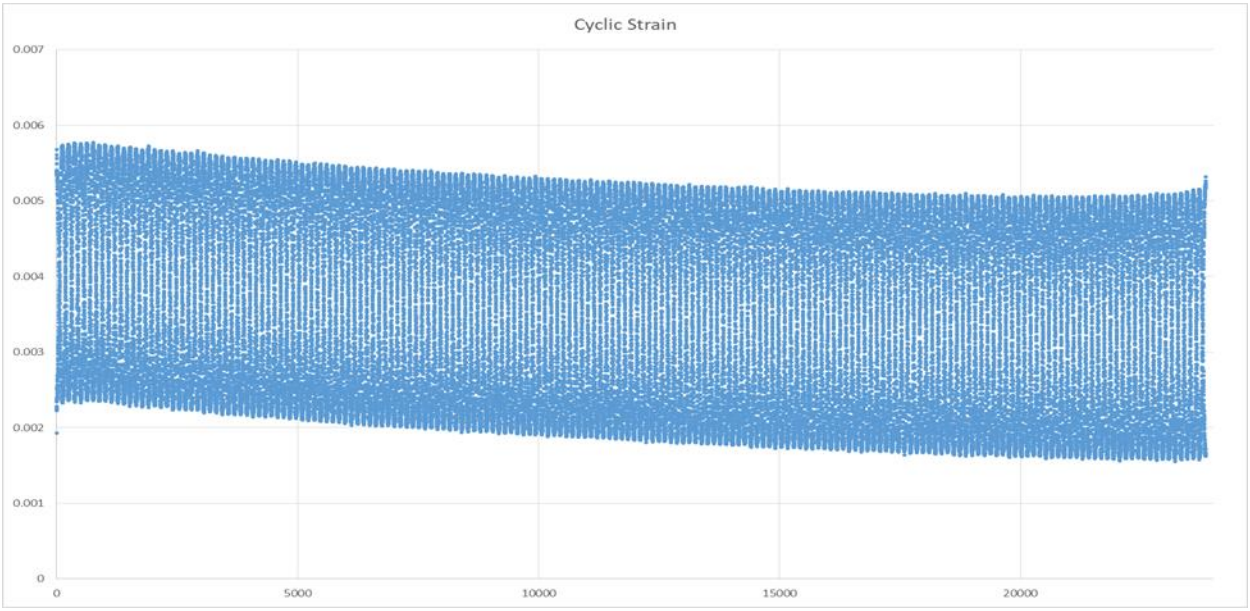

Figure B.20-2: Strain-life graph for specimen A9

The strain-life graph of test specimen A9 shows that the peak values for the strain, both maximum and minimum, decreases over the course of the fatigue life. There is an increase in peak values of strain near the end of the fatigue test and right before failure.

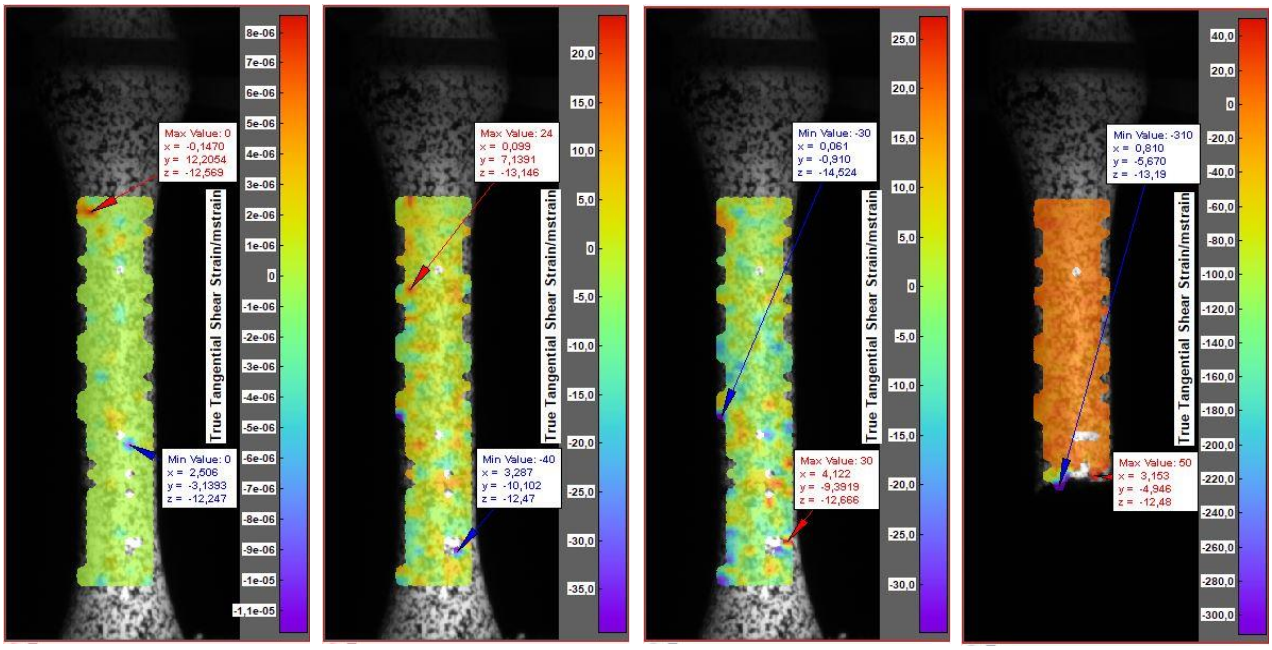

Figure B.20-3: From left to right: A9 reference image, A9 half-life image, A9 final image, A9 failure image

Test specimen A9 broke near the bottom of the test specimen's gauge length. The final image taken before failure indicates a shear strain concentration in the bottom part of the gauge length, but the point of failure is located just above the indicated shear strain concentration.

B.21 SPECIMEN A10

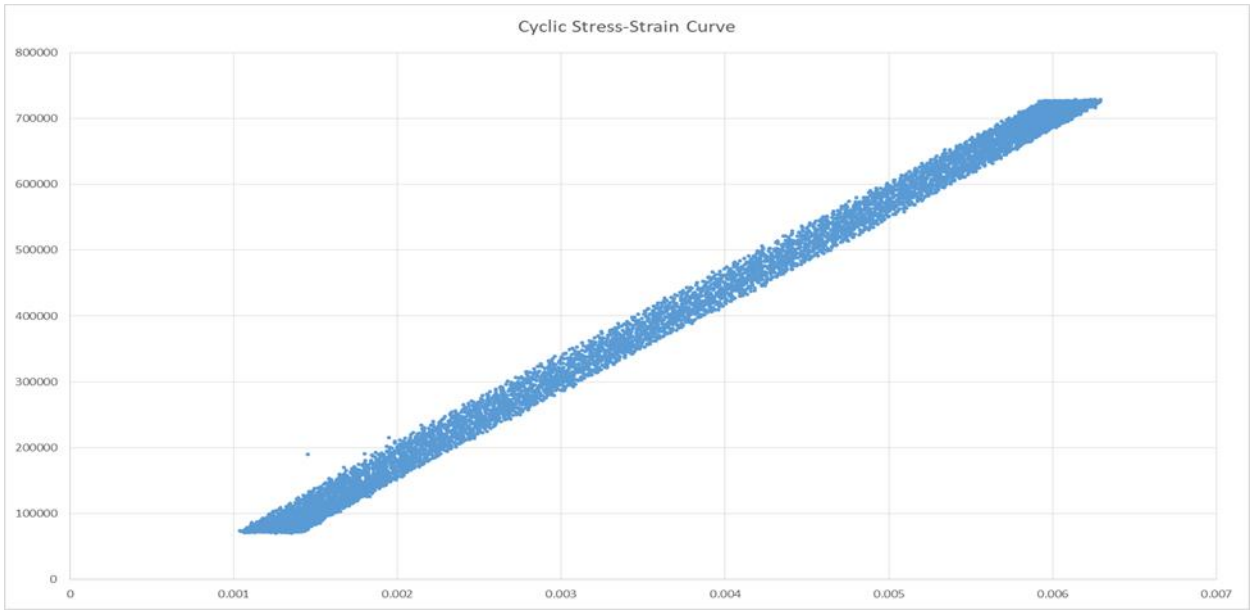

Figure B.21-1: Hysteresis stress-strain curve for specimen A10

For test specimen A10 it can be noticed, by looking at the hysteresis stress-strain curve in Figure B.21-1, that there is a change in strain near enough to 0.0005 mm/mm across the half-life of the fatigue test specimen which is equal to approximately 4 000 cycles.

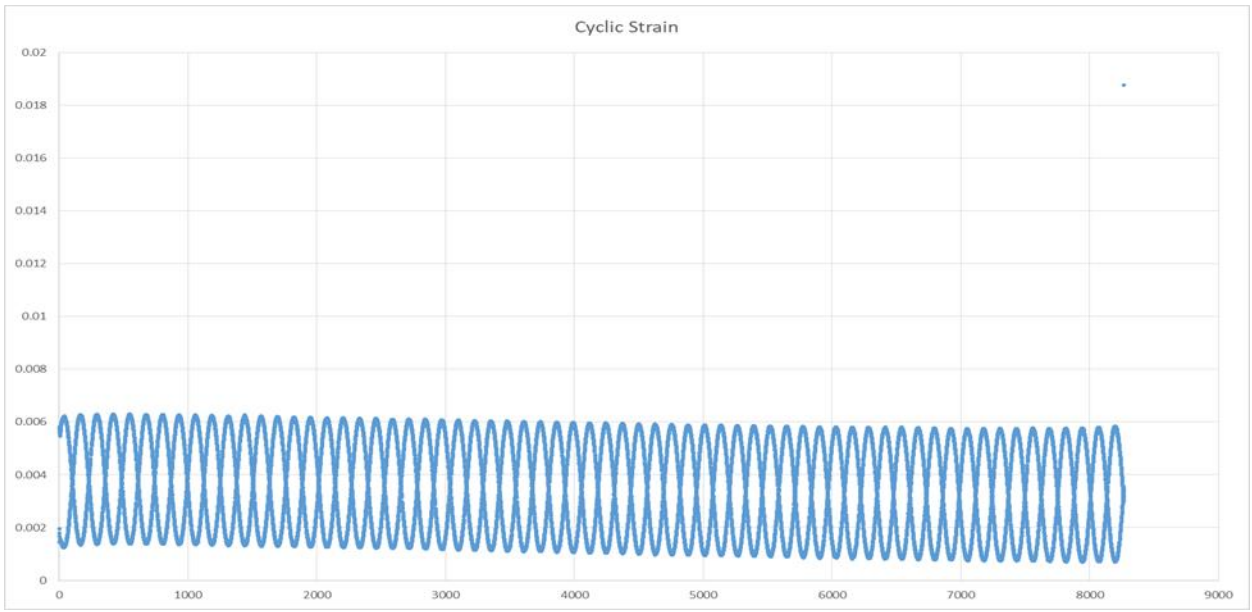

Figure B.21-2: Strain-life graph for specimen A10

The strain-life graph indicates that there is very little change in the peak strain values, both maximum and minimum, measured across the fatigue life of the specimen. It can be noticed that the strain's peak values diverge near the end of the fatigue life.

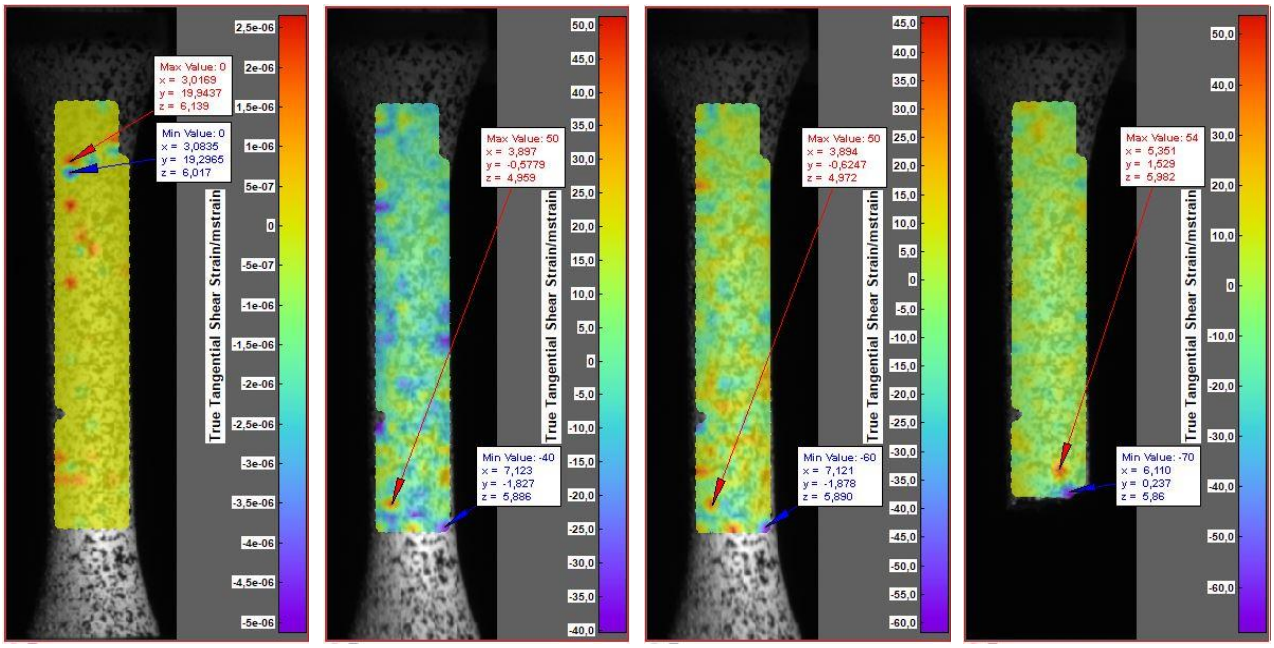

Figure B.21-3: From left to right: A10 reference image, A10 half-life image, A10 final image, A10 failure image

The sample failed at the bottom of the test specimen's gauge length. The shear strain concentration visualised in images two and three, from Figure B.21-3, thus accurately indicates where the specimen is expected to fail. Looking at figure B.21-2 with the divergence of the strain's peak values near the end of the fatigue life, it makes sense that a strain concentration is present and can be detected in the DIC images.

B.22 SPECIMEN A11

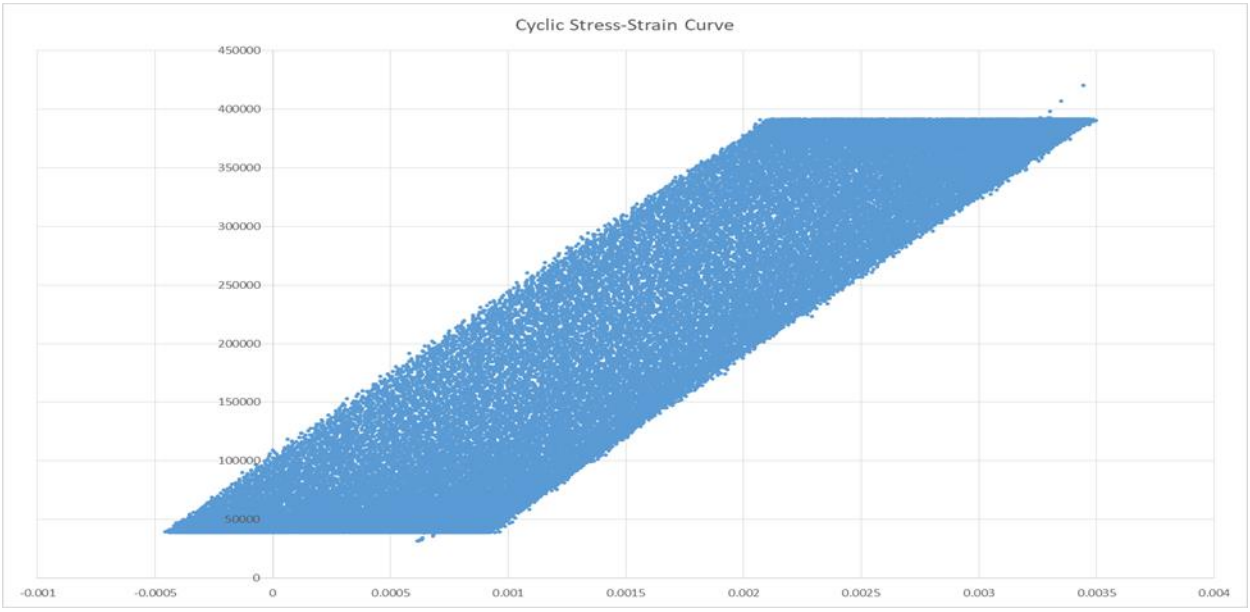

Figure B.22-1: Hysteresis stress-strain curve for specimen A11

Looking at Figure B.22-1 it is clear to the reader that over the course of the 25 000 + cycles, which represents the half-life of the test specimen, the change in strain is measured which equals approximately 0.0015 mm/mm.

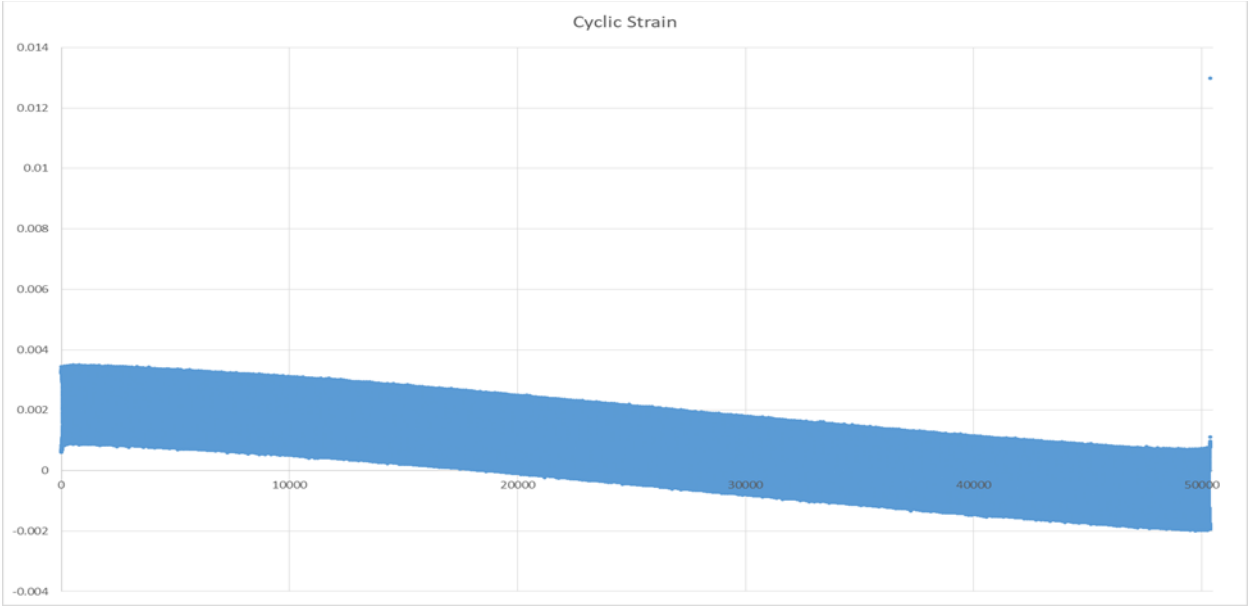

Figure B.22-2: Strain-life graph for specimen A11

The strain-life graph illustrated in Figure B.22-2 does not indicate a change in the peak values measured during the fatigue test, but it does indicate that there is a change from tensile strain to compressive strain over the course of the test. At the end of the fatigue test a divergence in the strain peak values can be identified.

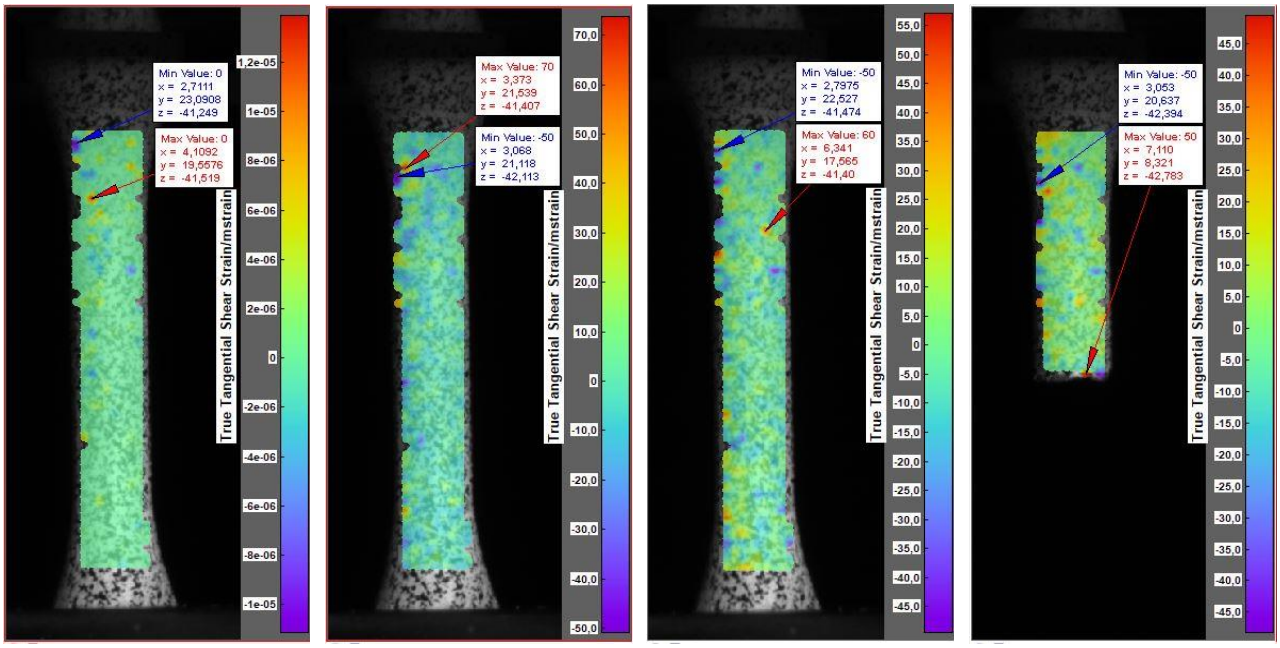

Figure B.22-3: From left to right: A11 reference image, A11 half-life image, A11 final image, A11 failure image

For this specimen there is no real correlation with regards to the visualised maximum shear strain (image three from Figure B.22-3) and the point where the specimen failed (image four from Figure B.22-3).

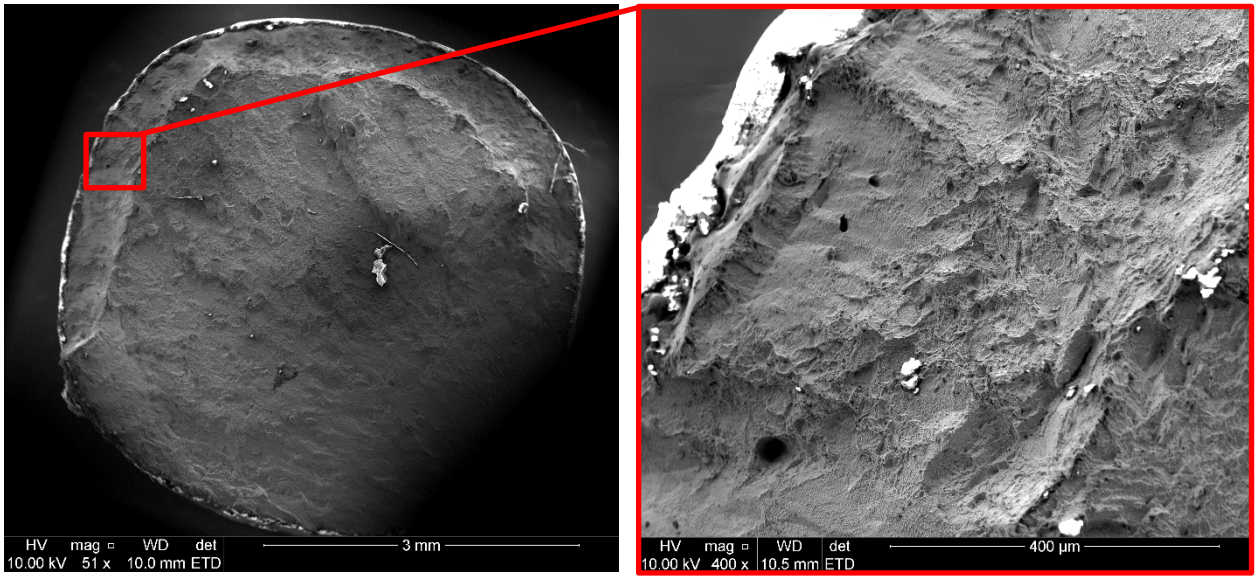

Figure B.22-4: SEM images for specimen A11

No significant defects can be detected on the fracture surface of the test specimen except for a few small holes, which look more like channels/tubes, near the surface of the specimen.